



IFSC UNIVERSIDADE
DE SÃO PAULO
Instituto de Física de São Carlos

Proceedings of the seminar to the course

Eletromagnetismo A

SFI5708 / 2023-2

Ph.W. Courteille (editor)
Universidade de São Paulo
Instituto de Física de São Carlos
30/11/2023

Contents

1	The Goos-Hänchen shift <i>by Anna Cristina Cavallari Inacio</i>	1
1.1	Introduction	1
1.2	Goos-Hänchen shift for a planar surface	1
1.2.1	Case A: electric vector perpendicular to the plane of incidence	2
1.2.2	Case B: electric vector parallel to the plane of incidence	2
1.3	Measuring the Goos-Hänchen shift	3
1.4	Conclusion	4
2	Emission of radiation by a charged particle in gravity <i>by Bruno Trebbi</i>	6
2.1	Introduction	6
2.1.1	Contextualization and History of the problem	6
2.1.2	The equivalence principle	6
2.2	The apparent physical paradox	7
2.3	Can Special Relativity Handle Acceleration?	8
2.3.1	Hyperbolic Motion	8
2.3.2	Rindler Horizon	9
2.4	The radiation seen by the Minkowski reference frame	10
2.5	Radiation seen by the comoving reference frame	11
2.6	What about the energy?	11
2.7	Conclusions	11
3	Magnetic monopoles <i>by Diego França de Oliveira</i>	12
3.1	Introduction	12
3.2	Predicting monopoles	12
3.2.1	Dirac's quantization condition	12
3.2.2	Gauge invariance	14
3.2.3	't Hooft-Polyakov monopole	14
3.3	Looking for monopoles	15
3.3.1	Monopoles detection experiments	15
3.3.2	Astrophysical bounds	16
3.4	Making monopoles	17
3.4.1	Particle accelerators	17
3.5	Conclusion	17
4	The Thomas precession <i>by Jaime J.B. Marquez</i>	18
4.1	Introduction	18
5	Superconductivity and the Meissner effect <i>by Julia Marcolan Teixeira</i>	19
5.1	Introduction	19
5.2	Superconductor features and Meissner effect	20
5.3	London equations	21
5.4	BCS theory	22
5.5	Applications of superconductivity	23

5.5.1	Magnetic Resonance Imaging (MRI)	23
5.5.2	Magnetic Levitation Transport (Maglev)	24
5.6	Conclusion	24
6	Radiation reaction <i>by Lucas Gois Tavares</i>	25
6.1	Introduction	25
6.2	Dynamics of electrical charges	26
6.2.1	The Liénard–Wiechert potentials	26
6.3	Radiation of an accelerated charge	26
6.3.1	Radiation emitted at low velocities	27
6.4	Radiation reaction	28
6.4.1	Radiation reaction based on conservation of energy	28
6.5	Conclusion	29
7	Mie scattering and the first and second rainbow <i>by Luis Augusto Pereira</i>	31
7.1	Introduction	31
7.2	The rainbow	32
7.2.1	The first rainbow	32
7.2.2	The second rainbow	33
7.3	Beyond the geometrical optics	34
7.4	Conclusion	34
8	The free-electron laser <i>by Marcelo da Silva Cruz</i>	35
8.1	Introduction	35
8.1.1	A new kind of laser	35
8.2	Theoretical revision	36
8.3	The Stanford experiment	37
8.3.1	The coupled wave of FEL	37
8.3.2	Low-gain	38
8.3.3	High-gain	38
8.4	Modern applications	39
8.4.1	Optical guidance	39
8.4.2	Generation of radiation	39
8.5	Conclusion	40
9	Bremsstrahlung <i>by Nathan Barbola Marucci</i>	41
9.1	Introduction	41
9.2	Radiation emitted by a point charge	41
9.2.1	Distribution in Frequency and Angle of Energy Radiated by Accelerated Charges	42
9.3	Bremsstrahlung in Coulomb Collisions	43
9.4	X-rays	44
9.4.1	Generation of X-rays	44
9.4.2	X-ray Spectrum	45
9.5	Bremsstrahlung in Nuclear Decay	45
9.6	Conclusion	46
10	Cherenkov radiation <i>by Vinicius dos Santos Malafatti</i>	47
10.1	Introduction	47
10.2	Theory	47
10.2.1	Potentials and conditions for the emission	48
10.2.2	Radiated Energy	49
10.3	Applications	49
10.3.1	CTAO	50
10.4	Conclusion	50

11 Kerr Effect <i>by Vinicius Pereira Pinto</i>	52
11.1 Introduction	52
11.2 Third-order nonlinear processes	53
11.2.1 Symmetry effects	53
11.3 The DC Kerr Effect	53
11.4 The Optical Kerr Effect	54
11.4.1 Intensity-dependent refractive index	54
11.4.2 Refractive nonlinearities types	54
11.5 Nonlinear optical characterization	55
11.5.1 Nonlinear Interferometry	55
11.5.2 Z-scan	55
11.5.3 Discrimination of nonlinearities types	56
11.5.4 Other techniques	57
11.6 Kerr Effect application	57
11.6.1 Kerr-lens Modelocking	57
11.6.2 Kerr Effect on Bose–Einstein Condensates	57
11.7 Conclusion	57
12 The Drude model <i>by Willer Frank de Sousa Oliveira</i>	59
12.1 Introduction	59
12.2 Basic Assumptions of the Drude Model	59
12.3 A Mechanical Analogy for the Drude Model	61
12.4 Theory of Conduction in Metals	62
12.4.1 Conductivity and Electrical Resistivity	62
12.5 Application	63
12.6 Hall Effect	63
12.6.1 Electric charges in motion under the action of an external magnetic force	63
12.6.2 Effect of an external magnetic field on an electric current	63
12.7 Conclusion	65

Preface

Estes anais (ou proceedings) reúnem as monografias elaboradas pelos alunos do curso de Fundamentos da Interação da Radiação com a Matéria (SFI5905), realizado no Instituto de Física de São Carlos da Universidade de São Paulo durante o primeiro semestre de 2023 sob supervisão do Prof. Ph. W. Courteille.

1

The Goos-Hänchen shift

Anna Cristina Cavallari Inacio

Instituto de Física de São Carlos, Universidade de São Paulo, 13560-970 São Carlos, SP, Brazil

Abstract: The Goos-Hänchen shift is an optical phenomenon, first observed by Fritz Goos and Hilda Hänchen in 1947, that happens when linearly polarized light is totally internally reflected, suffering a small lateral shift. Since then the topic has been well studied by the scientific community, with several theoretical explanations, experiments and applications being developed over the years. This work aims to discuss one way to derive the mathematical expression of the shift through conservation of energy based on the work of René Renard. The work also aims to discuss one of the methods to directly measure the Goos-Hänchen shift developed by Fabien Bretenaker in 1992.

1.1 Introduction

Isaac Newton predicts in his work a lateral shift of a light beam when totally reflected from an interface to an optically thin media [1], however it was only observed many years later in 1947 by Fritz Goos and Hilda Hänchen. They developed the first experiments demonstrating the existence of the shift when linearly polarized light is totally internally reflected [2]. Since then the Goos-Hänchen effect has been a consistent object of research, guided either by a theoretical interest in understanding the physics of this phenomenon or experimental interest of finding new ways to measure or new applications. Some of the theories developed to explain this phenomena are the stationary-phase approach by Artmann and von Fragstein [3, 4], the imposition of energy conservation by Renard [5], both unified by Lotsch [6] in his work, time-delayed scattering processes by Chiu and Quinn [7], and angular spectrum approach developed by Brekhovskikh [8] and later by McGuirk and Carniglia [9]. With this studies, it was possible to understand the shift for others polarization, like the Imbert-Fedorov [10, 11] effect in which the shift

occurs for circularly and elliptically polarized light beam. Recently, research has been carried out on the Goos-Hänchen shift in a context of nanophotonics and biological applications, for example sensitive detection of biological molecules through the linear relation of the Goos-Hänchen shift measured and the concentration of target molecules [12]. There is also research about the generation of giant Goos-Hänchen shift using surface plasmon resonance techniques, allowing biological applications and the observations of important processes in the quantum information area [13].

This work aims to derive the Goos-Hänchen shift for a total internal reflection at a plane interface by the point of view of the conservation of energy, based on the work of Rémi Renard published in 1964 [5]. It also aims to discuss an experimental system for measuring the shift.

1.2 Goos-Hänchen shift for a planar surface

Considering two different non-absorbing mediums, the first one have a refractive index n_1 and the other one is a medium of refractive index n_2 , smaller than n_1 . Here we are going to study the case where a infinite plane wave is totally reflected from a plane interface between the two mediums, suffering a shift denominated d , as shown in Fig. 1.1. For the condition of total reflection be fulfilled, we assume the incident angle is greater than the critical angle.

The Fresnel-Maxwell treatment shows that there is an evanescent wave in the medium of index n_2 for the shift occur. This type of wave does not carry a time-averaged flux of energy across a plane parallel to the plane separating the two medias, which means it exists without dissipating energy. However, there is a time-averaged flux of energy carried

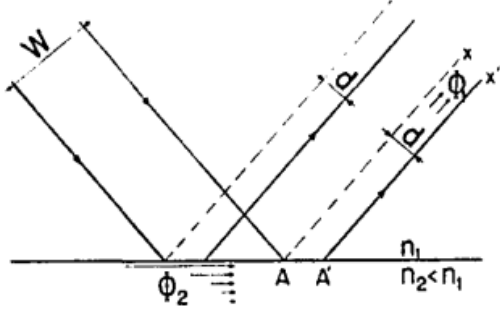


Figure 1.1: Illustration of the Goos-Hänchen shift for a finite plane wave. W is the incident plane wave. Φ_1 and Φ_2 are two fluxes of energy. The spacing d is the Goos-Hänchen shift. Source: R. Renard, 1964

by the evanescent wave across a plane that is perpendicular both to the plane separating the two medias and the plane of incidence. For escaping the contradiction this situation brings, we must consider a finite wave, in which energy is transferred from one side of the beam to the other [14] resulting in what is equivalent to the translation that produces the Goos-Hänchen shift.

There are two cases for linear polarization that are important to study. One that has the electric field perpendicular to the plane of incidence, also know as electrical transversal mode (TE), and one that has the electric field parallel to the plane of incidence, known as magnetic transverse mode (TM).

1.2.1 Case A: electric vector perpendicular to the plane of incidence

It is defined in literature [15] that the magnitude of the magnetic vector of the evanescent wave at the level of the plane separation between the two media and that the magnitude of the magnetic vector for the incident wave are

$$M_2^2 = \frac{64\pi^2 D_1^2}{K_1 \mu_1} \cdot \frac{\cos^2 \theta_i (2 \sin^2 \theta_1 - K\mu)}{\mu^2 \cos^2 \theta_i + \sin^2 \theta_i - K\mu} \quad (1.1)$$

$$M_1 = \frac{4\pi}{\sqrt{K_1 \mu_1}} D_1 \quad (1.2)$$

The time-average flux of energy across a plane surface perpendicular to \hat{x} , of width L in the direction of \hat{y} (see Fig. 1.2) is [16]

$$\Phi_2 = \frac{L}{32\pi^2} \left(\frac{\mu_2}{K_2} \right)^{1/2} \frac{1 - \gamma_2^2 \lambda_2}{1 + \gamma_2^2 \gamma_2} M_2^2 \quad (1.3)$$

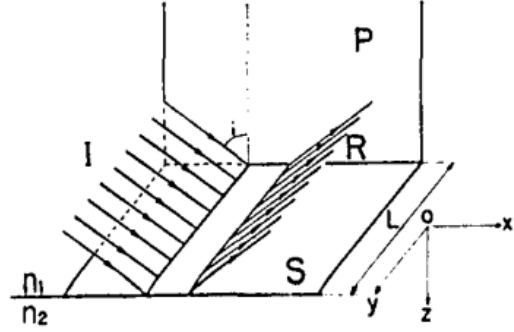


Figure 1.2: Illustration of the system of axes used in calculating the shift for a light beam of width L , incident at angle θ_i . I is the incident wave, R the reflected wave. S is the surface of separation between the two media and P is the plane of incidence. Source: R. Renard, 1964

where γ_2 is the damping factor of the evanescence wave defined by $\gamma_2^2 = 1 - n^2 / \sin^2 \theta_i$, with $n^2 = n_2^2 / n_1^2 = K_2 \mu_2 / K_1 \mu_1 = K\mu$ and $\lambda_2 = \lambda_{vacuum} / n_2$.

Using the Poynting vector it is possible to calculate the time average flux of energy of the plane wave, across a surface of area Ld , with d_{TE} being the Goos-Hänchen shift, perpendicular to the direction of propagation of the wave.

$$\Phi_1 = \frac{L d_{TE}}{8\pi} \left(\frac{\mu_1}{K_1} \right)^{1/2} M_1^2 \quad (1.4)$$

According to the principle of conservation of energy the two fluxes of energy must be equal. Taking $\Phi_1 = \Phi_2$ we can evaluate d_{TE}

$$d_{TE} = \frac{1}{\pi} \frac{\mu \sin \theta_i \cos^2 \theta_i}{\mu^2 \cos^2 \theta_i + \sin^2 \theta_i - n^2} \frac{\lambda_1}{\sqrt{\sin^2 \theta_i - n^2}} \quad (1.5)$$

We can reduce the Eq. (1.5) if we consider that the observation of the shift is near the critical angle of total reflection, so that $\sin \theta_i \simeq n$. We can also say that $\mu = 1$, since for most glasses that is practically true. This way we have the expression

$$d_{TE} \simeq \frac{\sin \theta_i}{\pi} \frac{\lambda_1}{\sqrt{\sin^2 \theta_i - n^2}} \quad (1.6)$$

The Eq. (1.6) is the same expression derived by Artmann and von Fragstein [3, 4].

1.2.2 Case B: electric vector parallel to the plane of incidence

It is a know result in literature [15] that for Case b, which the electric vector is parallel to the plane

of incidence, the result is analogous to Case a, only needing to permute μ and K . Thus, the Goos-Hänchen shift for Case b is

$$d_{TM} = \frac{1}{\pi} \frac{K \sin \theta_i \cos^2 \theta_i}{K^2 \cos^2 \theta_i + \sin^2 \theta_i - n^2} \frac{\lambda_1}{\sqrt{\sin^2 \theta_i - n^2}} \quad (1.7)$$

Using the same approximation for $\sin \theta_i \simeq n$ as before and using that $n^2 = K$ for glasses in Eq. 1.7, we get the expression

$$d_{TM} \simeq \frac{\sin \theta_i}{\pi n^2} \frac{\lambda_1}{\sqrt{\sin^2 \theta_i - n^2}} \quad (1.8)$$

The Eq. 1.8 is the same expression for the shift derived by Artmann and von Fragstein [3, 4].

Renard [5] discuss in his work that when the angle of incidence is $\pi/2$ the shifts d_{TE} and d_{TM} must be zero because in this case the incident and reflected beams are co-linear. For the expressions 1.8 and 1.6, derived by Artmann and von Fragstein [3, 4], this result does not happen when the angle tends to $\pi/2$, showing that, although at first, these expressions seem strictly correct, they are limited to some specific cases. Is important to say that the Renard's derivation is also limited, in his own work it is discussed that there are some divergences between the experimental results obtained by Goos and Hänchen [2] and those obtained theoretically by his equations. Till this day the Goos-Hänchen shift is studied for different limits and situations, for example absorbing medias, metallic reflection and negative Goos-Hänchen shift, and new expression for describing the shift are still being discussed by the scientific community.

1.3 Measuring the Goos-Hänchen shift

There are many measurements of the Goos-Hänchen shift that were achieved along of the years. Goos and Hänchen [2] were the first to measure in 1947, they compared the total reflection from a prism with the reflection from a silver stripe deposited on the back of the prism. To be able to measure the effect, since it is very small, they multiple the relative shift between the two reflections using an waveguide. This experiment was latter refine to a better resolution and to distinguish the difference between the shifts of the TE and TM polarization [17]. In 1972, Imbert [10] was able to observe a lateral shift for light circularly polarized foreseen by Fedorov [11] in 1955, coining the name

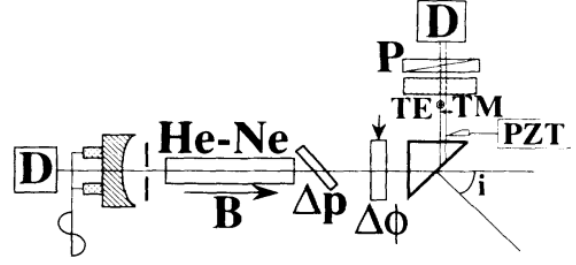


Figure 1.3: Experimental setup. Source: Brekhovskikh, 1960

Imbert-Fedorov shift. In 1977, Cowan and Anicin [18] did an experiment to observe the Goos-Hänchen shift for microwave radiation using a paraffin prism and single reflection of the beam. In 1992, Bretenaker measured the shift for both polarization using a single reflection and a He-Ne cavity field. Latter in 2008, Schwefel [19] used a method very similar to the the one Goos and Hänchen used, but with a glass half-cylinder and a 'partially coherent LED light source to measure the effect for a single reflection for TE and TM polarization for all angles of incidence.

In this work we are going to discuss the experiment set up by Bretenaker in 1992. This experimental method uses the high sensitivity of the eigenstates of a quasi-isotropic laser to small perturbations to measure the Goos-Hänchen effect for angles of incidence both below and above the critical angle [13]. A HeNe laser is oscillating at $\lambda_0 = 3.39 \mu m$. The cavity is built with a plane mirror and a spherical mirror and it contains a silica prism responsible for the total reflection for angles of incidence above the critical angle $\theta_c = 45, 212$. The reflection on the prism leads to the spatially separation of TE and TM eigenstates. For measuring the Goos-Hänchen shift, is necessary to have a knife edge inside the cavity. Because of the spatial separation between the two eigenstates, the diffraction losses due to this knife edge are different for TE and TM, which leads to a modulation of the total intensity of the laser when the linear polarization rotates. This we have that the polarization effect is transformed into an intensity effect. The knife edge is controlled by a piezoelectric transducer. The experimental apparatus is shown in Fig. 1.3

The results obtained by this experiment, as shown in Fig 1.4, are consistent with the values obtained by calculations with the Artmann's formulas previously showed and discussed in this work.

1.4 Conclusion

Since the Goos-Hänchen shift was first observed in 1947, a lot has been discovered about this phenomenon. Although it has been developed a lot of theories that explain the shift for different situations and the respective experiments able to observe it, exploring several limits, medias and polarization, there still a lot to be discovered about this effect and its applications. We hope that in the next years the researchers being conducted in the moment, like using the shift to detect biological molecules and the studies about the generation of a giant Goos-Hänchen shift, present good results and can be increasingly refined with the help of new technologies.

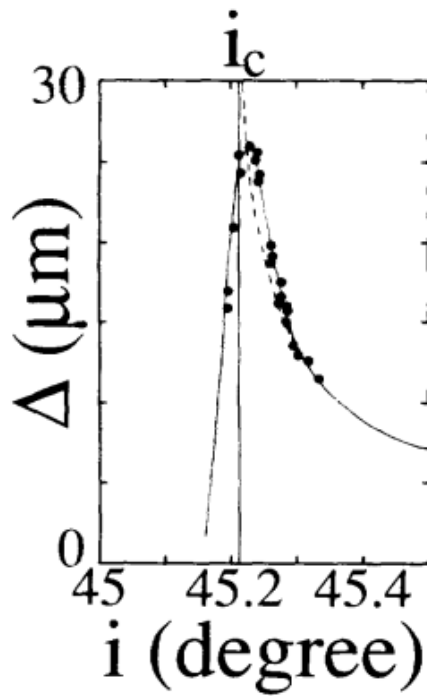


Figure 1.4: Difference between the TE and TM Goos-Hänchen shifts vs the angle of incidence. Solid line represents theory; dotted line represents the Artmann's formulas and the points the experimental measurements. Source: Brekhovskikh, 1960

Bibliografia

- [1] I. Newton *Opticks*. Prabhat Prakashan, (1730).
- [2] F. Goos and H.L. Hänchen *Neumessung des strahlversetzungseffektes bei totalreflexion*. Annalen der Physik, **440(3-5)**, 251-252 (1949).
- [3] K. Artmann. *Berechnung der Seitenversetzung des totalreflektierten Strahles*. Annalen Der Physik, **437(1-2)**, 87-102. (1948).
- [4] C. Von Fragstein. *The sideways displacement of totally reflected light*. Annalen Der Physik (Leipzig), **4**, 271. (1949).
- [5] R.H. Renard. *Total reflection: A new evaluation of the Goos-Hänchen shift*. Journal of the Optical Society of America, **54**, 1190-1197. (1964).
- [6] H.KV. Lotsch. *Beam displacement at total reflection: The Goos-Hänchen effect I*. Optik **32(2)**, 116-137. (1970).
- [7] K.W. Chiu and J.J. Quinn. *On the Goos-Hänchen effect: a simple example of a time delay scattering process*. American Journal of Physics, **40(12)**, 1847-1851. (1972).
- [8] L. Brekhovskikh. *Waves in Layered Media*. Academic Press, New York, 100-122. (1960).
- [9] M. McGuirk and C. Carniglia, *An angular spectrum representation approach to the Goos-Hänchen shift*. Journal of the Optical Society of America, **67**, 103-107. (1977).

- [10] C. Imbert. *Calculation and experimental proof of the transverse shift induced by total internal reflection of a circularly polarized light beam.* Physical Review D, **5(4)**, 787. (1972).
- [11] F.I. Fedorov. *K teorii polnogo otrazheniya.* Doklady Akademii Nauk SSSR, **106(3)**, 465-468. (1955).
- [12] L. Jiang and et al. *Multifunctional hyperbolic nanogroove metasurface for submolecular detection.* Small, **13(30)**, 1-7. (2017).
- [13] X. Yin *Photonic spin Hall effect at metasurfaces.* Science, **339(6126)**, 1405-1407. (2015).
- [14] C. Schaefer and R. Pich. *A contribution to the theory of total reflection* Annalen der Physik, **30**, 245. (1937).
- [15] H. Arzelies, Annalen der Physik, (Paris), **12/1**, 5. (1946).
- [16] H. Arzelies. *Propriétés de l'onde évanescente obtenue par réflexion totale.* Rev. Opt., **27**, 205. (1948).
- [17] H. Wolter. *Zur Frage des Lichtweges bei Totalreflexion.* Zeitschrift für Naturforschung A, **5(5)**, 276-283. (1950).
- [18] J.J. Cowan and B. Aničin. *Longitudinal and transverse displacements of a bounded microwave beam at total internal reflection.* Journal of the Optical Society of America, **67**, 1307-1314. (1977).
- [19] H.G.L. Schwefel and et al. *Direct experimental observation of the single reflection optical Goos-Hänchen shift.* Optics Letters, **33**, 794-796. (2008).
- [20] F. de Fornel. *Evanescent Waves: From Newtonian Optics to Atomic Optics.* Springer. (2001).

2

Emission of radiation by a charged particle in gravity

Bruno Trebbi

Instituto de Física de São Carlos, Universidade de São Paulo, 13560-970 São Carlos, SP, Brazil

Abstract: Born's 1909 paper initiated a debate among physicists about whether relativistic uniformly accelerated charges radiate. The solution needs to be theoretical, as experimental validation is challenging due to the Larmor formula. The answer is related to questions about the Equivalence Principle, motion of free-falling bodies, radiation's absoluteness, and energy conservation. This monograph seeks to elucidate these fundamental inquiries with the restriction that we assume charges in gravitational fields following geodesic paths.

2.1 Introduction

2.1.1 Contextualization and History of the problem

After an article published in 1909 by Max born, named "*The Theorie des starren Elektrons in der Kinematik des Relativitätssprinzips*" [1], where he derived the electromagnetic fields of a relativistic uniformly accelerated charge, important physicists such as Pauli (known for Pauli's Exclusion Principle), and von Laue (known for X-ray diffraction), concluded that such charges could not radiate [5]. Others, such as Schott and Milner, argued that the charge would radiate [5].

This problem has persisted for decades, and recent contributions to its resolution (including references [2, 3, 4]) date back to the last decade. This not only underscores the contentious nature of the problem but also highlights that its underlying complexities are not as straightforward as they may initially appear.

Usually, when such theoretical problems appear impossible to solve, experimentalists appears with an experimental apparatus that will end the con-

troversy, but this problem, in specific, requires unpractical precision in the measurement of radiated power, because, as stated by Larmor formula, showed in equation (2.1), where P is the power radiated by the accelerated particle, with electric charge q is and velocity \vec{v} :

$$P = \frac{2q^2 \langle \dot{\vec{v}}, \dot{\vec{v}} \rangle}{3c^3(4\pi\epsilon_0)}, \quad (2.1)$$

in Earth's gravitational field, where $\langle \dot{\vec{v}}, \dot{\vec{v}} \rangle \approx 10^2 \frac{m^2}{s^4}$, one electron would radiate $P \approx 5.5 \cdot 10^{-52} W$ [2]. This shows that we would need a very high number of electrons, and a way to isolate them from induced charges, so that the electrostatic force would be much weaker than the gravitational. This means that the problem need to be done theoretically, as the experiment by itself is almost impossible.

It's really important to understand that this problem isn't just a casual curiosity. It's connected to some fascinating questions [2], like whether Einstein's Equivalence Principle holds true, whether a chargeless object falls faster, if radiation is absolute, if a stationary charge in a gravity field emits radiation, and whether the law of energy conservation is legit.

In this monograph, these questions will be answered, and to start, we need to clarify what is Einstein's Equivalence Principle.

2.1.2 The equivalence principle

Let's begin with a Gedankenexperiment: imagine you are traveling across the stars in a spaceship with no windows. Because you have been traveling for so much time, you don't know where you are, nor if there are any astronomical body close to you. In your pocket, there is an accelerometer, which can

measure your proper acceleration. One day, you wake up and do a daily check, but this time, you see that your accelerometer is measuring a nonzero constant acceleration. Because there is no windows, you don't know if you are at rest w.r.t. an unknown planet or if your engines suddenly turned on (they don't make noise).

This conclusion is self-evident, as it aligns with classical mechanics. In classical mechanics, Newton's Second Law dictates that the sum of external forces acting on an object equates to the product of its mass and acceleration. Moreover, experimental verification has consistently shown the equivalence of inertial and gravitational mass, which makes it easy to conclude that the astronaut won't be able to say whether it is being accelerated by its engine with acceleration $-\vec{a}$, or whether it is **at rest** in a planet's gravitational field (here assumed to be uniform and homogeneous), with acceleration \vec{a} , as seen in figure (2.1):

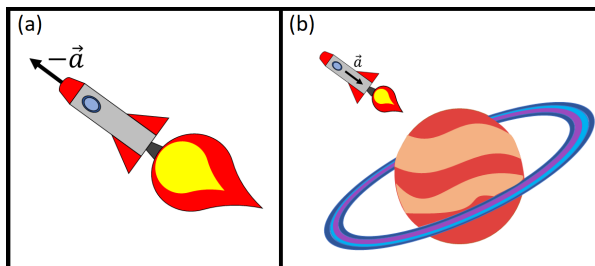


Figure 2.1: In the case (a), we see the spaceship is accelerating with acceleration $-\vec{a}$ in free space, whereas in case (b), the spaceship is **at rest** w.r.t. a unknown planet with acceleration \vec{a} , the astronaut would only be able to differ the situation if he look through the window.

This is the so called equivalence principle in classical mechanics. Albert Einstein extended this principle, formulating the so called strong Einstein's Equivalence Principle, which is one of the most important concept in the General Relativity Theory [2]:

The motion of a small test body due to gravity depends only on its initial conditions and not on its constitution and the outcome of any local experiment in a freely falling laboratory is independent of the velocity of the laboratory and its location in spacetime.

This means, not only that locally, the effects of gravity are indistinguishable from the effects of acceleration, but also, that every law of nature is the same in free falling particles (those which are falling in homogeneous gravitational fields), which includes

the laws of electromagnetism.

With that in mind, we can now identify the apparent paradox.

2.2 The apparent physical paradox

According to Einstein's Equivalence Principle, a particle at rest in a homogeneous gravitational field of acceleration \vec{g} is equivalent to the same charged particle accelerated with acceleration $-\vec{g}$, whereas a free falling charged particle in the same homogeneous gravitational field is equivalent to a non-accelerating particle, therefore, if Einstein's Equivalence Principle is true, a free falling charge doesn't radiate, but a particle at rest does^[1].

Now, in the reference frame of the resting particle, the free falling particle is accelerated, so it should radiate, what happened to Larmor formula? And also, in the reference frame of an observer also at rest close to the charged particle it cannot radiate, because it has no acceleration, and if it radiated, the energy wouldn't be conserved, as it has the same height, so it didn't change its potential energy. It seems like Einstein's Equivalence Principle is incompatible with Larmor formula.

The solution of this "paradox" came with Rohrlich [5] and Fulton and is as follows:

1. **For a comoving reference frame with respect to the free falling charge:**
 - (a) The free falling charge does not radiate,
 - (b) The rest charge does radiate,
2. **For a reference frame at rest with respect to the rest charge:**
 - (a) The free falling charge does radiate,
 - (b) The rest charge does not radiate,

In the end there is no paradox, because, as will be shown in the latter sections, there is an event horizon called Rindler-Horizon that makes it impossible for an observer at rest, with respect to the rest or free falling charge, to detect any radiation due to

¹This is not correct, because I assume the motion of the charge in a gravitational field is a geodesic beforehand, therefore it should be an inertial frame, whereas the charge at rest would be a uniformly accelerating reference frame. In reality, a charge and its field interacting with a gravitational field does not necessarily follow a geodesic, because it would be moving under the DeWitt-Brehme radiation reaction force [6] and, therefore, would probably radiate. But this would be impossible for me to calculate at my level of knowledge considering the short time I have to finish this.

the charge he sees at rest. For that, the observer will see a electrostatic field. Of course we still have to say some words about the conservation of energy, but this will be done latter. So basically, there will only be radiation when the charge is accelerating with respect to the observer.

For now, lets review the mathematics of an accelerating reference frame in special relativity in order to obtain the solution above.

2.3 Can Special Relativity Handle Acceleration?

If you interacted enough in a physics department, you probably heard at least one time: "Special relativity can't handle acceleration, for that you need to use general relativity". This sentence is wrong, because although special relativity is incompatible with gravity, it is possible to treat accelerated particles.

Differently from classical mechanics, where a uniformly accelerated particle follows a parabola in the spacetime diagram, in special relativity it would mean that eventually, the body would have speed greater than light, which is impossible. Therefore, it is intuitive that the curve an uniformly accelerated body will have in the spacetime diagram, will have asymptotes, where we should get $v \rightarrow c$ when $t \rightarrow \infty$, as we can see in figure (2.2) It happens that this curve is also a conic, more specifically, an hyperbole, as we are going to show in the next subsection.

2.3.1 Hyperbolic Motion

To proof that the motion is hyperbolic, it will be interesting to follow three steps:

1. First, we proof that the 4-velocity is normalized, i.e. $u_\mu u^\mu = c^2$ [2];
2. Second, we proof that the first item implies that the 4-acceleration is perpendicular to the 4-velocity, i.e. $u_\mu a^\mu = 0$;
3. Third, and last, we impose that the norm of the 4-acceleration is a constant, i.e. $a_\mu a^\mu = -\alpha^2$.

Lemma 2.3.1. *The four velocity of a particle is normalized to c^2 [3].*

²Remember that $u_\mu u^\mu = \sum_{\mu=0}^3 u_\mu u^\mu$

³Some textbooks use $c = 1$, that's why some say the 4-velocity is normalized. Mathematically, a unit speed curve – which is one that has the first derivative norm equals to one – has some advantages, especially when finding the Frenet-Serret formulas, see [8]

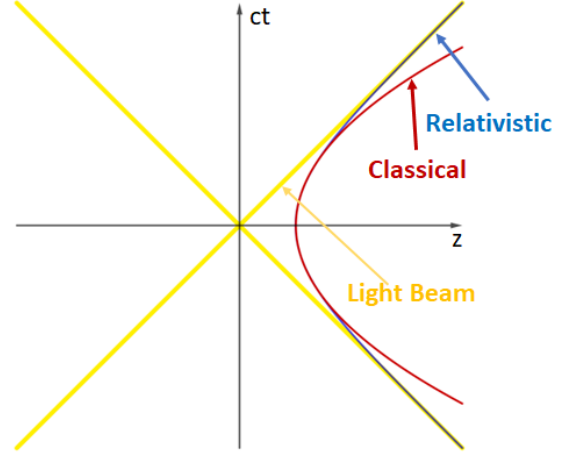


Figure 2.2: In classical mechanics, there is no maximum possible speed, therefore, the slope of the spacetime trajectory can increase as much as you wish, whereas in special relativity, the maximum speed possible is the speed of light in vacuum, c , so the trajectory should have an maximum slope (mathematically, we say that $t(z) = c \frac{z}{c}$ is an asymptote of our trajectory curve).

Proof. By definition, the 4-velocity is the derivative of the 4-position in relation to the proper time τ :

$$u^\mu = \frac{dx^\mu}{dt} \frac{dt}{d\tau}. \quad (2.2)$$

The covariant 4-velocity can be obtained using the metric of spacetime, which in this case is the Minkowski metric:

$$u_\mu = g_{\mu\nu} u^\nu = \eta_{\mu\nu} \frac{dx^\nu}{dt} \frac{dt}{d\tau}. \quad (2.3)$$

The squared norm of the 4-velocity is given by the calculation bellow:

$$u^\mu u_\mu = g_{\nu\mu} u^\mu = \eta_{\nu\mu} \frac{dx^\nu}{dt} \frac{dx^\mu}{dt} \left(\frac{dt}{d\tau} \right)^2, \quad (2.4)$$

where we remember that the proper time is, by definition

$$\gamma d\tau = dt \Rightarrow \frac{dt}{d\tau} = \gamma. \quad (2.5)$$

With this, one can simply calculate

$$u^\mu u_\mu = c^2 (1 - \beta_x^2 - \beta_y^2 - \beta_z^2) \gamma^2 \quad (2.6)$$

Notice that $(1 - \beta_x^2 - \beta_y^2 - \beta_z^2) = \gamma^{-2}$, therefore,

$$u^\mu u_\mu = c^2, \quad (2.7)$$

which concludes the demonstration. \square

Corollary 2.3.1.1. *The 4-acceleration is perpendicular to the 4-velocity.*

Proof. As a consequence of lemma (2.3.1), we have that the derivative of $u_\mu u^\mu = 0$, because it is a constant, but, we also have that:

$$\frac{d}{d\tau} (u_\mu u^\mu) = \frac{du_\mu}{d\tau} u^\mu + u_\mu \frac{du^\mu}{d\tau} = 0. \quad (2.8)$$

Because the Minkowski metric is constant, we have,

$$\frac{du_\mu}{d\tau} u^\mu = \frac{dg_{\mu\nu} u^\nu}{d\tau} u^\mu \Rightarrow \frac{du_\mu}{d\tau} u^\mu = \eta_{\mu\nu} \frac{du^\nu}{d\tau} u^\mu. \quad (2.9)$$

Going back to the product rule,

$$\frac{d}{d\tau} (u_\mu u^\mu) = \eta_{\mu\nu} \frac{du^\nu}{d\tau} u^\mu + u_\mu \frac{du^\mu}{d\tau}. \quad (2.10)$$

Factorizing the metric,

$$\frac{d}{d\tau} (u_\mu u^\mu) = \eta_{\mu\nu} \left(\frac{du^\nu}{d\tau} u^\mu + u^\nu \frac{du^\mu}{d\tau} \right). \quad (2.11)$$

Changing the dummy indices, we get,

$$\frac{d}{d\tau} (u_\mu u^\mu) = 2\eta_{\mu\nu} \frac{du^\nu}{d\tau} u^\mu = 0. \quad (2.12)$$

Identifying the 4-acceleration – which is the derivative of the 4-velocity with respect to the proper time,

$$2\eta_{\mu\nu} \frac{du^\nu}{d\tau} u^\mu = 2\eta_{\mu\nu} a^\nu u^\mu = 0. \quad (2.13)$$

To end, we just need to identify the scalar product, which is zero

$$2\eta_{\mu\nu} a^\nu u^\mu = 2a_\mu u^\mu = 0 \Leftrightarrow a_\mu u^\mu = 0. \quad (2.14)$$

Therefore, the 4-velocity is perpendicular to the 4-acceleration. \square

With this, in order to get the hyperbolic motion, we are going to assume that the particle is moving in a uniformly accelerated motion in the x^3 direction, so that $u^1 = u^2 = 0 = a^1 = a^2$.

Because this acceleration is constant,

$$a_\mu a^\mu = -\alpha^2 \Leftrightarrow -a_0 a^0 + a_3 a^3 = -\alpha^2, \quad (2.15)$$

But, from lemma (2.3.1) and corollary (2.3.1.1),

$$\begin{cases} u_0 u^0 - u_3 u^3 = c^2 \\ a_0 u^0 - a_3 u^3 = 0 \\ -\alpha^2 = a_0 a^0 - a_3 a^3 \end{cases} \Rightarrow \begin{cases} c^2 a^0 = \alpha^2 u^3 \\ c^2 a^3 = \alpha^2 u^0 \end{cases}. \quad (2.16)$$

This gives us two coupled differential equation:

$$\begin{cases} \frac{du^0}{d\tau} = \frac{\alpha}{c} u^3 \\ \frac{du^3}{d\tau} = \frac{\alpha}{c} u^0 \end{cases} \Leftrightarrow \frac{d^2 u^3}{d\tau^2} = \frac{\alpha^2}{c^2} u^3. \quad (2.17)$$

The solution of this ODE, with the restrictions, is given by

$$\begin{cases} u^0 = c \cosh\left(\frac{\alpha}{c}\tau\right) \\ u^3 = c \sinh\left(\frac{\alpha}{c}\tau\right) \end{cases}. \quad (2.18)$$

This gives a hyperbole in spacetime, as expected.

2.3.2 Rindler Horizon

Because the particle is accelerating constantly, following an hyperbolic motion, an artificial^[4] event horizon is created in a region of spacetime – the Rindler Horizon – the light beams passing by this region will never interfere with the particle, it appears for the particle as a dark region, because the light beams never reach it, as shown if figure (2.3).

For an observer at rest, it is clear in figure (2.3) that the distance from the particle and its Rindler horizon is increasing, but for the accelerated particle, due to length contraction, the distance is constant. To show that, one can find the 4-position and calculate its contraction:

$$r^0 = \int d\tau c \cosh\left(\frac{\alpha}{c}\tau\right) = \frac{c^2}{\alpha} \sinh\left(\frac{\alpha}{c}\tau\right), \quad (2.19)$$

and also,

$$r^3 = \int d\tau c \sinh\left(\frac{\alpha}{c}\tau\right) = \frac{c^2}{\alpha} \cosh\left(\frac{\alpha}{c}\tau\right). \quad (2.20)$$

Therefore,

$$r_\mu r^\mu = \frac{c^4}{\alpha^2} \left[\sinh^2\left(\frac{\alpha}{c}\tau\right) - \cosh^2\left(\frac{\alpha}{c}\tau\right) \right] = -\frac{c^4}{\alpha^2} \quad (2.21)$$

This seems useless, but notice that a light beam is always at the same distance from the particle (Rindler distance), which means that the speed of light for non inertial reference frames is different from c , i.e. zero for uniformly accelerated charges. Now we are ready to do the calculation and see if the observer will detect any radiation.

⁴I'm calling it artificial, because, differently from the black holes event horizon, if the acceleration is turned off, the light beams can reach the particle once again, so the event horizon remains only while the particle is accelerated.

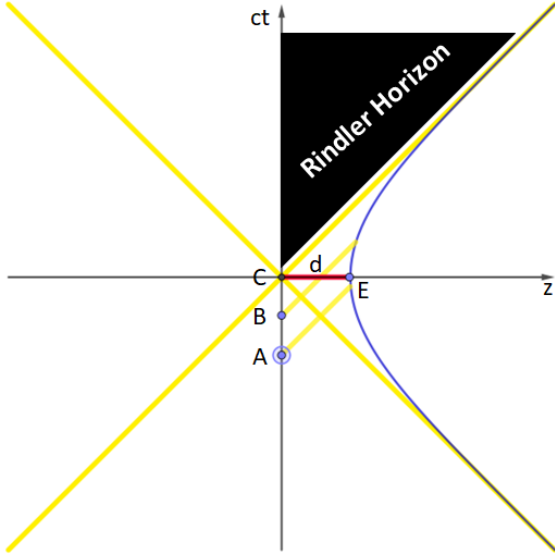


Figure 2.3: We see a uniformly accelerated particle with a hyperbolic motion in spacetime. Observe that the light beam emitted at the points A and B reach the particle, whereas the light beam emitted by C will never reach it. It's visually easy to see the Rindler Horizon. We call the distance d the Rindler distance, which is the distance from the particle and the Rindler horizon.

2.4 The radiation seen by the Minkowski reference frame

To start, we are going to see what an comoving observer with the free falling charge will see when looking to the charge at rest (remember that everything passes as if the charge is uniformly accelerated, also, remember that the observer at rest with respect to the charge at rest will have the same conclusion when doing the analysis of the free falling charge).

For those, we use the Minkowski metric $ds^2 = \eta_{\nu\mu} dx^\mu dx^\nu$ and solve the Maxwell equations according to [7] :

$$\begin{cases} \partial_\mu F_{\nu\xi} + \partial_\nu F_{\xi\mu} + \partial_\xi F_{\mu\nu} = 0 \\ \frac{1}{\sqrt{G}} \partial_\mu (\sqrt{G} F^{\mu\nu}) = \frac{4\pi}{c} J^\nu \end{cases}, \quad (2.22)$$

where G is the determinant of $G_{\mu\nu} = \eta_{\mu\nu}$, and the current density J^ν is given by [7]:

$$J^\nu = ec \int d\tau u^\nu \delta^{(4)}(x - r(\tau)) \quad (2.23)$$

The solution can be found using Green function

as done in [7, 3]:

$$F^{\mu\nu} = e \left[\frac{1}{u^\xi (x_\xi - r_\xi)} \frac{d}{d\tau} \left(\frac{(x^\mu - r^\mu) u^\nu - (x^\nu - r^\nu) u^\mu}{u^\xi (x_\xi - r_\xi)} \right) \right]_{\tau=\tau_{ret}}, \quad (2.24)$$

where τ_{ret} is the retarded time, x^μ is an event of spacetime and r^μ is the 4-position of the accelerated particle (already calculated).

The retarded time, between an event x^μ and r^μ is a light-like interval, i.e. $(x_\mu - r_\mu)(x^\mu - r^\mu) = 0$,^[5] therefore, considering an event $x^\mu = (ct, x, y, z)$, we have $x^\mu - r^\mu = \left(ct - \frac{c^2}{\alpha} \sinh\left(\frac{\alpha}{c} \tau_{ret}\right), x, y, z - \frac{c^2}{\alpha} \cosh\left(\frac{\alpha}{c} \tau_{ret}\right) \right)$ and with that the retarded time is well defined as follows:

$$(x_\mu - r_\mu)(x^\mu - r^\mu) = 0 \Leftrightarrow$$

$$z \cosh\left(\frac{\alpha}{c} \tau_{ret}\right) - ct \sinh\left(\frac{\alpha}{c} \tau_{ret}\right) = \frac{\alpha}{2} \left(\frac{x^2 + y^2 + z^2}{c^2} - t^2 + \frac{c^2}{g^2} \right). \quad (2.25)$$

With this, it is easy to show that, because $u^\mu (x_\mu - r_\mu) = u^0 (x_0 - r_0) - u^3 (x_3 - r_3)$, then,

$$u^\mu (x_\mu - r_\mu) = c \left(ct \cosh\left(\frac{\alpha}{c} \tau\right) - z \sinh\left(\frac{\alpha}{c} \tau\right) \right), \quad (2.26)$$

and with this, we can calculate the electromagnetic fields. I'll show the example of B_x , and then write the answer for the others.

$$B_x = -F^{23} = \left[\frac{-e}{u^\xi (x_\xi - r_\xi)} \frac{d}{d\tau} \left(\frac{(x^2 - r^2) u^3 - (x^3 - r^3) u^2}{u^\xi (x_\xi - r_\xi)} \right) \right]_{\tau=\tau_{ret}} \quad (2.27)$$

In the denominator, we see equation (2.26) which I'll call ζ . Now we remember that $r^2 = 0 = u^2$, therefore,

$$\begin{aligned} B_x &= \left[\frac{-eyc}{\zeta} \frac{d}{d\tau} \left(\frac{\sinh\left(\frac{\alpha}{c} \tau\right)}{\zeta} \right) \right]_{\tau=\tau_{ret}} \quad (2.28) \\ &= \left[\frac{-eycat}{\left(ct \cosh\left(\frac{\alpha}{c} \tau_{ret}\right) - z \sinh\left(\frac{\alpha}{c} \tau_{ret}\right) \right)} \right]. \end{aligned}$$

Calculating the others, we see $B_z = 0$, $B_y = -\frac{x}{y} B_x$, $E_x = \frac{x}{y} E_y$ and, finally,

$$E_y = \frac{eE_z}{\alpha \left(\frac{x^2 + y^2}{c^2} - t^2 \right)^2 - \frac{c^4}{\alpha^2}} \quad (2.29)$$

The radiation field can be further extracted by taking terms that drop as $1/R$.

⁵In our choice of metric (+ - - -), a space-like interval has $\Delta S < 0$, a timelike interval has $\Delta S > 0$ and a light-like interval has $\Delta S = 0$.

2.5 Radiation seen by the co-moving reference frame

According to an accelerated observer w.r.t. a charge, the coordinates of an inertial observer is given by:

$$\begin{cases} t = \sqrt{\frac{2\xi}{\alpha}} \sinh\left(\frac{\alpha}{c}\tau\right) \\ z = \sqrt{c\frac{2\xi}{\alpha}} \cosh\left(\frac{\alpha}{c}\tau\right) \end{cases}. \quad (2.30)$$

Therefore, we can write the metric as

$$ds^2 = 2\alpha R d\tau^2 - dx^2 - dy^2 - \frac{c^2}{2\alpha R} dR^2. \quad (2.31)$$

With that, we can calculate the fields, remembering that they transform as given by equation (2.32)

$$F'^{\mu\nu} = \frac{\partial x'^{\mu}}{\partial x^{\zeta}} \frac{\partial x'^{\nu}}{\partial x^{\eta}} F^{\zeta\eta}. \quad (2.32)$$

So, we just need to calculate some partial derivatives and get the fields

$$\begin{cases} \frac{\partial \tau}{\partial t} = \frac{z}{2\xi}; \quad \frac{\partial \xi}{\partial t} = -\alpha t \\ \frac{\partial \tau}{\partial z} = \frac{-t}{2\xi}; \quad \frac{\partial \xi}{\partial z} = \frac{z\alpha}{c^2} \end{cases}. \quad (2.33)$$

Calculating the magnetic field components, we get $B'_z = 0$ and also, according to [3],

$$F'^{13} = \frac{y}{x} F'^{23} = \frac{e\alpha}{c^2 \zeta^3} \left(\frac{1}{c} \frac{\partial \xi}{\partial t} + ct \frac{\partial \xi}{\partial z} \right) = 0, \quad (2.34)$$

so, $B_x = B_y = B_z = 0$. For the electric fields, one can calculate by the same technique and get, as we see in [3],

$$\partial_0 F'^{01} = \partial_0 F'^{02} = \partial_0 F'^{03} = 0. \quad (2.35)$$

This results show that no radiation is observed in this reference frame, as is expected.

2.6 What about the energy?

For the observer at rest in respect to the emitting charge, the free falling observer that detect radiation would be taking energy out of nowhere, to solve this problem, [2] argued that it should deaccelerate to conserve energy, and everything passes as if the kinetic energy was converted to electromagnetic energy. In the end the gravitational field loses energy

and this energy is converted to electromagnetic radiation. Although this apparently solves the problem, the fact that we are treating radiation classically, can't explain the conservation of energy in the case that the charge is not detected, for that a proper quantum electrodynamics treatment would be necessary.

2.7 Conclusions

The debate about whether relativistic uniformly accelerated charges emit radiation has a incredible history and deals with fundamental physics questions. As we saw, there is no paradox and the Equivalence Principle's validity is once again proofed, using the concept of a Rindler horizon to explain why charged particles seemingly do not radiate while accelerating, when seen by observers at rest in relation to it. Despite of this success, the conservation of energy still appears to be in doubt, probably because we are using classical model of radiation instead of the QED model. Remember that all of this discussion is only possible if we assume that charges move along geodesic paths in the gravitational field, which is not true.

Bibliografia

- [1] Born, Max. "Die Theorie des starren Elektrons in der Kinematik des Relativitätsprinzips." *Annalen der Physik* 335.11 (1909): 1-56.
- [2] Gründler, Gerold. "Electrical charges in gravitational fields, and Einstein's equivalence principle." arXiv preprint arXiv:1509.08757 (2015).
- [3] De Almeida, Camila, and Alberto Saa. "The radiation of a uniformly accelerated charge is beyond the horizon: A simple derivation." *American Journal of Physics* 74.2 (2006): 154-158.
- [4] Rinehart, Luther. "Radiation from an accelerating charge in a family of Rindler frames." arXiv preprint arXiv:2211.02958 (2022).
- [5] Fulton, Thomas, and Fritz Rohrlich. "Classical radiation from a uniformly accelerated charge." *Annals of Physics* 9.4 (1960): 499-517.
- [6] DeWitt, Bryce S., and Robert W. Brehme. "Radiation damping in a gravitational field." *Annals of Physics* 9.2 (1960): 220-259.
- [7] Jackson, John David. "Classical electrodynamics." (1999): 841-842.
- [8] Oprea, John. *Differential geometry and its applications*. MAA, 2007.

3

Magnetic monopoles

Diego França de Oliveira

Instituto de Física de São Carlos, Universidade de São Paulo, 13560-970 São Carlos, SP, Brazil

Abstract: The supposed existence of magnetic monopoles will be assessed, from three different perspectives. First, from a theoretical perspective, quantum and electrodynamics theory will be discussed, exploring how magnetic monopoles could exist and their relation to the quantization of charge. A little will be discussed about the Higgs field and the Grand Unified Theories, as some of the monopoles most interesting characteristics come only by that means. Second, the journey of looking for monopoles will be explored, including some of the experiments that try to detect them, and it will be shown why, even if monopoles do exist, we may never see one. Lastly, one of the current attempts to create magnetic monopoles in the LHC particle accelerator will be shown.

3.1 Introduction

In the theory of electrodynamics, Maxwell's equations for the electric and magnetic fields have a clear symmetry. However, due to the existence of electric charges and the absence of their magnetic counterparts, this symmetry is completely lost in their presence. Suppose magnetic monopoles were real and acted in correspondence with electric monopoles, bringing back the symmetry. Maxwell's equations, in the gaussian unit system, would have the form:

$$\begin{aligned}\nabla \cdot \vec{E} &= 4\pi\rho_e; & \nabla \times \vec{E} &= \frac{1}{c} \frac{\partial \vec{B}}{\partial t} + \frac{4\pi}{c} \vec{j}_m \\ \nabla \cdot \vec{B} &= 4\pi\rho_m; & \nabla \times \vec{B} &= \frac{1}{c} \frac{\partial \vec{E}}{\partial t} + \frac{4\pi}{c} \vec{j}_e\end{aligned}\quad (3.1)$$

In these equations, \vec{E} and \vec{B} are the electric and magnetic fields as usual, while ρ and j are the density of charge and density of current, which can be either of electric (ρ_e, \vec{j}_e) or magnetic charge (ρ_m, \vec{j}_m).

In this work, the Gaussian unit system will be primarily used, as it is the system utilized in most of the original articles used as reference. Many of the concepts revolving around the theme of magnetic monopoles go beyond the electrodynamics course description and were made as simplified as possible for didactic purposes. Most of the references used are from the original papers and can be consulted if one wishes to delve deeper into the formalism of such theories.

Let's try and predict if such monopoles could exist and how should they be.

3.2 Predicting monopoles

3.2.1 Dirac's quantization condition

Electromagnetic forces can be described in terms of scalar and vector potentials Φ and \vec{A} , instead of the electric and magnetic fields \vec{E} and \vec{B} . However, the definition of \vec{B} as the curl of a vector field, gives

$$\nabla \cdot \vec{B} = \nabla \cdot (\nabla \times \vec{A}) = 0 \quad (3.2)$$

which is precisely the absence of monopoles predicted in Maxwell's equations. Therefore, if the magnetic field is represented by the vector potential through Equation 3.2, then its field lines can never have start or end points. This appears to show that one cannot describe magnetic monopoles using the vector potential, which is particularly important in quantum mechanics theory, where particles are generally described in terms of their wave function ψ . When one describes an electrically charged particle in quantum mechanics, the complex phase ϕ of the wave function ψ depends on the vector potential \vec{A} . Moving in space causes the complex phase to change at a rate determined by the vector potential component parallel to the motion, which may be written

as

$$\nabla\phi = \frac{q\vec{A}}{\hbar c} \quad (3.3)$$

So, if the representation by a vector potential prohibits the existence of magnetic monopoles and quantum theory requires vector field representations, it seems that quantum theory requires the absence of magnetic monopoles. It was in 1931 that Paul Dirac showed a counterargument[1].

Assuming a very long coil with a flowing current, there will be a magnetic field that passes within the coil and expands at its extremities. The flux of the magnetic field inside the coils is given by the integral.

$$\Phi_B = \int \vec{B} \cdot d\vec{S} \quad (3.4)$$

If the length of the solenoid is much greater than its width, the shape of the magnetic field around the end of the solenoid looks exactly like that of a magnetic monopole with magnetic charge g , with $B = \frac{g}{r^2}\hat{r}$, so $\Phi_B = 4\pi g$. A vector field that is able to describe this magnetic field is

$$\vec{A} = g \frac{1 - \cos(\theta)}{r \sin(\theta)} \hat{\varphi} \quad (3.5)$$

\vec{A} is described in spherical coordinates, where θ is the angle with respect to the direction of the solenoid. One can see that the field contains a discontinuity at $\theta = 0$, the direction of the solenoid. This is known as the Dirac string. Figure 3.6 illustrates the situation.

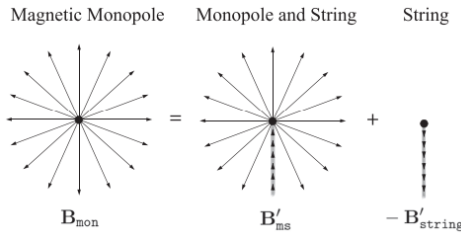


Figure 3.1: Representation of the magnetic field generated at the end of an infinite solenoid.

For this condition to really approach magnetic monopole behavior, it is necessary that the solenoid be undetectable. As the vector potential affects the wave function phase, as seen in equation 3.3, the solenoid generates a signal that can be detected. But there is a condition under which the solenoid can not be detected.

Assuming an electric charge traveling from point A to point B and passing through the vector field

produced by the solenoid, the phase divergence created by the vector potential is dependent on the path of the particle. That is, if one were to measure the phase shift from point A to point B, it would be possible to know the path the particle traveled, revealing the presence of the vector potential and the solenoid that produces it. Figure 3.2 represents the situation.

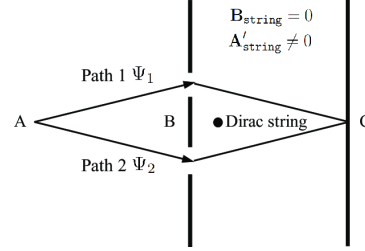


Figure 3.2: Aharonov-Bohm thought experiment, explaining the travel for a electric charge from A to B, passing through paths X and Y around the Dirac string.

Integrating equation (3.3) it is possible to quantify the phase shift θ_{X_n} caused by a given path X_n .

$$\theta_{X_n} = q \int_{A \rightarrow X_n \rightarrow B} \vec{A} \cdot d\vec{r} \quad (3.6)$$

A closed path going from A to B via X_n and returning to A via X_m would give a value determined by equation (3.7), which would be non-zero as long as $n \neq m$. The Stokes theorem can be applied, allowing for substitution of equation (3.4).

$$\Delta\theta = \theta_{X_n} - \theta_{X_m} = q \oint_C \vec{A} \cdot d\vec{r} \quad (3.7)$$

$$\Delta\theta = q \int \vec{B} \cdot d\vec{S} = q\Phi = \frac{q4\pi g}{\hbar c} \quad (3.8)$$

The complex wave function's phase θ makes its value indistinguishable from 2π addition. In this manner, X_m and X_n , two distinct pathways, would be indistinguishable if

$$\frac{4\pi qg}{\hbar c} = n2\pi ; \quad \frac{2qg}{\hbar c} \in \mathbb{Z} \quad (3.9)$$

It means that, in order for the magnetic monopole to be allowed, the electric charge must be quantized. In fact, any theory that assumes charge quantisation allows for the magnetic monopoles existence, as is the case of quantum mechanics. As a direct consequence of it, if the magnetic monopole exists, it would also come with a quantified magnetic charge of basic unit $g = \frac{\hbar c}{2e}$. This quantization is not exclusive for the Dirac string condition, and come naturally from the gauge symmetry, which will be shown ahead.

3.2.2 Gauge invariance

The Dirac string condition and the quantization of charge came from the hypothetical situation of the infinite solenoid. However, it is possible to show that the quantization condition is still present if you try to remove the Dirac string, as Cheng Yang developed in 1975 [2]. First, it is impossible to choose an \vec{A} such that it has no singularities around the sphere, which is a direct consequence of equation (3.2). Therefore, the only way to remove the string is to pick different \vec{A} for different regions around the monopole. Let's assume a vector potential for the superior side of the sphere surrounding the monopole and another potential for the inferior side of the sphere.

$$\begin{aligned}\vec{A}_{sup} &= g \frac{1 - \cos(\theta)}{r \sin(\theta)} \hat{\varphi} ; & 0 \leq \theta \leq \frac{\pi}{2} \\ \vec{A}_{inf} &= -g \frac{1 + \cos(\theta)}{r \sin(\theta)} \hat{\varphi} ; & \frac{\pi}{2} \leq \theta \leq \pi\end{aligned}\quad (3.10)$$

Defined this way, the vector potential contains no singularities and produces a magnetic field $\vec{B} = \frac{gr}{|r|^3}$ at any point in space, which means we successfully avoided the Dirac string while still constructing a magnetic monopole. As a boundary condition in this situation, it is necessary that at the intersection of the potentials at the equator, $\theta = \frac{\pi}{2}$, the vector fields describe the same physics. For this to be true, let us assume that the potentials obey the electrodynamic gauge symmetry.

$$\begin{aligned}\nabla\chi &= \vec{A}_{sup} - \vec{A}_{inf} \\ \nabla\chi &= \frac{2g}{r \sin(\theta)} \rightarrow \chi = 2g\varphi\end{aligned}\quad (3.11)$$

The same transformation χ must also be valid under the quantum mechanics gauge symmetry

$$\begin{aligned}\exp\left(\frac{ie\chi(\phi = 0)}{\hbar c}\right) &= \exp\left(\frac{ie\chi(\phi = 2\pi)}{\hbar c}\right) \\ \exp\left(\frac{ie2g(\phi = 0)}{\hbar c}\right) &= \exp\left(\frac{ie2g(\phi = 2\pi)}{\hbar c}\right)\end{aligned}\quad (3.12)$$

This leads to the same quantization condition in equation (3.9). In fact, the gauge symmetry present in electrodynamic and quantum mechanics theory expects the quantization of charge. In fact, gauge symmetry plays a central role in various fields of physics, so it is possible that other theories that have such symmetries would also expect the quantization of charge. Next, let's dive into more generalized gauge theories.

3.2.3 't Hooft-Polyakov monopole

By the 1970s, an effort was made by the physics community to develop a theory that would simultaneously describe electrodynamics, the weak force and the strong force, which would eventually become our current Standard Model of particle physics. These unifying theories would consider that, at high energies, the different forces can be described as one. Figure 3.3 shows the scales of energies involved. These unified theories have as a guiding principle the gauge symmetries present in electrodynamics. Although the gauge transformations involved are more complicated, the structure of these theories is very similar to Maxwell's theory.

The gauge symmetry present in Maxwell's theory is a U(1) symmetry, as the weak force theory holds a SU(2) symmetry. To describe a theory that would predict both, an electroweak force theory, it is reasonable to assume the symmetry of such a theory would be a combination of these, U(1) x SU(2), which was explored by Glashow, Weinberg, and Salam, granting them the Nobel Prize in 1979. At high

energies, the theories would be one and the same; at lower energies, something must be responsible for breaking the symmetry and splitting the two forces. This role was given to the Higgs field.

In the context of this work, the Higgs field can be understood as a continuous field that, in unified theories, is presented with three degrees of freedom, acting like a vector field. The length of the vector is the only thing that carries physical meaning, but once the length is set, the symmetries allow for smooth changes in the direction. The electroweak gauge symmetry theory was good enough to be able to predict the existence of novel particles, like the W and Z bosons, discovered in the 1980s, and the Higgs boson, which was granted the Nobel prize in physics in 2013. With such success, it later progressed to enclose the strong force description as a Grand Unified Theory (GUT), and here is where

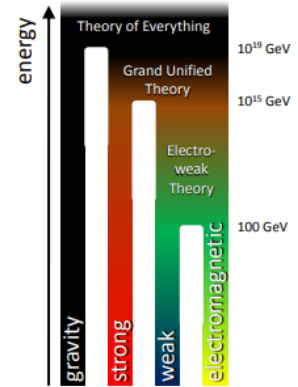


Figure 3.3: Representation of the energies at which the fundamental forces can be described by unified theories

the monopole comes into play.

As a distinct characteristic, the modulus of the Higgs field vector is non-zero at any point in a vacuum. In GUTs, the Higgs field usually varies smoothly across space, but it is possible to find it in a "hedgehog" configuration, where the vectors point in different directions from a point in space. This point cannot be removed by smooth transformations under the symmetry rules, making them topological defects in space. Figure 3.4 shows a representation of the Higgs field, which contains a defect at the origin.

As the Higgs field is always non-zero in the vacuum, this zero-valued topological defect could only be due to the presence of a particle. The particle, as theory predicts, would have two distinct characteristics: First, as the energy of this defect should be very high, the particle at this point would be massive. Second, it is possible to calculate the magnetic field generated by this defect, which turns out to be

$$\vec{B} = \frac{g\vec{r}}{|\vec{r}|^3}; \quad (3.13)$$

This is exactly the field generated by a quantified magnetic charge located at the origin. Therefore, the Grand Unified Theories not only allow for the magnetic monopole, they also expect it. This was first observed by Gerard 't Hooft and Alexander Polyakov in the 1970s [4]. The massive magnetic monopole predicted by GUTs would have energy of around 10^{15} GeV. The implications of such high energies will be better discussed in Section 4.3.2.

Once again, the gauge symmetry, now applied for more complex theories, allows for the existence of magnetic monopoles. If such particles really exist somewhere in the universe one may be able to find them, so let's start looking.

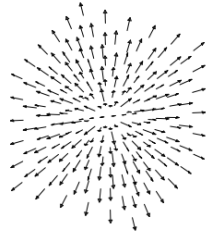


Figure 3.4: "Hedgehog" configuration of the Higgs fields, presenting a topological defect at the origin, where the field value is zero.

3.3 Looking for monopoles

3.3.1 Monopoles detection experiments

If the magnetic monopole is a particle predicted by GUTs, one may be able to detect it experimentally. In fact, unlike neutrinos, leptons, and other subatomic particles, it should be relatively easy to detect a magnetic monopole as it responds to electromagnetic interactions. Still, by the end of the 1980s, no one had ever encountered a sign of a magnetic monopole in our world. In 1982, Blas Cabrera prepared an experiment aiming to detect magnetic monopoles as astroparticles [5].

A particle with magnetic charge g , moving with a velocity v along the z -axis, passing through a coil of radius R and self-inductance L , would generate a current in such a coil. If the coil is made out of superconductive material and thus has zero resistance, the current would not dissipate. It is possible to calculate, integrating equation (3.1) along the area of the coil, the current induced by such a particle. Considering that the particle crosses the coil at $t = 0$ and applying the Stokes theorem

$$\begin{aligned} \int \vec{E} \cdot d\vec{l} &= \frac{1}{c} \int \frac{\partial \Phi_m}{\partial t} \cdot d\vec{A} + \frac{4\pi}{c} \int \vec{j}_m \cdot d\vec{A} \\ \Phi_B &= 2\pi g [1 - 2\Theta(t) + \frac{vt}{\sqrt{(vt)^2 + R^2}}] \\ \int \vec{j}_m \cdot d\vec{A} &= g\delta(t) \end{aligned} \quad (3.14)$$

The first term is equal to $L \frac{dI}{dt}$. The flux of a magnetic field is calculated considering a magnetic field in the form of equation 3.13, with $\Theta(t)$ being the Heaviside function. Integrating in time, knowing that the delta function $\Theta(t)$ is the time derivative of the Heaviside function $\Delta(t)$.

$$I(t) = \frac{2\pi g}{L} \left(1 + \frac{vt}{\sqrt{(vt)^2 + R^2}} \right) \quad (3.15)$$

The equation may not be intuitive, but it has a clear meaning. For $t \rightarrow -\infty$, long before any magnetic charge passes through the ring, $I = 0$. For $t \rightarrow \infty$, long after the monopole passes through the loop, $I = 4\pi g$. Interestingly, the value of the current generated does not depend on the radius of the loop and is clearly quantized. A passing monopole would return a distinguishable signal in quanta of $4\pi g$.

An detector was prepared at Stanford University using a four-turn, 5-cm-diameter loop coil made out

of superconducting material, put inside a protective shield, with its axis disposed vertically. From this configuration, the current expected to be generated by a passing monopole would be $I = 8\pi g$. The experiment was calibrated and set for 145 days, with the current in the coil being monitored constantly. On February 14, 1982, a large event was recorded, consisting of the current expected by the passage of a magnetic charge within 5% error.

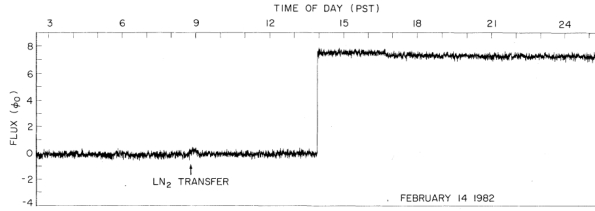


Figure 3.5: Current generated in a coil by a supposed magnetic monopole.

This result was shocking in the field of physics, and other scientists tried to replicate it, preparing their own detection experiment. The most notable of then was made by the Monopoles, Astrophysics, and Cosmic Rays Observatin (MACRO), based in Italy from 1989 to 2000, with an area of detection of 10000 m². The MACRO experiment was unable to find any monopoles as of the time it was active. In fact, not a single time after Cabrera was someone able to detect a signal that resembled a monopole astroparticle, which led to the discrepancy of the experiment. Scientists now begin to wonder: if there are monopoles roaming in the universe, what are the odds we come upon one?

3.3.2 Astrophysical bounds

If the monopoles are present in our universe, they would surely produce astrophysical effects, as Cabrera first tried to observe. Aside from that, any magnetic charge would be accelerated by a magnetic field, creating a magnetic current. Following the group of equations (3.1), the Lorentz force law over a magnetic charge moving with momentum p_m and interacting with fields \vec{E} and \vec{B} would take a different form. Also, let's remember the definition of the poynting vector (\vec{S}) and the fields energy density (u) in CGS units.

$$\frac{dp_m}{dt} = \int_V (\rho_m \vec{B} - \frac{\vec{j}_m}{c} \times \vec{E}) dV \quad (3.16)$$

$$\vec{S} = \frac{c}{4\pi} \vec{E} \times \vec{B}; u = \frac{E^2 + B^2}{8\pi}$$

From here, is easy to derive the poynting theorem, which takes the form.

$$\nabla \cdot \vec{S} + \frac{\partial u}{\partial t} = -\vec{j}_e \cdot \vec{E} - \vec{j}_m \cdot \vec{B} \quad (3.17)$$

The Poynting theorem shows clear that, just like electric current, magnetic current should also "drain" energy from the fields, which is expected as a consequence of conservation of energy. This way, if the flux of magnetic particles were too large, all the magnetic field would have dissipated in space. However, observations show that there is a magnetic field of roughly 3μG in our galaxy, from which we can conclude that the monopole flux cannot be very high around here. From this condition, Eugene Parker estimated in 1982 the maximum flux for GUTs monopoles to be $F \leq 10^{-15} \text{cm}^{-2} \text{s}^{-1} \text{sr}^{-1}$ [6]. The unit *sr*, or steradian, is the three-dimensional analog of the radian, with a value of 4πsr for a full sphere. The average number N of particles hitting a section of solid angle Ω of sphere of radius R per unit of time is given by

$$\frac{N}{t} = \Omega R F \quad (3.18)$$

For a detector the size of MACRO in the surface of the earth, that would be around $1.5 \cdot 10^{-18} \text{s}^{-1}$, around 1 monopole every 20 billion years. Astrophysical bounds related to the flux of magnetic monopoles are still very optimistic. The true limitations come into play when we consider the energy it takes to form a GUTs monopole in the first place.

As the mass of the GUT magnetic monopoles was expected to be very high ($E \approx 10^{15} \text{GeV}$), a very energetic event would be needed to form them. The only possible way a GUT monopole could have been formed would be shortly after the Big Bang, as it is the only event in the history of the universe to reach such high energies. However, if the monopoles were formed in the big bang, they would have recollapsed all the matter through their gravitational attraction. This is known as the "monopole problem", and Alan Guth proposes in the 1980s the cosmic inflation theory as possible solution.

The theory states that, just after the big bang, the universe started expanding exponentially, reaching apparent velocities much higher than the speed of light. This means that the density of monopoles in the current observable universe would be ridiculously low, so low that we probably will never be able to see one. If the monopoles cannot be found, we might as well try to make one ourselves.

3.4 Making monopoles

3.4.1 Particle accelerators

It was stated before that the monopoles predicted by the GUT were supposed to be massive, with energies around 10^{15}GeV . As the GUT is a high-energy theory, it predicts monopoles at such a level. However, the possibility remains that monopoles could exist with energies much lower than this, the so-called intermediate mass monopoles (IMM). If the energy of such monopoles were to be around 100GeV , in the order of the electroweak theory energies, it would be possible to produce them in particle accelerators.

The Large Hadron Collider (LHC), the world's largest particle accelerator, is able to reach collision energies of 13TeV . It currently holds 7 experiments, one of which is the Monopole and Exotics Detector at the LHC (MoEDAL)[7]. This system consists of a series of plate detectors disposed around the collision point. The plate detectors are designed to detect the track of ionizing particles and trap them.

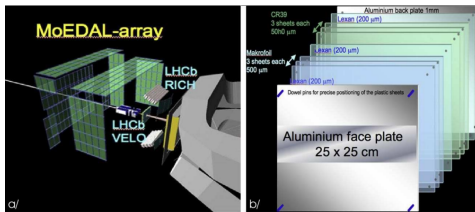


Figure 3.6: At left, MoEDAL detection architecture, consisting of a series of detection plates surrounding the area of collision. At right, depiction of the detection plate, consisting of aluminum and polymer sheets

When a pair of protons collide with such high energies, fundamental particles can be created by the Schwinger effect. The special thing about IMM's is that they would be very stable compared to other elementary particles produced while also been highly ionizing. MoEDAL's detection mechanism consists of a stack of polymer sheets that would be penetrated by IMM's, leaving a ionizing track that can be exposed chemically. Aluminum sheets are put at the start and end of the track to act as traps, as the monopoles are expected to bind strongly to this material. The sheets are analyzed by superconducting coils, allowing for the detection and quantization of the longing current that would be generated by the passing monopoles. The MoEDAL experiment is functioning since 2011 but has not yet been able to find magnetic charges. The search goes on.

3.5 Conclusion

In 1931, based on quantum mechanics and electrodynamics theory, Dirac predicted the existence of a never seen particle: the magnetic monopole. This is the same physics who would win the Nobel prize of 1933, for the prediction of the antimatter. It has been 92 years and the search is far from over.

The search for magnetic monopoles walked side by side with the development of the 20th century physics. They emerged from quantum mechanics and electrodynamics, walked their way through topology, gauge field theories and the Grand Unified Theories. The search for them went from astrophysical observations to cosmological predictions. We have no idea if such particles do exist, but we are certain that, even if they do, we may never come upon them. Current research explores the possibility of the formation of intermediate mass monopoles, through particles accelerator experiments, the main one being MoEDAL. In the next decades, as the physics theory develops itself, we hope to see the monopole problem being solved.

Bibliografia

- [1] Dirac, P. A. M. (1931). Quantised Singularities in the Electromagnetic Field. *Proceedings of the Royal Society A: Mathematical, Physical and Engineering Sciences*, 133(821), 60–72.
- [2] Wu, T. T., Yang, C. N. (1975). Concept of nonintegrable phase factors and global formulation of gauge fields. *Physical Review D*, 12(12), 3845–3857.
- [3] Cabrera, B. (1982). First Results from a Superconductive Detector for Moving Magnetic Monopoles. *Physical Review Letters*, 48(20), 1378–1381.
- [4] Hooft, G. ' (1974). Magnetic monopoles in unified gauge theories. *Nuclear Physics B*, 79(2), 276–284. doi:10.1016/0550-3213(74)90486-6
- [5] Cabrera, B. (1982). First Results from a Superconductive Detector for Moving Magnetic Monopoles. *Physical Review Letters*, 48(20), 1378–1381.
- [6] Turner, M. S., Parker, E. N., Bogdan, T. J. (1982). Magnetic monopoles and the survival of galactic magnetic fields. *Physical Review D*, 26(6), 1296–1305.
- [7] Acharya, B., et al . . . Chatterjee, A. (2016). Search for magnetic monopoles with the MoEDAL prototype trapping detector in 8 TeV proton-proton collisions at the LHC. *Journal of High Energy Physics*, 2016(8).

4

The Thomas precession

Jaime J.B. Marquez

Instituto de Física de São Carlos, Universidade de São Paulo, 13560-970 São Carlos, SP, Brazil

Abstract: Abstract.

4.1 Introduction

Bibliografia

[1]

5

Superconductivity and the Meissner effect

Julia Marcolan Teixeira

Instituto de Física de São Carlos, Universidade de São Paulo, 13560-970 São Carlos, SP, Brazil

Abstract: The effects of superconductivity were observed by Heike Kamerlingh Onnes in 1911 when he cooled mercury to a temperature below 4.2 K using liquid helium. Superconductors exhibit zero electrical resistance below a critical temperature, and the Meissner effect ensures that the magnetic field is expelled from their interior. This effect was phenomenologically introduced into Maxwell's equations by the London brothers, but its physical origin was only explained in 1957 by physicists John Bardeen, Leon Cooper, and Robert Schrieffer through the BCS theory. Superconductors have important applications such as Magnetic Levitation Transport (Maglev) and in magnetic resonance imaging (MRI).

5.1 Introduction

One of the main issues in the early 1900s was the question of what happens to the resistivity of a metal as its temperature approaches absolute zero. In 1908, Kamerlingh Onnes successfully liquefied helium at 4.2 K, marking the beginning of a new chapter in physics. In 1911, Heike Kamerlingh Onnes successfully refrigerated mercury to critical temperatures below 4.2 K, estimating the resistance to be 10^{-55} Ohm (practically zero, considering experimental error). This value is 10^{-12} times the resistance of mercury under normal conditions [1].

Heike Kamerlingh Onnes provided an initial definition of a superconductor as one in which electrical resistance tends to zero when cooled below a critical temperature (T_c). Because of this discovery, Kamerlingh Onnes won the Nobel Prize in 1913. Figure 5.1 illustrates the experimental setup used in the experiment, consisting of a cryostat where liquid helium, among other cryogenic fluids, is introduced

and a plot of resistance (ohms) versus temperature (K) for mercury from the first experiment to detect superconductivity.

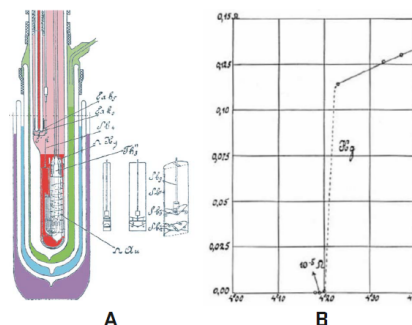


Figure 5.1: A: The bottom of the cryostat, where Heike Kamerlingh Onnes and his coworkers conducted the experiment that initially revealed superconductivity. The colors represent different cryogenic fluids within the intricate dewar [1]. B: A plot of resistance (ohms) versus temperature (K) for mercury from the 1911 experiment shows the superconducting transition at 4.20 K [1].

More robust theories were developed to explain the phenomenon and complemented the initial definition, and various other superconductor materials, in addition to mercury, were also discovered such as the niobium–titanium alloy. Applications involving superconductors face the challenge of requiring extremely low temperatures to achieve the superconducting state. Nevertheless, there are numerous applications utilizing superconducting materials, including Nuclear Magnetic Resonance Imaging (MRI) used as a diagnostic method and Magnetic Levitation Transport (Maglev).

5.2 Superconductor features and Meissner effect

Once a continuous electric current is established in a superconductor, it remains without the use of any energy source, as long as the temperature remains below the critical temperature. Given that the superconductor has no measurable electrical resistance, it operates like an ideal conductor with infinite conductivity or zero resistivity, and superconductors do not lose energy in the form of heat through the Joule effect. Nevertheless, this condition can change with the increase in temperature above T_c , where the material leaves the superconducting state.

Walther Meissner and Robert Ochsenfeld discovered another crucial characteristic in 1933. When a magnetic field is applied to a superconducting material at a temperature T above its critical temperature, the magnetic field penetrates the material, resulting in an internal magnetic field. As the temperature is lowered below the critical temperature, it enters the superconducting state. In this state, the material behaves like a perfect diamagnet, expelling the magnetic field. This phenomenon is recognized as the Meissner Effect and serves as a distinctive feature that sets superconductors apart from perfect conductors. Figure 5.2 illustrates the behavior of the superconductor when subjected to a magnetic field in two situations: above T_c and below T_c .

For any given temperature, there exists a critical magnetic field H_c that can be applied without compromising the material's superconducting properties. There are two types of superconductor materials. Type I superconductors are predominantly composed of metals and metallic alloys, with critical temperatures reaching extremely low values on the order of 10 K. Furthermore, the material undergoes a transition to the normal state when the magnetic field reaches a critical value, H_c .

Figure 5.3A shows

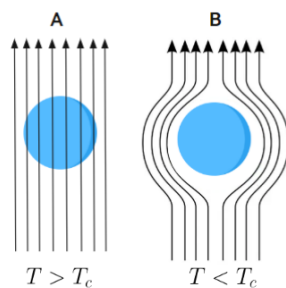


Figure 5.2: A: The magnetic field lines penetrate the superconducting material when it is above the critical temperature. B: When the temperature drops below the critical temperature, the field lines are then expelled from the superconductor. Figure produced by the author.

the behavior of the type I superconductor considering the magnetic field H as a function of temperature, and Figure 5.3B shows the relationship between the magnetic field H and temperature for different type I superconductors.

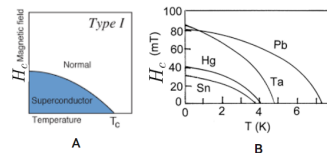


Figure 5.3: A - Behavior of the type I superconductor considering the magnetic field (H) as a function of temperature. Below the critical magnetic field, the material remains in the superconducting state, while above it transitions to a normal state. B - Relationship between the magnetic field (H) and temperature for different type I superconductors.

Type II superconductors are composed of metallic alloys and other materials, such as ceramics. Their critical temperatures are higher, but still fall within the range of low temperatures on the order of 100 K. Type II superconductors are characterized by exhibiting two critical magnetic fields: the first is H_{c1} , and the second is H_{c2} . Below the critical field H_{c1} , they behave like a type I superconductor, while above the critical field H_{c2} , they behave like a normal material without superconductivity. Between H_{c1} and H_{c2} , there is a partial penetration of magnetic flux, forming superconducting regions and regions in the normal state that allow magnetic field penetration. This behavior of type II superconductors is not yet fully explained by existing theories. Figure 5.4A shows the behavior of type II superconductors considering the magnetic field H as a function of temperature, and Figure 5.4B shows the vortex state with normal cores surrounded by superconducting regions.

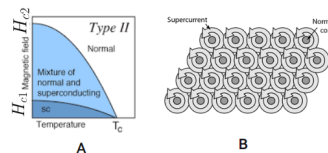


Figure 5.4: A - Behavior of the type II superconductor considering the magnetic field H as a function of temperature. Below the first critical magnetic field, H_{c1} , the material remains in the superconducting state; above the second critical magnetic field, H_{c2} , it transitions to a normal state. Between the fields H_{c1} and H_{c2} , there exists a mixture of states. B - Vortex with normal cores surrounded by superconducting regions observed in type II superconductors.

If any diamagnetic material, other than a superconductor, is in a region where there is a constant

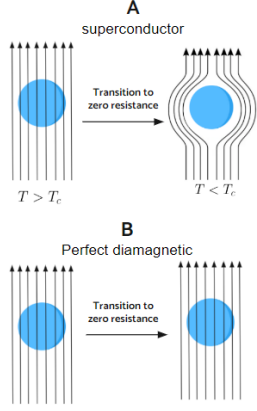


Figure 5.5: A: A magnetic field penetrates a superconductor at a temperature T above the critical temperature. The superconductor is then brought into the zero-resistance state when the temperature is lowered below T_c , and the magnetic field is expelled from the interior of the superconductor. B: A magnetic field penetrates a perfect diamagnet in a situation where the electrical resistance is not zero. After some mechanism is used to lower the electrical resistance, the magnetic field is not expelled and continues within the material. Figure produced by the author.

magnetic field, and it is somehow possible to reduce its electrical resistance to zero without changing the magnetic field, the field will remain inside the material. This happens because, according to Faraday's law, a variable magnetic field is necessary to induce the currents used to cancel the magnetic field inside the sample. The existence of the Meissner effect implies that it is possible to induce currents in a superconductor even if the applied magnetic field is constant; for this, it is sufficient to reduce the temperature to a value lower than the critical temperature and consequently reduce the resistance to zero. In a superconductor, it doesn't matter the order in which the magnetic field is applied before or after the temperature and resistance reduction. Figure 5.4 depicts a comparison between what happens with an ideal diamagnetic and a superconductor when brought to a condition in which resistance is reduced to zero [2]. For this reason, although the expulsion of the internal magnetic field is related to diamagnetism, it cannot serve as an explanation for the Meissner effect. This phenomenon is not addressed by Faraday's law, and a new theory should be developed to explain it.

5.3 London equations

In 1935, brothers Fritz and Heinz London developed a phenomenological explanation capable of

elucidating the Meissner effect based on observations of the superconductors behavior. They incorporated specific conditions for superconductors into a description based on Maxwell's equations.

When normal conduction electrons move, they are subject to the resistance of the material, and their motion can be described by equation (5.1).

$$m \frac{d\vec{v}}{dt} = e\vec{\varepsilon} - \frac{\vec{v}}{\Gamma} \quad (5.1)$$

Where Γ is the resistance. If the electron in question moves without any resistance, then the motion can be described by equation (5.2)

$$m \frac{d\vec{v}}{dt} = e\vec{\varepsilon} \quad (5.2)$$

We can write the current density as 5.3.

$$\vec{j} = en_s \vec{v} \quad (5.3)$$

Substituting (5.3) into the equation of motion (5.2), we then find (5.4) which is the first London equation.

$$\frac{\partial \vec{J}}{\partial t} = \frac{n_s e^2}{m} \vec{\varepsilon} \quad (5.4)$$

Equation (5.4), results in the electrical field (5.5)

$$\vec{\varepsilon} = \frac{m}{e^2 n_s} \frac{d\vec{J}}{dt} \quad (5.5)$$

Substituting equation (5.5) into Faraday's law ($\nabla \times \vec{\varepsilon} = -\frac{\partial \vec{B}}{\partial t}$), we find the relationship described in (5.6)

$$\frac{\partial}{\partial t} \left(\nabla \times \vec{J} + \frac{e^2 n_s}{m} \vec{B} \right) = 0 \quad (5.6)$$

From the equation, we see that the term in parentheses needs to be constant, and we will assume that this constant is zero we found (5.7) which is the second London equation

$$\nabla \times \vec{J} = -\frac{e^2 n_s}{m} \vec{B} \quad (5.7)$$

Using Ampère's law ($\nabla \times \vec{B} = \mu_0 \vec{J}$), after applying some identities, we find equation 5.8

$$\nabla^2 \vec{B} = \frac{1}{\lambda_L^2} \vec{B} \quad (5.8)$$

The solution to the differential equation (5.8) indicates that the magnetic field \vec{B} must be exponentially attenuated within the superconductor, such that it is appreciable only up to a distance λ_L from

the surface of the superconductor. Where λ_L represents the London penetration depth, and its value is given by $\lambda_L = \sqrt{\frac{m}{\mu_0 e^2 n_s}}$. Analyzing the values of λ_L components, it is possible to estimate its value to be between 100 and 1000 Angstrom.

Furthermore, applying the curl operator to (5.7) and applying some identities, we arrive at equation (5.9)

$$\nabla^2 \vec{J} = \frac{1}{\lambda_L^2} \vec{J} \quad (5.9)$$

Just like for the magnetic field inside the superconductor, equation (5.9) indicates that the superconducting current should be situated near the surface, penetrating only the distance allowed by the London penetration depth. Thus, we can conclude that the superconducting current density is indeed volumetric, but, similar to the magnetic field, it exponentially decays within the sample, being appreciable only in a very small volume within the superconductor.

To conclude that the term in parentheses from equation (5.6) was equal to zero, the London Brothers supposed that a part of electrons in the system move without losses (superconductor electrons), while another part comprises normal electrons [5]. This assumption is similar to the two-fluid model of liquid helium by Gorter and Casimir [4]. Under these conditions, the free energy of the system is given by equation (5.10).

$$F = F_n + F_s + F_{mag} \quad (5.10)$$

where F_n is the free energy of normal electrons, F_s is the contribution of superfluid electrons, and F_{mag} is the energy of the magnetic field. Using Ampère's equation for the magnetic field, it is possible to express the free energy solely in terms of integrals of the magnetic field 5.11, and the energy of normal electrons doesn't depend on this field.

$$F = F_n + \frac{1}{8\pi} \int \left[\vec{B}^2 + \frac{m}{n_s e^2} (\nabla \times \vec{B})^2 \right] dr \quad (5.11)$$

When we minimize the free energy with respect to the magnetic field, we obtain exactly the expression (5.8). The London theory establishes a connection between superfluid electrons moving without losses and the Meissner effect. The two-fluid model is composed of bosons, they are particles with integer spin which impose no restrictions on the occupation of energy levels, allowing us to place as many bosons as we want in each quantum energy level. According to

the two-fluid model, at low temperatures, a macroscopic number of bosons tends to occupy the lowest energy level, forming a condensate where there is no thermal agitation, while the others occupy other energy states, behaving like a normal fluid. However, electrons are fermions that have half-integer spin and obey Pauli's Exclusion Principle. Only one fermion can be allocated to each quantum energy level. Thus, how can the behavior of electrons be compared to the two-fluid model?

The ideas introduced by the London brothers explained phenomenologically the existence of the Meissner effect but still failed to provide a physical mechanism capable of explaining why superconductivity was possible.

5.4 BCS theory

In 1957, physicists John Bardeen, Leon Cooper, and Robert Schrieffer introduced a theoretical model that agreed with experimental observations in superconductors. This model became known as the BCS Theory, named after the initials of the authors, and earned them the Nobel Prize in Physics in 1972. In this work, the BCS theory will be addressed in a more qualitative manner. A detailed theoretical description based on quantum field theory can be found in reference [7].

The BCS theory is based on the formation of Cooper pairs, proposed by Leon Cooper in 1956, suggesting a bound state between two electrons. Electrons naturally repel each other due to Coulombic repulsion, as they have charges of the same sign. Cooper's theory proposed that electrons can attract each other through the ions in the crystalline structure inside a metal.

Cooper pairs are formed at low temperatures, where the ions thermal agitation are lower. To understand this process, let's consider that it is actually formed by two steps. In the first step, consider an electron in the material moving in a region with positive ions. There is an attractive interaction between them that creates a deformation propagating through the lattice, which can be associated with the emission of a phonon. This deformation increases the concentration of positive charges in a particular region; it can happen that a second electron passes near this region and is attracted by the phonon emitted by the first. Figure 5.6 shows a schematic illustrating the interaction, which can be considered as an attractive interaction between the electrons since both intermediate interactions were positive. The two electrons then form a bound state

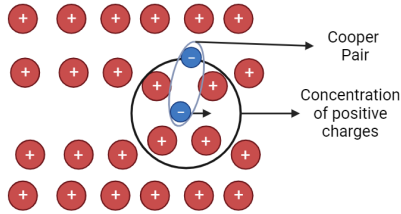


Figure 5.6: An electron moving in a region of positive ions interacts, creating a deformation that propagates through the lattice and can be associated with the emission of a phonon. This increases the concentration of positive charges in a specific region, and a second electron can be attracted by the phonon emitted by the first. The figure illustrates the propagation of the electron, the concentration of positive charges in a specific region, and the formation of the Cooper pair.

called a Cooper pair.

Cooper pairs behave like bosons, as the sum of electron spins results in an integer value. Thus, more than one Cooper pair can occupy the same energy state. Cooper pairs have lower energy than fermions, and at low temperatures, they occupy the lowest energy state, forming a Cooper pair condensate. This theory aligns with the idea proposed by the London brothers to explain superconductivity through the two-fluid model.

However, the presence of direct Coulomb repulsion diminishes the effectiveness of the attraction between electrons, rendering it relatively weak. The energy distribution in a superconductor has a forbidden energy range around the Fermi energy, given by E_g , similar to superconductors that have an energy gap between the conduction and valence bands. The value of E_g at a given temperature is equal to the Cooper pair binding energy for that temperature.

Figure 5.7 shows the experimental results for energy gap values E_g as a function of temperature T for some superconducting elements, while the continuous curve depicts the same behavior predicted by the BCS theory. For temperatures on the order of the critical temperatures of superconductors, the value of E_g is much larger than the thermal energy available to the atoms. Thus, Cooper pairs persist despite the weak binding.

The structure formed by Cooper pairs is extremely ordered, so that when they move, this ordering is maintained, and the superconductor remains free from interactions responsible for the appearance of electrical resistance. This ordered motion also suggests that the electrons participating in the supercurrent are good charge conductors but do not conduct heat, as heat is generated by the disordered motion of electrons.

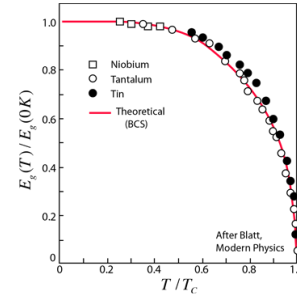


Figure 5.7: energy gap values E_g as a function of temperature T for some superconducting elements,

5.5 Applications of superconductivity

Applications involving superconductors face the challenge of requiring extremely low temperatures to achieve the superconducting state. Nevertheless, there are numerous applications utilizing superconducting materials. In this section, two of them will be commented on.

5.5.1 Magnetic Resonance Imaging (MRI)

Magnetic Resonance Imaging is one of the applications of Nuclear Magnetic Resonance and is used in various fields, including industry, agriculture, material science, and, most notably, in medicine as an important diagnostic method. Magnetic resonance techniques use a static and homogeneous magnet combined with a series of radiofrequency pulses to excite the samples and process the signals. In the case of imaging, the signals are spatially encoded by the use of linear gradient fields. Figure 5.8A shows a magnetic resonance image of a brain and Figure 5.8B shows magnetic resonance imaging equipment.

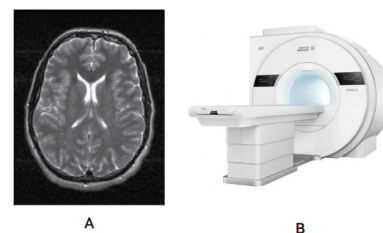


Figure 5.8: Magnetic resonance image of a brain [3]. B: Magnetic resonance imaging equipment.

An ultrastable magnetic field is employed to provide high-resolution images without artifacts. The magnetic field is generated by a constant current in

a coil made of superconducting material wire that forms the magnet. The wire must be immersed in a bath of liquid helium to keep it in a superconducting state. To reduce the boil-off of liquid helium, it is enclosed in a vacuum jacket filled with materials that limit radiative losses. This setup is surrounded by an additional jacket filled with liquid nitrogen and another vacuum jacket to isolate it as much as possible from the room-temperature environment as we can see in the Figure 5.9. The central bore of the magnet, which houses the sample probe, is at room temperature.

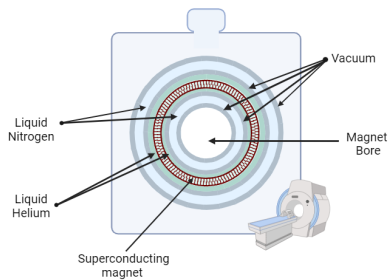


Figure 5.9: Cooling scheme of a superconducting magnet used in Magnetic Resonance Imaging equipment. The liquid helium is enclosed in a vacuum jacket filled with materials that limit radiative losses. This setup is surrounded by an additional jacket filled with liquid nitrogen and another vacuum jacket to isolate it as much as possible from the room-temperature environment. Figure produced by the author.

5.5.2 Magnetic Levitation Transport (Maglev)

A manifestation of the Meissner effect is magnetic levitation. When a magnet is placed near a superconductor in its superconducting state, the magnetic fields generated by the magnet are expelled from the interior of the superconductor. This results in a magnetic repulsion, causing the magnet to levitate above the superconductor. This magnetic interaction creates a repulsive force that balances the weight of the magnet, allowing it to levitate over the superconductor.

Magnetic levitation is an interesting phenomenon and has practical applications in technologies such as magnetic levitation trains (Maglev). A magnetic levitation train, or Maglev (Magnetic Levitation Transport), is similar to a train that travels on an elevated track above the ground through the use of superconductors. Due to its high production cost, there is currently only one commercial line, the Shanghai Transrapid 5.10. This line covers a distance of 30 km to Pudong International Airport in just 8 minutes and can be seen in the figure. Con-

struction began in March 2001, and it commenced operations on January 1, 2004.



Figure 5.10: Transrapid de Xangai.

5.6 Conclusion

After observations of the effects of superconductors, it was necessary for some theories to be developed before physicists John Bardeen, Leon Cooper, and Robert Schrieffer formulated the BCS theory capable of explaining the underlying physical principles of superconductivity. They were awarded the Nobel Prize in Physics in 1972 for this theory, which has numerous applications. However, the BCS theory can only perfectly explain the behavior of type I superconductors; it does not encompass type II superconductors.

Bibliografia

- [1] Dirk Van Delft and Peter Kes. The discovery of superconductivity. *Physics Today*, 63(9):38–43,2010.
- [2] Machado, Kleber Daum, *Teoria do Eletromagnetismo Volume II*, Ed. UEPG, Ponta Grossa, 2002.
- [3] JENKINSON, Mark; CHAPPELL, Michael. *Introduction to neuroimaging analysis*. Oxford University Press, 2018.
- [4] Poole, C. P., Farach, H. A., Creswick, R. J., & Prozorov, R. (2014). *Superconductivity*. Elsevier.
- [5] Fritz London and Heinz London. The electro magnetic equations of the supraconductor. *Proceedings of the Royal Society of London. Series A Mathematical and Physical Sciences*,149(866):71–88, 1935.
- [6] John Bardeen, Leon N Cooper, and John Robert Schrieffer. Theory of superconductivity. *Physical review*, 108(5):1175, 1957.
- [7] LANCASTER, Tom; BLUNDELL, Stephen J. *Quantum field theory for the gifted amateur*. OUP Oxford, 2014.

6

Radiation reaction

Lucas Gois Tavares

Instituto de Física de São Carlos, Universidade de São Paulo, 13560-970 São Carlos, SP, Brazil

Abstract: In this work, we provide a brief introduction to the fundamental concepts of electrodynamics classical, in order to investigate and analyze in a comprehensive way the effects resulting from the reaction radiation. Initially, we use solutions of the Maxwell's equations to describe the fields generated by point loads, resulting in the Lienard-Wiechert fields. A next, we go deeper into the description of the radiation emitted by punctual loads at low speeds, covering the non-relativistic context. In this context, we derived the Larmor formula, which quantifies the radiation power. Using the theoretical tools developed in the previous sections, we expand our analysis for simple oscillating systems, determining the Abraham-Lorentz force exerted on the source loads.

6.1 Introduction

Classical electrodynamics is a fundamental branch of physics that describes electromagnetic interactions among charged particles and the electric and magnetic fields surrounding them. Since the pioneering works of Michael Faraday and James Clerk Maxwell in the 19th century, electromagnetic theory has played a central role in understanding natural phenomena. Over the years, advancements in classical electrodynamics have led to the formulation of Maxwell's laws, which unified electricity and magnetism into a consistent set of differential equations. These laws laid the groundwork for understanding electromagnetic waves and made it possible to explain the propagation of light and other forms of electromagnetic radiation.

In this work, we present an exploration of the fundamental concepts of classical electrodynamics with a special emphasis on the effects of radiation reaction. Initially, we introduce the basic principles of electromagnetic theory, including the formulation of

Maxwell's laws and the application of gauge transformations to the electromagnetic field. Next, we address the fields generated by point charges, using the solution of the wave equation in electromagnetic potentials, known as Lienard-Wiechert fields. We explore how these fields behave and interact with charged particles.

An issue of interest is the emission of radiation by moving point charges. We investigate the non-relativistic case, where particle velocities are low compared to the speed of light, allowing for the derivation of the Larmor formula for emitted radiation power. Additionally, we analyze the effects of radiation reaction on the particles themselves, leading to the formulation of the Abraham-Lorentz force.

Subsequently, we broaden our discussion to encompass a more realistic context by introducing the electron model from Lorentz's theory. We rederive the Abraham-Lorentz force, now free from acceleration divergence terms. We deduce the covariant version of Maxwell's equations and the Larmor formula, subsequently analyzing the relativistic effects on the radiation reaction emitted by charged particles in accelerated motion. We compare the results obtained with those from classical electrodynamics (non-relativistic context).

6.2 Dynamics of electrical charges

The Maxwell's equations in the International System of Units (SI) are:

$$\nabla \cdot \mathbf{E} = \frac{\rho}{\varepsilon_0}, \quad (6.1)$$

$$\nabla \cdot \mathbf{B} = 0, \quad (6.2)$$

$$\nabla \times \mathbf{E} = -\frac{\partial \mathbf{B}}{\partial t}, \quad (6.3)$$

$$\nabla \times \mathbf{B} = \mu_0 \mathbf{J} + \mu_0 \varepsilon_0 \frac{\partial \mathbf{E}}{\partial t}. \quad (6.4)$$

which, together with the strength of Lorentz,

$$\vec{F} = q \left(\vec{E} + \vec{v} \times \vec{B} \right) \quad (6.5)$$

They fully describe the dynamics of the electromagnetic field and its interaction with particles. However, solving this set of equations is not a trivial process, because at least we need to know the densities of charge ρ and current \vec{J} .

6.2.1 The Liénard–Wiechert potentials

The scalar and vector potentials are a way of describing the electromagnetic field generated by charge densities and arbitrary currents. However, in order to describe the effects of radiation, fields generated by point charges, the so-called potentials and fields of radiation will be studied. Liénard–Wiechert. The Liénard–Wiechert potentials describe, in a relativistically correct manner, the classical effects of the electromagnetic field generated by charges in arbitrary motion. Starting from the Lorenz Gauge, the Potential retarded calls are given by:

$$\phi(\vec{r}, t) = \frac{1}{4\pi\varepsilon_0} \int d^3r' \int dt' \frac{(\rho_q(t), t')}{|\vec{r} - \vec{r}_q(t)|} \delta\left(t' - \left[t - \frac{|\vec{r} - \vec{r}_q(t')|}{c}\right]\right) \quad (6.6)$$

$$\vec{A}(\vec{r}, t) = \frac{1}{4\pi\varepsilon_0} \int d^3r' \int dt' \frac{(\vec{J}_q(t), t')}{|\vec{r} - \vec{r}_q(t)|} \delta\left(t' - \left[t - \frac{|\vec{r} - \vec{r}_q(t')|}{c}\right]\right) \quad (6.7)$$

It is worth noting that both potentials, which are evaluated at time t , are given in terms of the integral

of the sources evaluated at the delay time, $t_R = t - |\vec{r} - \vec{r}_q(t')|/c$ which in turn is the time before t . For a point particle, the densities of charges and current can be related to the charge q by middle of the Dirac delta distribution,

$$\rho(\vec{r}_q(t), t') = q\delta^3(\vec{r} - \vec{r}_q(t')) \quad (6.8)$$

$$\vec{J}(\vec{r}_q, t') = q\vec{v}(t')\delta^3(\vec{r}_q(t) - \vec{r}_q(t')) \quad (6.9)$$

which, when substituted in EQs 3 and 4, result in the Liénard–Wiechert potentials :

$$\phi(\vec{r}, t) = \frac{q}{4\pi\varepsilon_0} \frac{1}{\left|\vec{R}(t_R) - \vec{\beta}(t_R) \cdot \vec{R}(t_R)\right|} \quad (6.10)$$

$$\vec{A}(\vec{r}, t) = \frac{\mu_0}{4\pi} \frac{q\vec{v}(t_R)}{\left|\vec{R}(t_R) - \vec{\beta}(t_R) \cdot \vec{R}(t_R)\right|} \quad (6.11)$$

where $\vec{\beta} = \frac{\vec{v}}{c}$.

From the potentials, it is possible to find the respective electric and magnetic fields. It is worth remembering that

$$\vec{E}(\vec{r}, t) = \frac{q}{4\pi\varepsilon_0} \left\{ \frac{(\vec{R}(t_R) - |\vec{R}(t_R)|\vec{\beta}(t_R))(1 - |\vec{\beta}(t_R)|^2)}{[|\vec{R}_{t_R}| - \vec{R}(t_R) \cdot \vec{\beta}(t_R)]^3} + \frac{\vec{R}(t_R) \times (\vec{R}(t_R) - |\vec{R}(t_R)|\vec{\beta}(t_R)) \times \frac{\vec{\alpha}(t_R)}{c}}{[|\vec{R}_{t_R}| - \vec{R}(t_R) \cdot \vec{\beta}(t_R)]^3} \right\} \quad (6.12)$$

$$\vec{B}(\vec{r}, t) = \frac{1}{c} \left[\hat{R}(t_R) \times \vec{E}(\vec{r}, t) \right] \quad (6.13)$$

The electric field described by Eq.(7.12) has two contributions, the first term depends only on the velocity $\vec{\beta}(t_R)$ of the particle, while the second also exhibits dependence on the acceleration of the particle, $\vec{\alpha}(t_R)$. For this reason, the factor that is proportional to $\vec{\beta}(t_R)$, is known as the electric field of velocity or Coulomb field, and the second term, proportional to $\vec{\alpha}(t_R)$, is known as the electric field of radiation. Similarly, the magnetic field also has such characteristics. Finally, it is important to note that the Liénard–Wiechert fields are linked to each other, as can be seen in Eq.(7.13).

6.3 Radiation of an accelerated charge

When it comes to electromagnetic radiation, it can be generated by various types of charge and cur-

rent distribution. distribution of charges and currents, however, we will only be interested in the radiation emitted by the simplest form of distribution, i.e. by point charges. As we discussed earlier, the fields generated by point charges are the so-called Liénard-Wiechert fields.

As we are interested in the radiation emitted at points very far from the source, the velocity dependent term, proportional to $1/R^2$, cancels out faster than the acceleration fields, proportional to $1/R$, when $R \rightarrow \infty$. In this limit, the electric field will be expressed by:

$$\vec{E}(\vec{r}, t) \approx \vec{E}_a(\vec{r}, t) = \frac{q}{4\pi\epsilon_0} \frac{\vec{R}(t_R) \times (\vec{R}(t_R) - |\vec{R}(t_R)|\vec{\beta}(t_R)) \times \frac{\vec{a}(t_R)}{c}}{[|\vec{R}_{t_R}| - \vec{R}(t_R) \cdot \vec{\beta}(t_R)]^3} \quad (6.14)$$

Remembering that the flow of energy (per unit area) carried by the electromagnetic wave is given by the Poynting vector,

$$\vec{S} = \frac{1}{\mu_0} \vec{E} \times \vec{B} = \frac{1}{\mu_0} \vec{E} \times \left[\frac{\hat{R} \times \vec{E}(\vec{r}, t)}{c} \right] \quad (6.15)$$

where, using the bla bla vector identity $\vec{a} \times (\vec{b} \times \vec{c}) = (\vec{b} \cdot \vec{c})\vec{a} - (\vec{a} \cdot \vec{c})\vec{b}$, we rewrite Eq.(7.15):

$$\vec{S} = \frac{1}{\mu_0 c} \left\{ |\vec{E}|^2 \hat{R} - (\hat{R} \cdot \vec{E}) \vec{E} \right\} \quad (6.16)$$

To determine the power emitted (P) by the charge in motion, we need to integrate the Poynting vector over a surface σ . In this case, the most appropriate surface is a spherical shell centered at the position of the charge (evaluated at the retardation time), i.e., a sphere with a radius $R = c(t - t_R)$. In general, the electric field can have contributions from both the velocity and acceleration fields. However, by analyzing Eq.(7.16), we will see that the Poynting vector has terms proportional to $\frac{1}{R^4}$ (velocity field multiplied by itself), $\frac{1}{R^3}$ (velocity field multiplied by the acceleration field), and $\frac{1}{R^2}$ (acceleration field multiplied by itself). However, the area of the sphere to be considered is proportional to the square of the radius, i.e., $A \propto R^2$, so in the limit as $R \rightarrow \infty$, the only term that will have a significant contribution is the term generated by the acceleration field ($\propto \frac{1}{R^2}$).

As the accelerating electric field is perpendicular to the versor \hat{R} , Eq.(7.16) reduces to:

$$\vec{S} = \frac{1}{\mu_0 c} |\vec{E}_a|^2 \hat{R} \quad (6.17)$$

Consequently, the power passing through the sphere at time t will be:

$$\frac{dP(t)}{dA} = \vec{S} \cdot \hat{R} \quad (6.18)$$

If we consider that the unit area can be given by $dA = R^2 d\Omega$, the radiated power assumes:

$$\frac{dP(t)}{d\Omega} = R^2 [\vec{S} \cdot \hat{R}] = \frac{R^2}{\mu_0 c} |\vec{E}_a|^2 \quad (6.19)$$

We can see that the power is not the same as that emitted at t_R , which can be obtained using the chain rule:

$$P(t_R) = \frac{dW}{dt_R} = \frac{dW}{dt} \frac{\partial t}{\partial t_R} \rightarrow P(t_R) = P(t) \frac{\partial t}{\partial t_R} \quad (6.20)$$

in such a way that we will have

$$P(t) = \frac{P(t_R)}{1 - \hat{R} \cdot \vec{\beta}} \quad (6.21)$$

Integrating with respect to the surface, we obtain the total power emitted:

$$P(t_R) = \oint d\Omega \frac{R^2}{\mu_0 c} [1 - \hat{R} \cdot \vec{\beta}] |\vec{E}_a|^2 \quad (6.22)$$

Next, we will see the power radiated by point load at low and high velocities (relativistic context).

6.3.1 Radiation emitted at low velocities

This case consists of considering a charge q moving in such a way that its speed is very low compared to the speed of light. compared to the speed of light. In this case, we can consider the limit where $\vec{\beta} \rightarrow 0$ in the Eq.(7.14),

$$\lim_{\vec{\beta} \rightarrow 0} \vec{E}_a(\vec{r}, t) = \frac{q}{4\pi\epsilon_0 c^2} \frac{(\hat{R} \cdot \vec{a}) \hat{R} - \vec{a}}{|\vec{R}|} \quad (6.23)$$

whose quadratic norm is,

$$|\vec{E}_a|^2 = \frac{q^2 |\vec{a}|^2}{16\pi^2 \epsilon_0^2 c^4 |\vec{R}|^2} \sin^2 \theta \quad (6.24)$$

The Poynting vector then becomes,

$$\vec{S} = \left(\frac{\mu_0 q^2 |\vec{a}|^2}{16\pi^2 c |\vec{R}|^2} \sin^2 \theta \right) \hat{R} \quad (6.25)$$

It is worth noting that there is no emission of radiation parallel to the acceleration of the charge, and the maximum emission is obtained in the perpendicular plane. In possession of the Poyting vector, the radiated power per unit angle Solid is given by:

$$\frac{dP}{d\Omega} = \frac{\mu_0 q^2 |\vec{a}|^2}{16\pi^2 c} \sin^2 \theta \quad (6.26)$$

Therefore, the radiated power is:

$$P = \frac{\mu_0 q^2}{6\pi c} |\vec{a}|^2 \quad (6.27)$$

This is known as the Larmor formula for the radiation emitted by the particle. It is worth noting that in this the direction of the velocity in relation to the direction of the acceleration does not matter.

For the general case where the particle's velocity and acceleration have any orientation, the electric field is given by the relation Eq.(7.14),

$$\vec{E}_a(\vec{r}, t) = \frac{q}{4\pi\epsilon_0} \frac{\vec{R}(t_R) \times (\vec{R}(t_R) - |\vec{R}(t_R)|\vec{\beta}(t_R)) \times \frac{\vec{a}(t_R)}{c}}{[|\vec{R}_{t_R}| - \vec{R}(t_R) \cdot \vec{\beta}(t_R)]^3} \quad (6.28)$$

whose squared norm $|\vec{E}_a|^2$,

$$|\vec{E}_a|^2 = \frac{|\hat{R} \times [(\hat{R} - \vec{\beta}) \times \vec{a}]|^2}{|\vec{R}|^2 [1 - \hat{R} \cdot \vec{\beta}]^6} \quad (6.29)$$

The radiated power per unit of solid angle, is given by the expression,

$$\frac{dP}{d\Omega} = \frac{\mu_0 q^2}{16\pi^2 c} \frac{|\hat{R} \times [(\hat{R} - \vec{\beta}) \times \vec{a}]|^2}{[1 - \hat{R} \cdot \vec{\beta}]^5} \quad (6.30)$$

Integrating the above expression under the solid angle Ω ,

$$P = \frac{\mu_0 q^2 \gamma^6}{6\pi c} \left[|\vec{a}|^2 - \left(\frac{\vec{v} \times \vec{a}}{c} \right)^2 \right] \quad (6.31)$$

where $\gamma = 1/\sqrt{1-\beta^2}$ is the Lorentz factor. The Eq.(7.31) is Liénard's generalization of for Larmor's formula, which is reobtained by making $|\vec{\beta}| \rightarrow 0$.

6.4 Radiation reaction

When a particle of mass m charged with a charge q undergoes the action of a resulting force not zero, it acquires an acceleration and consequently a variation in its kinetic energy. The external force, during the displacement of the particle, performs work

and by the work-energy theorem its value should be equal to the variation of kinetic energy. Meanwhile, we know what accelerated charges emit radiation, thus not all work performed is converted into kinetic energy. Part of the energy becomes radiation, and it makes it look as if the resulting force in the particle was smaller of what she is. So there's a force exerted by radiation on the charge that generated it, and that's what we call it a radiation reaction.

6.4.1 Radiation reaction based on conservation of energy

Let's determine an expression for the radiation reaction based on applying the law of conservation of energy to an accelerated charge. For simplicity's sake, let's consider a non relativistic particle, i.e. $\beta \ll 1$. With this, we can use Larmor's formula (Eq.(7.27)). This is the average power emitted, in the form of radiation, by the charge that has an acceleration a . We can think that this power corresponds to the time rate at which the charge loses energy because of the force exerted by the radiation,

$$P = -\vec{F}_{rad} \cdot \vec{v} \quad (6.32)$$

the negative sign indicates that power is being removed from the particle and v represents its velocity. Replacing Eq.(7.27) in Eq.(7.32),

$$\vec{F}_{rad} \cdot \vec{v} = -\frac{\mu_0 q^2}{6\pi c} |\vec{a}|^2 \quad (6.33)$$

It is important to note that this equation is not complete, as the charge also has velocity fields, which have an associated energy. However, the energy generated by the velocity fields does not "detach" from the charge, as is the case with radiation fields. To determine the energy lost by the charge, both the radiation and the velocity fields must be taken into account.

However, if we consider a cyclical movement over a short time interval $[t_1, t_2]$ so that the energy associated with the velocity fields will be the same at both instants. Thus, on average, the Eq.(7.33) is valid. Therefore, integrating over this interval:

$$\int_{t_1}^{t_2} dt \vec{F}_{rad} \cdot \vec{v} = - \int_{t_1}^{t_2} dt \frac{\mu_0 q^2}{6\pi c} |\vec{a}|^2 \quad (6.34)$$

which can be rewritten as:

$$\int_{t_1}^{t_2} dt \left[\vec{F}_{rad} - \frac{\mu_0 q^2}{6\pi c} \dot{\vec{a}} \right] \cdot \vec{v} = 0 \quad (6.35)$$

since this relationship must be valid for any \vec{v} , we have identified the so-called Abraham-Lorentz force for radiation reaction:

$$\vec{F}_{rad} = \frac{\mu_0 q^2}{6\pi c} \dot{\vec{a}} \quad (6.36)$$

Note that this force was established considering the simplest situation. Therefore, it only applies if we restrict ourselves to a cyclical movement in which velocity and your temporal derivate are equal at the beginning and end of the cycle.

It is interesting to consider a situation in which there is no external force acting on the particle, except for radiation. In this scenario, using Newton's second law:

$$\vec{F}_{rad} = \frac{\mu_0 q^2}{6\pi c} \dot{\vec{a}} = m\vec{a} \quad (6.37)$$

or even,

$$\frac{d\vec{a}}{dt} = \frac{6\pi mc}{\mu_0 q^2} \vec{a} \quad (6.38)$$

whose solution to this differential equation can be easily obtained,

$$\vec{a}(t) = \vec{a}_0 \exp\left\{\left[\frac{6\pi mc}{\mu_0 q^2} t\right]\right\} \quad (6.39)$$

if we define the time constant τ_{rad} by:

$$\tau_{rad} = \frac{\mu_0 q^2}{6\pi mc} \quad (6.40)$$

let's rewrite the solution as follows,

$$\vec{a}(t) = \vec{a}_0 \exp\left\{\left[\frac{t}{\tau_{rad}}\right]\right\} \quad (6.41)$$

We note that the typical τ_{rad} time is generally very small. It is also noted that the acceleration increases exponentially over time and how this result was obtained from the Larmor formula, the energy conservation is respected. Such a consequence is physically unacceptable, because this solution indicates the existence of forces associated with infinite energy. This inconsistency can be solved by $\vec{a}_0 = 0$, but the only valid solution will be trivial, i.e. $\vec{F}_{rad} = 0$.

6.5 Conclusion

The research carried out in this paper revealed that it is possible to express Maxwell's equations in electromagnetic potential terms. In this context,

the Lorenz caliber option provided a deeper analysis. It has been shown that these potentials obey a wave equation non-homogeneous, whose solution was achieved by the Green method. The introduction of the concept of time delay allowed to determine the Lienard-Wiechert potential as well as the corresponding fields. With these results in hand, we examined the ability of the Lienard-Wiechert fields to describe the radiation emitted by point charges, culminating in the derivation of the Larmor formula. Use this formula allowed the description of the radiation power associated with the force known as the force of Abraham-Lorentz. It was therefore noted that the force of Abraham-Lorentz, for the simple case, is given in terms of an exponential acceleration, without however violating energy conservation. Tal the consequence is physically unacceptable, as this solution indicates the existence of forces associated with infinite energy. One way to try to bypass this problem, initially proposed by Dirac, was using the model of a charged, rigid spherical particle (similar to the electron model) proposed by Lorentz), taking into account not only the acceleration fields, but also the terms associated with the field near the source (ou campo de velocidades). The procedure consists of make a multipolar approximation to the Lienard-Wiechert fields, enabling the calculation of the force is felt by the load elements infinitely close to the source load. We saw that such strength also it presents the same inconsistent solution of exponential acceleration.

Bibliografia

- [1] ROHRLICH, Fritz. Classical Charged Particles. 3st. ed. : World Scientific, 2007.
- [2] MACHADO, Kleber Daum. Teoria do Eletromagnetismo. 1st. ed. : Editora UEPG, 2006. v. 3.
- [3] JACKSON, John David. Classical Electrodynamics. 3rd. ed. : John Wiley & Sons, 1998.
- [4] ZANGWILL, Andrew. Modern Electrodynamics. 1st. ed. : Cambridge University Press, 2013.
- [5] BARUT, A. O. Electrodynamics and Classical Theory of Fields and Particles. 1st. ed. : Dover Publications, 1980.
- [6] F. Melia, "Electrodynamics", Chicago Lectures in Physics, Univesity of Chicago Press, 2001.

- [7] C. Brau, "Modern Problems in Classical Electrodynamics", Oxford University Press, 2004.
- [8] W. K. h. Panofsky and M. Phillips, "Classical Electricity and Magnetism", Dover Publication, Inc. (2005)
- [9] W. Rindler, "Introduction to Special Relativity, Clarendon Press, Oxford, 1991.
- [10] GRIFFITHS, David J. Introduction to Electrodynamics. 3rd. ed. : Prentice Hall, 1999.

7

Mie scattering and the first and second rainbow

Luis Augusto Pereira

Instituto de Física de São Carlos, Universidade de São Paulo, 13560-970 São Carlos, SP, Brazil

Abstract: Have you ever looked at the sky in a rainy day and asked yourself "What is that bright colored arc in the sky?". It may seem to be a simple problem easily solved by geometrical optics, but that is not the true. Over the centuries many scientists tried to give a complete quantitative explanation of the rainbow and a satisfactory one has been developed only in the past century. Here is presented part of history and theory behind the rainbow.

7.1 Introduction

The rainbow is a beautiful natural phenomena which always captivated the attention of humankind, throughout history this phenomena has appeared in several arts and myths, besides many scientists developed theories to explain those colorful arcs at the sky [1, 2, 3].



Figure 7.1: Picture of a rainbow

After a rain it is possible to see a bright arc in the sky, as shown in figure 7.1, called primary rainbow, at its inner side the sky seems more illuminated. Above outer side, higher in sky, we see a fainter arc with reversed colors sequence, called secondary rainbow. Between these two arcs the sky is darker, that

region is called Alexander's dark band, due to the Greek philosopher Alexander of Aphrodisias, who first described it in about A.D. 200 [1]. Another feature sometimes seen at the inner side of primary rainbow is faint bands pinks and greens alternately, called supernumerary arcs.

Aristotle is the first one known to try rationally explain the appearance of rainbow [1]. He believed that it was caused by an unusual reflection of sunlight from clouds at a fixed angle, giving rise to a circular cone of "rainbow rays". That explanation is not true, but he was right about the shape and perceived that the rainbow is not material object in the sky, but a set of directions where the light is strongly scattered into the eyes of the observer.

In 1266, Roger Bacon measured the angle formed by the rainbow rays, he measured an angle about 42 degrees for the primary rainbow and the secondary about 8 degrees higher. Nowadays, these angles are measured in opposite direction so that the angle measured is the total deflection in the path of sunlight, which gives about 180 minus 42 degrees, that is 138, to primary rainbow and 130 degrees to secondary rainbow. Past few years, Theodoric of Freiberg, rejected the Aristotle's idea of the rainbow results from a collective reflection of raindrop clouds, but instead each drop produces a rainbow. He made an experiment using a flask filled with water to simulate a raindrop and proved his hypothesis, although his discoveries remained unknown until Descartes rediscovered Theodoric ideas, independently, by the same method. Utilizing the laws of reflection and refraction Descartes was able to explain the existence of the rainbow [1].

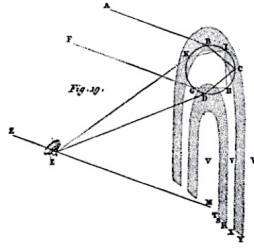


Figure 7.2: schematic draw of Descartes's experiment: a person looking at the two rainbows produced by a flask filled with water.

The explanation about how the rainbow occurs was that the sunlight is refracted into the water drop and inside the drop it is reflected backwards, so in order to see a rainbow an observer must be somewhere between the sun and the water drop.

The colors was explained by Newton in his experiment of light dispersion in prism, showing that the white light is composed by a mixture of colors.

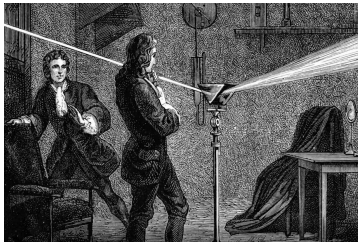


Figure 7.3: Newton using a prism to decompose light.

7.2 The rainbow

7.2.1 The first rainbow

As the rainbow is caused by the water droplets suspended in the air, to understand how it occurs we need to understand what happens when the light hits the droplet, here considered as a perfect sphere, at a angle α . In such situation the ray of light that comes at the water droplet surface is partially reflected and partially refracted, at a angle β , penetrating the medium. Inside the droplet the refracted ray follow its path until it hits another surface of the sphere where, again, it will be partially reflected, staying inside the water, and partially refracted, coming back to the air. This process goes on until the intensity of the ray vanishes.

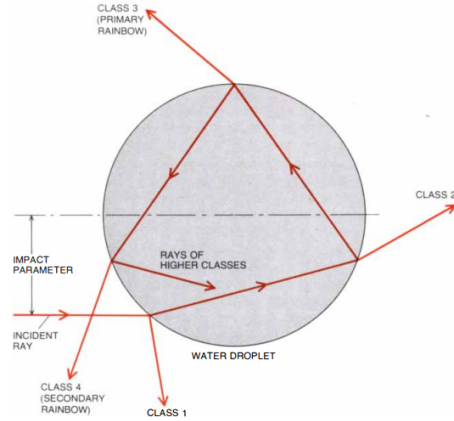


Figure 7.4: Path of ray of light through a droplet. The class 3 ray, once reflected ray, is the responsible for the rainbow. The class 4 ray, twice reflected ray, is the responsible for the secondary rainbow. The impact parameter is the distance of incident ray to center of droplet. Source: Nussenzveig, H. M. [1].

The relation between the angle of incidence and refraction is given by the Law of Snell

$$n_1 \sin \alpha = n_2 \sin \beta \quad (7.1)$$

where $n_1 \approx 1$ and $n_2 = 1.33$ are the refractive indices of the air and the water, respectively. We are interested in the ray of light that produces the primary rainbow, so we shall see the deflection in the path of this ray

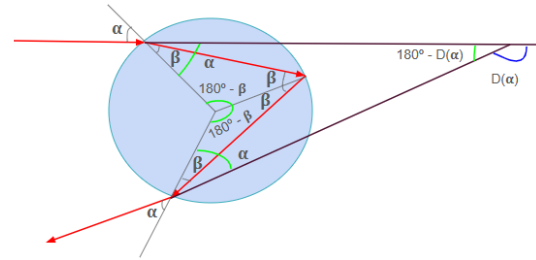


Figure 7.5: Path of ray once reflected. Source: produced by the author.

by geometry the green angles must sum 360° , so

$$2(180 - 2\beta) + 2\alpha + 180 - D(\alpha) = 360 \quad (7.2)$$

$$D(\alpha) = 180 - 4\beta + 2\alpha \quad (7.3)$$

By equation (8.1) $\beta = \arcsin(\sin(\alpha)/1.33)$. Hence

$$D(\alpha) = 180 - 4 \arcsin(\sin(\alpha)/1.33) + 2\alpha \quad (7.4)$$

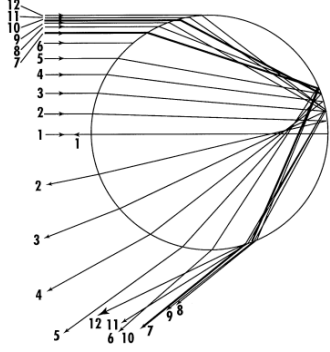


Figure 7.6: Paths of various rays through a water drop at different angles. Source: Adam, J. A. [4]

If we analyze the plot of this function we shall see a minimum, where around this point the deflection barely changes, which means there is a certain angle at around it there is a concentration of the rays, that fact is represented in figure 7.6. To find the minimum we can derivative the expression

$$\frac{d}{d\alpha} D(\alpha) = 2 - \frac{3 \cos \alpha}{\sqrt{1 - \left(\frac{3 \sin \alpha}{4}\right)^2}} = 0 \quad (7.5)$$

After manipulating this equation one can obtain the following result $\sin \alpha = \sqrt{\frac{20}{27}}$, which leads to $\alpha = 59.4^\circ$. Hence, $D(\alpha) = 138^\circ$, that means in such situation when we look at the drop at 42° we see a concentration of ray lights.

But because of Newton's study on optics we know the sunlight is a mixture of colored rays and each color have your own refractive index this means that each one will follow its own path through the drop, resulting in the concentration of each color at defined angles, giving rise to a rainbow. Assuming that the light spectrum ranges from blue to red, it is sufficient to evaluate only these two deflection angles to understand the primary rainbow. As for red light $n_r \approx 1.33$ and for blue light $n_b \approx 1.34$, we get as rainbow angles 42° and 40° , respectively. That is why we see the primary rainbow at the sky and because no light is reflected higher than 42° the sky is darker above red arc and as there is no concentration lower than 40° the sky is filled with white light.

7.2.2 The second rainbow

To understand the formation of second rainbow we need to analyze the deflection in the path of a ray twice reflected as shown in figure 7.4.

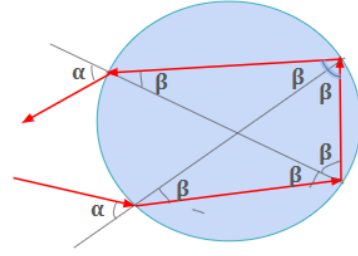


Figure 7.7: Paths of a ray twice reflected. Source: produced by the author

As in the previous case, we need to evaluate $D(\alpha)$ but this time it is counterclockwise.

$$D(\alpha) = 2\alpha - 6\beta + 360^\circ \quad (7.6)$$

Again, to find its minimum we derive the expression,

$$\frac{d}{d\alpha} D(\alpha) = 0 \quad (7.7)$$

after some calculations we obtain

$$\cos(\alpha) = \sqrt{\frac{n_2^2 - 1}{8}} \quad (7.8)$$

where n_2 is the refractive index of red light at water. Hence, we obtain a minimum angle $\alpha = 71.8^\circ$ where happens the concentration, which means the deflection angle is $D(\alpha) = 231^\circ$ and rainbow angle equals to 51° . For blue light, the calculations leads to an angle equals to 54° , that is, now the rainbow has the colors reversed and there is a minimum angle where we can see the light instead a maximum as in the case of primary rainbow, confirming the dark zone of Alexander's dark band. The fact ray light loses intensity through the path explain why secondary rainbow is fainter.

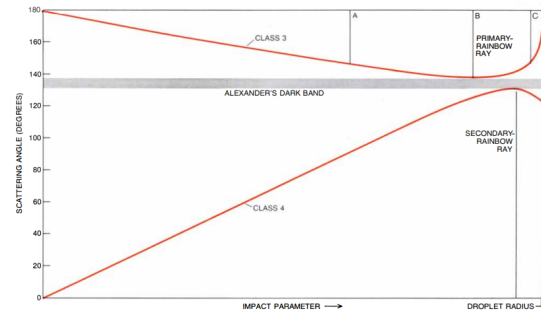


Figure 7.8: Behavior of deflection rays as we change the impact parameter, the behavior is the same when used incident angle as parameter. Source: Nussenzveig, H. M. [1].

7.3 Beyond the geometrical optics

7.4 Conclusion

Bibliografia

- [1] Nussenzweig, H. M. "The theory of the rainbow." *Scientific American* 236.4 (1977): 116-128.
- [2] Anuradha, S. Rainbows in Art History: A Symbol of Hope for a Better Future. 3 april 2023. Available on: <https://www.dailyartmagazine.com/rainbows-in-art-history/>. Accessed: 21 november 2023.
- [3] Faena Aleph. Rainbows: A Journey Through Their History in Art. Available on: <https://www.faena.com/aleph/rainbows-a-journey-through-their-history-in-art>. Accessed: 21 november 2023.
- [4] Adam, J. A. "The mathematical physics of rainbows and glories." *Physics reports* 356.4-5 (2002): 229-365.

8

The free-electron laser

Marcelo da Silva Cruz

Instituto de Física de São Carlos, Universidade de São Paulo, 13560-970 São Carlos, SP, Brazil

Abstract: The topic of this paper is the free-electron laser (FEL), a brief theoretical review and its applications and variations. The FEL uses a wiggler to accelerate the electrons in the cavity, they produces a very short and intense light pulses. Furthermore, the FEL is monochromatic and adjustable in a wide energy range, the light produced is polarised (spin polarised). During the interaction between the electrons and an incident beam, the beam will be modulated in energy. The result is a spatial modulation, which allows the emitted radiation to be coherent.

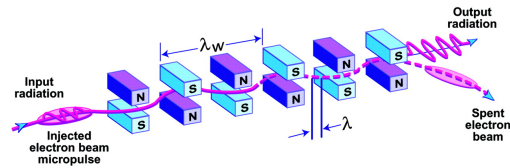


Figure 8.1: Schematic illustration of the interaction between the electron beam and the wiggler in an FEL with a planar wiggler [4]. Source: Freund H. P., Neil G. R., Proc. IEEE 87, 782 (1999).

8.1 Introduction

8.1.1 A new kind of laser

The invention of the free-electron lasers, also know as FELs, is an important chapter in the history of science, technology and and mankind itself [1]. It was invented by the physicist John M. J. Madey using the technology developed by Hans Motz and his colleagues pioneered the development of technology by constructing an undulator [2] and experimentally demonstrated by his group at Stanford University in the 1970s [3]. The creation of a FEL requires the use of radiation caused by beams of relativistic electrons subjected to the movement of a periodic transverse magnetic field. Incoherent synchrotron light sources also utilize undulators. The process of lasing occurs as a result of the radiation and wiggler coming together to create a beat wave. This beat wave, also known as a ponderomotive wave, is essentially an interference pattern that moves at a slower pace than the speed of light and can be synchronized with the electron. Furthermore, in the figure 8.1 we can see how the FEL works in a schematic example.

In comparison with a usual laser, instead of rely-

ing on stimulated emission from atomic or molecular sources, it utilizes relativistic electrons as the amplifying medium. It's need to be contemplate the fact of scattering process of virtual photons using the radiation emitted in the $+\hat{z}$ direction and can be improve on due the stimulated emission in the presence of a magnetic field [1], showed in the figure 8.2 and in the figure 8.3.

The stimulated emission occurs due the presence of the creation operator a^* in the Hamiltonian of interaction, and can be explicated by the initial state. Besides, the transition rate and his factor $\sqrt{n+1}$ in the matrix element is the number of photons had been stimulated in the process per unit volume [1]. The absorption in electron absorbs one of the high energy photons $\lambda_f = \frac{\lambda_q}{2\gamma^2}$, with λ_q as the wiggler (or undulator) wavelength and $\gamma = \sqrt{1 - \frac{v^2}{c^2}}$, and radiates a low energy photon into the equivalent plane wave [1]. For $n \gg 1$, the absorption and emission rates become nearly equal. The only distinction between the two rates for large n is in terms of kinematics. Both processes draw from the same population of electrons [1].

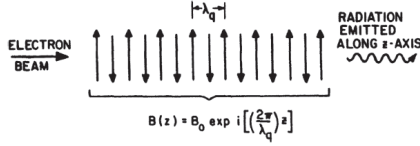


Figure 8.2: Example of radiation by a relativistic electron beam in a periodic transverse magnetic field [1]. Source: Madey M. J., Schwettman H. A. and Fairbank W. M., 1973 A free electron laser IEEE Trans. Nucl. Sci. NS-20980.

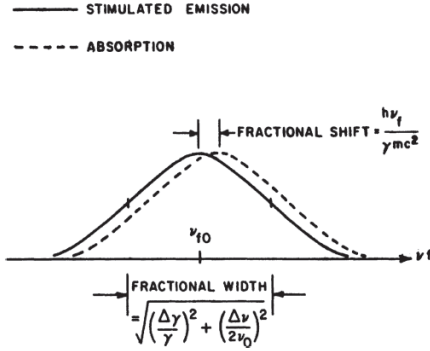


Figure 8.3: Example of lineshape for stimulated emission and absorption. [1]. Source: Madey M. J., Schwettman H. A. and Fairbank W. M., 1973 A free electron laser IEEE Trans. Nucl. Sci. NS-20980.

8.2 Theoretical revision

The atomic theory for lasers was modeled by Maxwell's equations for electrical field, in addition, the Schrödinger equation was required to describe the atom. Still in the meantime these equations is coupled via the polarization vector to FEL treatment and the vector potential \vec{A} , the Boltzmann equation for electrons density f was considered too. The vector potential submit the electron ponderomotive potential on the electrons and the Boltzmann equation is inherited in the case that is necessary to determine the electron distribution function and hence the radiating current [1].

In the work published by [5] and [6] they replaces the static magnetic field of period λ_q , by an electromagnetic field of wavelength λ_i :

$$\lambda_i = (1 + \beta)\lambda_q \simeq 2\lambda_q \quad (8.1)$$

where

$$\beta \equiv 1 - \frac{1}{\gamma^2} \quad (8.2)$$

And the motion of the electron distribution $f(x, \vec{P}, t)$ by the collisionless relativistic Boltzmann equation is given by equation 8.3:

$$\frac{df}{dt} = \frac{\partial f}{\partial t} + \dot{x}_i \frac{\partial f}{\partial x_i} + \dot{P}_i \frac{\partial f}{\partial P_i} = 0 \quad (8.3)$$

where \vec{P} as the canonical momentum and x the position. All the number of electrons $N(t)$ is:

$$N(t) = \int x d^3t \int f(x, \vec{P}, t) d^3 \quad (8.4)$$

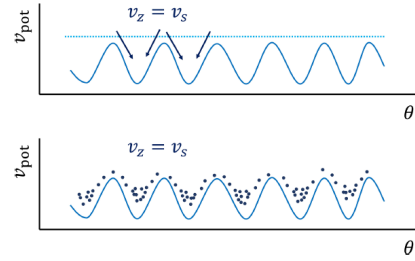


Figure 8.4: The number of incident electrons are shown stationary with respect to the growing potential. The phase of the growing potential is calculated by $\theta = (\omega_s - \omega_i)t - (k_i - k_s)\hat{z}$ [1].

Furthermore, we have the Boltzmann equation and his relation with the coupled by a transverse current \vec{J}_\perp to the vector potential in equation 8.5:

$$\nabla^2 \vec{A} - \frac{1}{c^2} \frac{\partial^2 \vec{A}}{\partial t^2} = \mu_0 \vec{J}_\perp \quad (8.5)$$

with \vec{A} as the vector potential, and

$$\vec{J}_\perp(x, \vec{P}, t) \equiv e \int d^3 P \vec{v}_\perp f(x, \vec{P}, t) \quad (8.6)$$

We have e as the electron charge and \vec{v}_\perp being the transverse component of the electron velocity. Now, we can factorize the electron distribution using a Heaviside function $u(x)$ for circular beam and two-dimensional delta-function δ^2 :

$$f(x, \vec{P}, t) = [u(r) - u(r - a)] \delta^2(\vec{P}_\perp) h(z, p_z, t) \quad (8.7)$$

So, the Boltzmann equation can be reduced in this form:

$$\frac{\partial h}{\partial t} + \frac{p_z}{m\gamma} \frac{\partial h}{\partial z} = \frac{e^2}{m\gamma} \frac{\partial^2 A_z^2}{\partial z^2} \quad (8.8)$$

additionally the Maxwell equation takes form:

$$\left(\frac{\partial^2}{\partial z^2} - \frac{1}{c^2} \frac{\partial^2}{\partial t^2}\right) \vec{A}_t = \frac{e^2 \kappa}{m c \epsilon_0} \vec{A}_t \int_{-\infty}^{\infty} \frac{h(z, p_z, t)}{\gamma} dp_z$$

and $\kappa = \frac{a^2}{b^2}$ as the filling factor with b as the radius of the cavity.

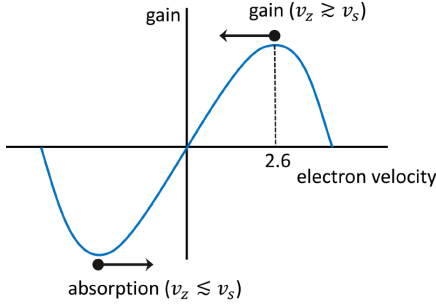


Figure 8.5: Gain versus electron velocity, that is the ‘detuning’ parameter $\mu = \Delta\omega\left(\frac{1}{v_s} - \frac{1}{v_z}\right)$ [1].

Besides, the potential \vec{A}_i^2 occurs on the right-hand side of the equation 8.8 in source of the ponderomotive potential driving the electrons. And this is given by:

$$A_i^* A_s e^{-i(\omega_s - \omega_i)t - (k_i + k_s)z} \quad (8.9)$$

the incident field by the wiggler can be seen by the electrons and this implies that $\omega_i = ck_i$ and $k_i = \frac{2\pi}{\lambda_w}$, λ_w is the wiggler period.

So, now we have the phase velocity of the potential, and the Boltzmann equation yields:

$$v_p = \frac{\omega_s - \omega_i}{k_s + k_i} = \frac{\Delta\omega}{k} \quad (8.10)$$

and

$$k_s \simeq 4\gamma_s^2$$

with

$$\gamma_s = \frac{1}{\sqrt{1 - \frac{v_s^2}{c^2}}} \quad (8.11)$$

The electrons in FEL enter in a initial condition with equal velocity to the resonant velocity of potential, v_s , and are therefore almost stationary compared the bunching velocities. To get the gain, its need to consider $v_z \geq v_s$ and when $v_z \leq v_s$, we have the Landau damping as the dominant phenomenon, and the electrons can absorb energy from the field.

In the next section of this work, will be discuss about the first experiment in Stanford University.

8.3 The Stanford experiment

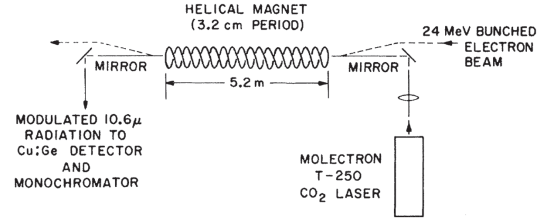


Figure 8.6: Experimental Setup. The electron beam is magnetically deflected around an optical element on the axis of the helical magnet. Source: Madey, John; Scully, Marlan O.; Sprangle, Phillip. (Copyrighted by the American Physical Society 1976.) [1].

The experiment consists in a magnetic field of 5.2 mT formed by a superconducting spiral with a period of 3.2 cm. The beam and infrared field extend along the axis. Infrared light from a CO_2 laser with transverse excitation and an atmospheric beam waist of 3.3 mm excited the mode of a 10.2 mm copper tube. The gain was measured at optical powers of $1.4 \times 10^5 Wcm^{-2}$. In the figure 8.7 they utilized a right-circular polarization, and the gain was vanished for the left-circular [1].

8.3.1 The coupled wave of FEL

The coupled wave is known as the FEL mechanism and your interaction mechanism can be seen in coupling of 3 waves, one electromagnetic and two electron beam (ponderomotive) waves, which are also electromagnetic. The wave propagates in the same direction as the electron beam and has a phase velocity that almost corresponds to the electron beam velocity $v_z \leq c$. The FEL has a number of similarities with wave radiation travelling in a generating mechanism. There is a unmodulated or unbunched electron beam propagating through a wiggler field which radiates incoherent synchrotron radiation.

The Gain corresponds to a positive signal. The instantaneous peak gain reached 7 on each trial. The spiral field amplitude is 2.4 kG, and the instantaneous peak electron current is 70 mA. The electron energy passes through a small range of nearly 24 MeV. The full energy width (half width of wavelength) of point $\frac{1}{e}$ in (a) is 0.4 %. The power density of the 10.6 μm radiation in (b) is $1.4 \times 10^5 Wcm^{-2}$ [1].

The FEL dispersion relationship reveals different

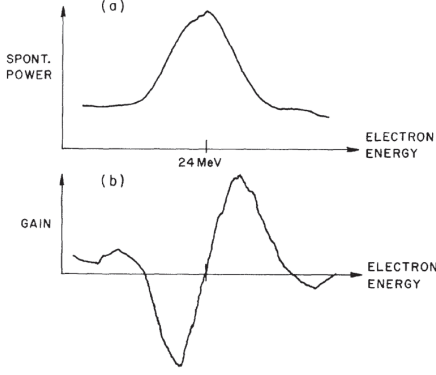


Figure 8.7: (a) Spontaneous power at $10.6 \mu\text{m}$ as a function of electron energy. (b) Amplitude and phase of applied modulation of $10.6 \mu\text{m}$ optical radiation from a CO₂ laser. Source: Madey, John; Scully, Marlan O.; Sprangle, Phillip. (Copyrighted by the American Physical Society 1976) [1].

operating states. The dispersion relationship can be viewed as the space and time Fourier transform of the wave equation 8.5 [1]. Furthermore, dispersion relation indicates the relationship between the frequency and wavenumbers of the waves generated in the FEL interaction and is given by:

$$\left(k - \frac{\omega}{c}\right) \left(k + k_2 - \frac{\omega}{v_z}\right)^2 = -K_c^3 \quad (8.12)$$

and we have $k = \frac{2\pi}{\lambda}$ as the radiation wavenumber, ω the frequency and:

$$K_c^3 = \left(\frac{\pi}{2}\right) \left(\gamma^{-3} \frac{\omega_b^2}{c^2}\right) \frac{a_w^2}{\lambda_w}$$

K_c^3 is the coupling coefficient, and ω_b^2 is proportional to the electron beam density, and a_w^2 the wiggler field amplitude. The strongest coupling between the three waves occur when the three wavenumbers are nearly matched.

8.3.2 Low-gain

We consider here the case of an FEL amplifier which is seeded by an external laser and energy conservation tells us that the light wave gains energy if the electron loses energy [12].

In low gain mode, the gain per channel is much less than unit; this is the system first proposed by Madey et al [1]. In this mechanism, the coupling coefficient is small, with three waves excited by an electron beam. Waves have a constant amplitude,

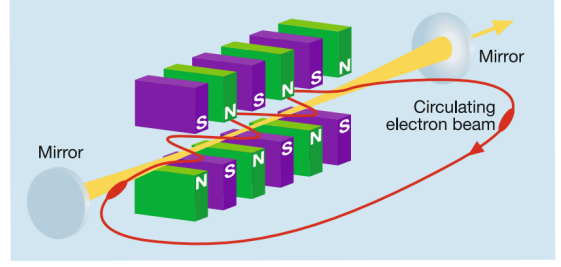


Figure 8.8: Example of Low Gain mode for FEL. Source: Schmüser, Peter, et al. [12].

the first one decreases slightly and the third one increases slightly as a function of propagation distance [1].

8.3.3 High-gain

In this case, the coupling coefficient is maximum, and solving the dispersion relation equation $\omega = (1 + \frac{v_z}{c})\gamma^2$ gives wavenumber shifts dominate due to Plasma waves, therefore no plasma waves are excited. Here, Radiation initially increases exponentially in space until electrons are trapped in plasmodynamic waves [1]. The production of Free Electron Laser (FEL) light is achieved through the higher harmonics of external seed radiation, employing the High-Gain Harmonic Generation (HGHG) process. [12].

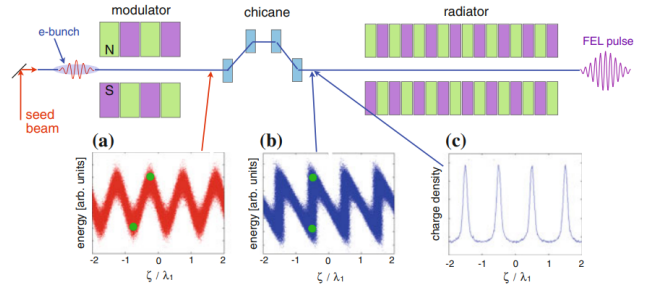


Figure 8.9: Principle of the high-gain harmonic generation process. The top graph shows the experimental setup. Source: Schmüser, Peter, et al. [12].

The Fourier expansion of $\rho(\zeta)$ contains higher harmonics with angular frequencies $\omega n = n\omega_1$ and wavelengths $\lambda n = \frac{\lambda_1}{n}$. The longitudinal phase space distributions are displayed in the bottom graphs (courtesy of D. Xiang, apud the author of this paper). The energy distribution in the bunch is plotted as a function of $\frac{\zeta}{\lambda_1}$. a) Downstream of the

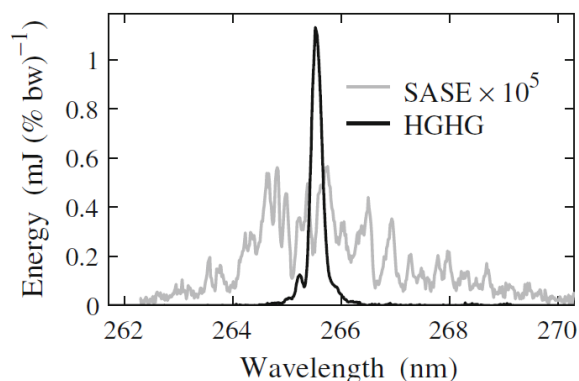


Figure 8.10: A single-shot spectrum was acquired at the Deep Ultraviolet Free-Electron Laser (DUV FEL) using a 30MW seed beam. The gray line represents the spectrum of a single-shot Self-Amplified Spontaneous Emission (SASE) far below saturation, measured in the absence of the seed beam. Source:[12].

modulator, b) downstream of the magnetic chicane. Graph c) shows the microbunching: charge density as a function of $\frac{\zeta}{\lambda_1}$.

The initial experimental findings regarding high-gain harmonic generation in the ultraviolet were achieved using the deep ultraviolet free-electron laser at Brookhaven National Laboratory [13].

A Ti:Sa laser was employed to generate the seed beam with a wavelength λ_1 of 800 nm, facilitating the production of third-harmonic radiation at 266 nm. The results, as depicted in Figure 8.10, validated the anticipated outcomes for HGFG FEL operation, including a stable wavelength spectrum, narrow bandwidth, and minimal pulse-energy fluctuations.

8.4 Modern applications

The FEL have been operated from the microwave to the vacuum ultraviolet regions, the future for this application is the field of high energy light and shorter wavelengths [4]. Almost 20 years ago, there is a record average power of $1.7kW$ and has been produced at wavelength of $3\mu m$ [5].

There is some interesting applications in the Condensed Matter like, using the FEL in IR range: Surface science with Catalysis, Adsorption, Selective excitation of surface layer or adsorbed molecule. Semiconductor with High Tc SC bandgap, Carrier dynamics and electron gas dynamics at metal-

insulator junction. Superconductors an Magnetic properties [9].

In the field of Chemistry, the FEL has applications in IR range: Molecular Vibrational Excitation, Reaction Dynamics, Photochemistry, Molecular Clusters (Van der Waals - molecule), Electronic Excitations (UV range), Raman Spectroscopy (UV range) and Crossed Photon-Molecular Beams (UV range) [9]

At Biology field, the FEL is applied in Microscopy, Halography, Cellular Dynamics ($1 - 3nm$) and DNA sequencing ($0.1 - 1nm$) [9].

In Military applications, the Thomas Jefferson National Accelerator Facility Lab manages a high-average-power, sub-picosecond free-electron laser in the kilowatt class, spanning the mid-infrared spectral range. On July 21, 2004, a milestone of 10 kilowatts in continuous wave (cw) operation was reached. Future plans include extending the Free-Electron Laser (FEL) capabilities to cover 250nm in the ultraviolet (UV) range. Additionally, the short electron pulses generate hundreds of watts of broadband terahertz (THz) light, accessible to researchers in a dedicated user laboratory [14].

In medicine, they can use FEL in Surgery ($3\mu m$) and Photoheray-selective absorption in pigment elements ($0.7 - 1\mu m$) [9].

8.4.1 Optical guidance

Optical guidance of radiation is crucial for a high performance in FEL amplifier. Operate FEL to high gain Amplifiers with interaction lengths much larger than diffraction length (Rayleigh) requires optical guidance radiation. This is especially true for FEL amplifiers operate in the IR, optical or X-ray range and fold FEL radiation length ratio Interaction length (swing length). In the X-ray region, e.g. For example, the E-fold length of a radiation can be hundreds of meter. This is what happens when there is no visual guidance get out of it before it gets reinforced [1].

8.4.2 Generation of radiation

The terahertz (THz) frequency range occupies a position between the radio and infrared bands, encompassing both photonic and electronic methodologies across the expansive electromagnetic spectrum. Recent technological progress in THz science has led to an extension of this frequency window, now incorporating a portion of the infrared (IR) spectrum. The updated "Terahertz Science and Technology Roadmap" has expanded upon the previous definition of the THz band ($0.1-10$ THz), now

defining its frequency range up to 30 THz [11].

Accelerator-based sources produce coherent high-field terahertz (THz) radiation through ultra-short relativistic electron bunches. Utilizing linear accelerators, electron bunches are generated to emit fully coherent (super-radiant) THz radiation, with the intensity directly proportional to the number of electrons emitting radiation in phase. The attainment of super-radiant and high-field THz emission in these sources necessitates ultra-short electron bunches or density modulation at THz frequencies [11].

8.5 Conclusion

In conclusion, FEL is a new type of laser that promises great advances in modern science. Its construction requires a considerable investment and it was only possible to create it from complete theories of Electromagnetism, Relativity, Quantum Mechanics and Atomic Physics. The possibility of creating electron beams accelerated by magnetic undulators is fascinating and capable of producing an intense beam of coherent light with high intensity and power. Its applications range from condensed matter physics to biology, medicine, military and chemistry. It possible to use the FEL in UV and IR band, with low and high harmonic generations, furthermore, the terahertz frequency range can be studied using a FEL with very applied technologies in photonics and electronics devices.

Bibliografia

- [1] Madey, John; Scully, Marlan O.; Sprangle, Phillip. The free electron laser: conceptual history. *Physica Scripta*, v. 91, n. 8, p. 083003, 2016.
- [2] Motz, Hans. Applications of the radiation from fast electron beams. *Journal of Applied Physics*, v. 22, n. 5, p. 527-535, 1951.
- [3] Huang, Zhirong; Kim, Kwang-Je. Review of x-ray free-electron laser theory. *Physical Review Special Topics-Accelerators and Beams*, v. 10, n. 3, p. 034801, 2007.
- [4] Patrick G. O'Shea, Henry P. Freund; Free-Electron Lasers: Status and Applications. *Science* 292, 1853-1858 (2001).
- [5] G. R. Neil et al., Sustained Kilowatt Lasing in a Free-Electron Laser with Same-Cell Energy Recovery. *Phys. Rev. Lett.* 84, 662 (2000)
- [6] Weizsäcker C. F., Ausstrahlung bei Stößen sehr schneller elektronen *Z. Phys.* 88 612, 1934.
- [7] Williams E. J., Nature of the high energy particles of penetrating radiation and status of ionization and radiation formulae, *Phys. Rev.* 45 729, 1934.
- [8] Kroll N. M. and McMullin W. A. ; 1978 Stimulated emission from relativistic electrons passing through a spatially periodic transverse magnetic field *Phys. Rev. A* 17 300
- [9] Pellegrini, C. "Free electron lasers: Development and applications." *Part. Accel.* 33 (1990): 159-170.
- [10] Pellegrini, C.. "The history of X-ray free-electron lasers." *The European Physical Journal H* 37.5 (2012): 659-708.
- [11] Koral, C., Mazaheri, Z., Papari, G. P., Andreone, A., Drebot, I., Giove, D., ... & Serafini, L. (2022). Multi-pass free electron laser assisted spectral and imaging applications in the terahertz/far-IR range using the future superconducting electron source BriXSinO. *Frontiers in Physics*, 10, 127.
- [12] Schmäuser, Peter, et al. "Free-electron lasers in the ultraviolet and X-ray regime." *Springer Tracts in Modern Physics* 258 (2014).
- [13] L.-H. Yu et al., First ultraviolet high-gain harmonic-generation free-electron laser. *Phys. Rev. Lett.* 91, 074801 (2003)
- [14] Jefferson Lab FEL; Archived from the original: <https://www.jlab.org/FEL>

9

Bremsstrahlung

Nathan Barbola Marucci

Instituto de Física de São Carlos, Universidade de São Paulo, 13560-970 São Carlos, SP, Brazil

Abstract: Bremsstrahlung radiation, or braking radiation, is emitted by a charged particle undergoing acceleration and can be classified into two types: external Bremsstrahlung and internal Bremsstrahlung. External Bremsstrahlung occurs, for example, when charged particles are scattered by an atomic nucleus, while internal Bremsstrahlung originates within the atom and is associated with processes involving changes in nuclear charge. This monograph will discuss these two types of processes. In the case of scattering due to the Coulomb potential, it will be demonstrated that semiclassical arguments can lead to the correct results predicted by quantum mechanics. Furthermore, because X-rays are closely related to Bremsstrahlung and have various interesting applications—from medical physics to astrophysics—their generation and spectrum will be explored.

9.1 Introduction

In 1895, W.C. Rontgen[1], by discharging a large induction coil in a vacuum tube surrounded by black paper, observed that when approaching another piece of paper covered on one side with barium platinocyanide, it fluoresced. This illumination occurred regardless of whether the painted side or the other side was facing the tube. The fluorescence was so intense that it could be observed from a distance of up to 2 meters. Thus, Rontgen noted the presence of an "agent" capable of penetrating black cardboards that were otherwise quite opaque to ultraviolet light or sunlight. He continued his investigations into how other substances could be penetrated by this "agent" and discovered, for example, that if a hand was placed between the tube and the fluorescent screen, a dark image of the bones would form (Figure 9.1). For simplicity, Rontgen named this "agent" X-rays.



Figure 9.1: Photograph of the bones of a live person's finger

The X-ray spectrum can be separated into two components (Figure 9.2): a characteristic line spectrum and a continuous spectrum. It was only 18 years after the discovery of X-rays that Sommerfeld, with Rontgen's approval, proposed the name *bremsstrahlung* (braking radiation) for the continuous spectrum.

9.2 Radiation emitted by a point charge

As we know from the classical theory of electrodynamics, the electric and magnetic fields generated by a point particle of charge e moving with velocity βc are given by[2]:

$$\begin{aligned} \mathbf{B} &= [\mathbf{n} \times \mathbf{E}]_{\text{ret}} \\ \mathbf{E} &= e \left[\frac{\mathbf{n} - \boldsymbol{\beta}}{\gamma(1 - \boldsymbol{\beta} \cdot \mathbf{n})^3 R^2} \right]_{\text{ret}} + \frac{e}{c} \left[\frac{\mathbf{n} \times (\mathbf{n} - \boldsymbol{\beta}) \times \dot{\boldsymbol{\beta}}}{(1 - \boldsymbol{\beta} \cdot \mathbf{n})^3 R} \right]_{\text{ret}} \end{aligned} \tag{9.1}$$

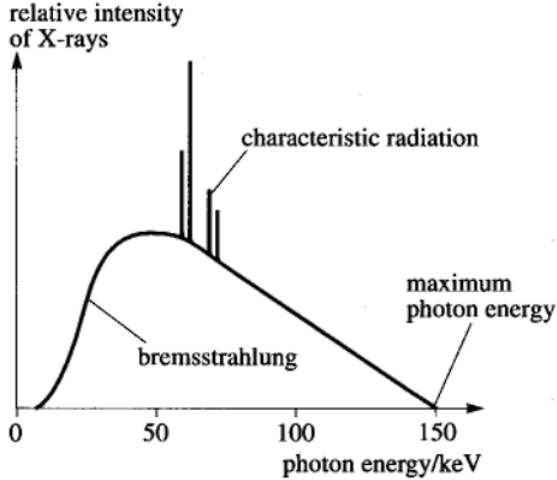


Figure 9.2: X-ray Spectrum

In the above equation, \mathbf{n} is the unit vector pointing from the particle's position to the observation point where the field is calculated; $\gamma \equiv 1/\sqrt{1-\beta^2}$ is the Lorentz factor; and the subscript "ret" serves to remind us that the quantity in square brackets should be evaluated at the retarded time, t_r , such that:

$$t_r = t - R(t_r)/c \quad (9.2)$$

In the expression for the electric field in Equation 9.1, the first term is called the velocity field and is independent of acceleration. The second term is called the acceleration field since it depends linearly on $\dot{\beta}$. The velocity field, as it decreases with R^{-2} , is essentially a static field; whereas the acceleration field, decreasing with R^{-1} , is responsible for the radiation emitted by the particle.

Indeed, consider a particle moving near the origin of our coordinate system and a sphere of radius R centered at the same (Figure 9.3). The radiated power, P_{rad} , by the particle is given by:

$$P_{\text{rad}} = \lim_{R \rightarrow \infty} \oint \mathbf{S} \cdot d\mathbf{a} \quad (9.3)$$

where the Poynting vector, \mathbf{S} , is given by:

$$\mathbf{S} = \frac{c}{4\pi} \mathbf{E} \times \mathbf{B} = \frac{c}{4\pi} \mathbf{E} \times (\mathbf{n} \times \mathbf{E}) = \frac{c}{4\pi} |\mathbf{E}|^2 \mathbf{n} \quad (9.4)$$

Thus, as the area of the sphere grows with $4\pi R^2$, in order for the radiated power to remain constant when taking the limit as R tends to infinity, we must impose that \mathbf{S} scales with R^{-2} , and this only occurs due to the presence of the acceleration field, \mathbf{E}_a , in Equation 9.1.

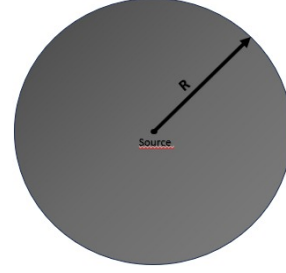


Figure 9.3: Sphere over which we are calculating the flux.

9.2.1 Distribution in Frequency and Angle of Energy Radiated by Accelerated Charges

Thus, the energy flux per unit time carried by radiation is given by:

$$P = \int \frac{c}{4\pi} |\mathbf{E}_a|^2 R^2 d\Omega \quad (9.5)$$

It follows, therefore, that the radiated power per solid angle is:

$$\frac{dP}{d\Omega} = |\mathbf{A}(t)|^2 \quad \text{where} \quad \mathbf{A}(t) = \left(\frac{c}{4\pi}\right)^{1/2} R \mathbf{E}_a \quad (9.6)$$

The total energy radiated per solid angle is obtained by integrating Equation 9.6 over time:

$$\frac{dW}{d\Omega} = \int_{-\infty}^{\infty} |\mathbf{A}(t)|^2 dt \quad (9.7)$$

Now, according to Parseval's theorem, we must have:

$$\frac{dW}{d\Omega} = \int_{-\infty}^{\infty} |\mathbf{A}(\omega)|^2 d\omega \quad (9.8)$$

where we introduced the Fourier transform, $\mathbf{A}(\omega)$, of $\mathbf{A}(t)$, such that:

$$\begin{aligned} \mathbf{A}(\omega) &= \frac{1}{\sqrt{2\pi}} \int_{-\infty}^{\infty} \mathbf{A}(t) e^{i\omega t} dt \\ \mathbf{A}(t) &= \frac{1}{\sqrt{2\pi}} \int_{-\infty}^{\infty} \mathbf{A}(\omega) e^{-i\omega t} d\omega \end{aligned} \quad (9.9)$$

Since negative frequencies have no physical meaning, it is customary to integrate Equation 9.8 only over positive frequencies, so that:

$$\frac{dW}{d\Omega} = \int_0^{\infty} \frac{d^2 I}{d\omega d\Omega} d\omega \quad (9.10)$$

The integrand of Equation 9.10 is nothing more than the energy radiated per unit solid angle and

per frequency interval. Thus, we must have:

$$\frac{d^2 I}{d\omega d\Omega} = |\mathbf{A}(\omega)|^2 + |\mathbf{A}(-\omega)|^2 \quad (9.11)$$

And, since $\mathbf{A}(t)$ is real, it is easy to see from Equation 9.9 that $\mathbf{A}(\omega) = \mathbf{A}(-\omega)$, so that:

$$\frac{d^2 I}{d\omega d\Omega} = 2|\mathbf{A}(\omega)|^2 \quad (9.12)$$

Therefore, let:

$$\mathbf{A}(\omega) = \left(\frac{e^2}{8\pi^2 c} \right)^{1/2} \int_{-\infty}^{\infty} \left[\frac{\mathbf{n} \times (\mathbf{n} - \boldsymbol{\beta}) \times \dot{\boldsymbol{\beta}}}{(1 - \boldsymbol{\beta} \cdot \mathbf{n})^3} \right]_{\text{ret}} e^{i\omega t} dt \quad (9.13)$$

It is interesting to make the variable change from t to t_r , obtaining the result:

$$\mathbf{A}(\omega) = \left(\frac{e^2}{8\pi^2 c} \right)^{1/2} \int_{-\infty}^{\infty} \frac{\mathbf{n} \times (\mathbf{n} - \boldsymbol{\beta}) \times \dot{\boldsymbol{\beta}}}{(1 - \boldsymbol{\beta} \cdot \mathbf{n})^2} e^{i\omega[t_r + R(t_r)/c]} dt_r \quad (9.14)$$

Since the observation point is assumed to be far from the charge, the unit vector \mathbf{n} is practically constant over time, so that:

$$R(t_r) \approx x - \mathbf{n} \cdot \mathbf{r}(t_r) \quad (9.15)$$

Where x is the distance from the observation point to the origin O , and \mathbf{r} is the position vector of the particle (Figure 9.4). Thus, up to an overall phase factor, we will have:

$$\mathbf{A}(\omega) = \left(\frac{e^2}{8\pi^2 c} \right)^{1/2} \int_{-\infty}^{\infty} \frac{\mathbf{n} \times (\mathbf{n} - \boldsymbol{\beta}) \times \dot{\boldsymbol{\beta}}}{(1 - \boldsymbol{\beta} \cdot \mathbf{n})^2} e^{i\omega(t - \mathbf{n} \cdot \mathbf{r}/c)} dt \quad (9.16)$$

In the above equation, for simplicity, we swapped the dummy variable t_r for t .

Moreover, it is easy to see that:

$$\frac{\mathbf{n} \times (\mathbf{n} - \boldsymbol{\beta}) \times \dot{\boldsymbol{\beta}}}{(1 - \boldsymbol{\beta} \cdot \mathbf{n})^2} = \frac{d}{dt} \left[\frac{\mathbf{n} \times (\mathbf{n} \times \boldsymbol{\beta})}{1 - \boldsymbol{\beta} \cdot \mathbf{n}} \right] \quad (9.17)$$

Therefore,

$$\boxed{\frac{d^2 I}{d\omega d\Omega} = \frac{e^2}{4\pi^2 c} \left| \int_{-\infty}^{\infty} e^{i\omega(t - \mathbf{n} \cdot \mathbf{r}/c)} \frac{d}{dt} \left[\frac{\mathbf{n} \times (\mathbf{n} \times \boldsymbol{\beta})}{1 - \boldsymbol{\beta} \cdot \mathbf{n}} \right] dt \right|^2} \quad (9.18)$$

9.3 Bremsstrahlung in Coulomb Collisions

As discussed in section 9.2, for a charged particle, such as an electron, to emit radiation, it needs

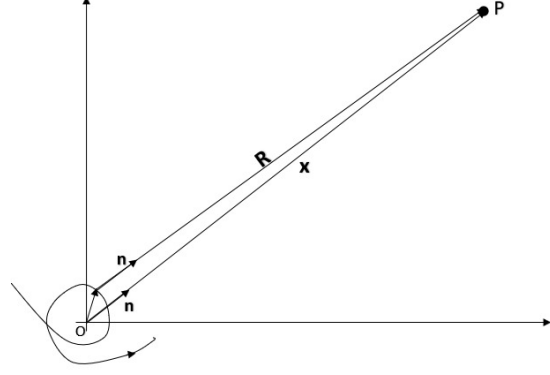


Figure 9.4: Diagram with the vectors of interest.

to be accelerated. This acceleration can occur, for example, in the case of scattering by an atomic nucleus due to the Coulomb potential, as illustrated in Figure 9.7.

Considering a particle with charge ze^1 scattered by a nucleus with charge Ze , the differential cross-section, in cgs units, are related to the scattering angle θ by:

$$\frac{d\sigma}{d\Omega} = \left(\frac{2zZe^2}{pv} \right)^2 \frac{1}{(2 \sin(\theta/2))^4} \quad (9.19)$$

Furthermore, the momentum transfer $Q \equiv |\mathbf{p}' - \mathbf{p}|$ is given by:

$$Q^2 = 2p^2(1 - \cos \theta) = 4p^2 \sin^2 \frac{\theta}{2} \quad (9.20)$$

To obtain the Bremsstrahlung cross-section, it is interesting to make some simplifications in Equation 9.18. First, let's consider the **low-frequency limit** where $\omega \rightarrow 0$. Doing so, the complex exponential in Equation 9.18 tends toward 1, and we obtain:

$$\lim_{\omega \rightarrow 0} \frac{d^2 I}{d\omega d\Omega} = \frac{z^2 e^2}{4\pi^2 c} \left| \frac{\mathbf{n} \times (\mathbf{n} \times \boldsymbol{\beta}')}{1 - \mathbf{n} \cdot \boldsymbol{\beta}'} - \frac{\mathbf{n} \times (\mathbf{n} \times \boldsymbol{\beta})}{1 - \mathbf{n} \cdot \boldsymbol{\beta}} \right|^2 \quad (9.21)$$

where $c\boldsymbol{\beta}'$ and $c\boldsymbol{\beta}$ are the final and initial velocities of the particle, respectively.

Now, we are interested in the **non-relativistic limit**, where $\beta \ll 1$, allowing us to approximate $1 - \mathbf{n} \cdot \boldsymbol{\beta} \approx 1$ in the denominator of Equation 9.21:

$$\lim_{\omega \rightarrow 0} \frac{d^2 I}{d\omega d\Omega} = \frac{z^2 e^2}{4\pi^2 c} \left| \mathbf{n} \times (\mathbf{n} \times \boldsymbol{\beta}') - \mathbf{n} \times (\mathbf{n} \times \boldsymbol{\beta}) \right|^2 \quad (9.22)$$

¹In this case, it is sufficient to replace e from the results of the previous section with ze .

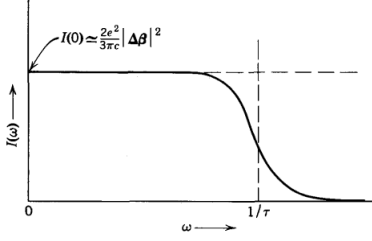


Figure 9.5: Frequency Spectrum of radiation emitted in a collision of duration τ with velocity change $\Delta\beta$ [2].

Rearranging the expression above, we get:

$$\lim_{\omega \rightarrow 0} \frac{d^2 I}{d\omega d\Omega} = \frac{z^2 e^2}{4\pi^2 c} \left\{ |\Delta\beta|^2 - (\mathbf{n} \cdot \Delta\beta)^2 \right\} \quad (9.23)$$

where $\Delta\beta \equiv \beta' - \beta$.

Since $\mathbf{n} = \sin\theta \cos\phi \hat{x} + \sin\theta \sin\phi \hat{y} + \cos\theta \hat{z}$, integrating with respect to the solid angle yields:

$$\lim_{\omega \rightarrow 0} \frac{dI}{d\omega} = \frac{2z^2 e^2 |\Delta\beta|^2}{3\pi c} \quad (9.24)$$

In the **high-frequency limit** as $\omega \rightarrow \infty$, the complex exponential in Equation 9.18 oscillates very rapidly, making the result very small (close to zero), and the radiated energy is negligible (Figure 9.5). Therefore,

$$\frac{dI}{d\omega} = \begin{cases} \frac{2z^2 e^2 |\Delta\beta|^2}{3\pi c}, & \text{Low frequencies} \\ 0, & \text{High frequencies} \end{cases} \quad (9.25)$$

At this point, it is interesting to introduce the differential radiation cross-section given by:

$$\boxed{\frac{d^2 \chi}{d\omega dQ} = \frac{dI}{d\omega} \frac{d\sigma}{dQ}} \quad (9.26)$$

Using Equation 9.19, Equation 9.20, the fact that $d\Omega = \sin\theta d\phi d\theta = Q d\phi dQ/p^2$, and integrating with respect to the azimuthal angle $d\phi$, we have:

$$\frac{d\sigma}{dQ} = 8\pi \left(\frac{zZe^2}{\beta c} \right) \frac{1}{Q^3} \quad (9.27)$$

Therefore, from Equation 9.24 and Equation 9.27, we obtain:

$$\frac{d^2 \chi}{d\omega dQ} = \frac{16}{3} \frac{Z^2 e^2}{c} \left(\frac{z^2 e^2}{mc^2} \right)^2 \frac{1}{\beta} \frac{1}{Q} \quad (9.28)$$

Integrating over dQ , we arrive at:

$$\frac{d\chi}{d\omega} = \frac{16}{3} \frac{Z^2 e^2}{c} \left(\frac{z^2 e^2}{mc^2} \right)^2 \frac{1}{\beta^2} \ln \left(\frac{Q_{\max}}{Q_{\min}} \right) \quad (9.29)$$

Now, introducing a semi-classical argument that takes into account the quantization of electromagnetic energy to include the photon, we should have:

$$E = E' + \hbar\omega \quad (9.30)$$

where $E = p/2m$ and $E' = p'/2m$ are the energies of the incident particle before and after the collision.

Thus, from the definition of momentum transfer and Equation 9.30, we should have:

$$\frac{Q_{\max}}{Q_{\min}} = \frac{p + p'}{p - p'} = \frac{(\sqrt{E} - \sqrt{E - \hbar\omega})^2}{\hbar\omega} \quad (9.31)$$

Finally, inserting Equation 9.31 into Equation 9.29, we obtain:

$$\frac{d\chi_{sc}}{d\omega} = \frac{16}{3} \frac{Z^2 e^2}{c} \left(\frac{z^2 e^2}{mc^2} \right)^2 \frac{1}{\beta^2} \ln \left[\frac{(\sqrt{E} - \sqrt{E - \hbar\omega})^2}{\hbar\omega} \right] \quad (9.32)$$

where the subscript *sc* serves to remind us that this expression was obtained through semi-classical arguments.

The result in Equation 9.32 is precisely the result obtained by quantum mechanics in the Born approximation, first derived by Bethe and Heitler in 1934. Moreover, the argument of the logarithm in Equation 9.32 equals unity when $\hbar\omega = E$, ensuring the conservation of energy requirement is properly satisfied.

It is interesting to note that the radiation cross-section depends on properties of the particles involved in the collision, such as $Z^2 z^4/m^2$, showing that radiation emission is more significant for electrons in materials with a high atomic number. In fact, a proton ($m_p = 1.007u$) of the same energy and incident on the same material will produce less bremsstrahlung than an electron ($m_e = 0.0005485u$) by a factor of:

$$m_p^2/m_e^2 = 1.007^2/0.0005485^2 = 3.37 \times 10^6 \quad (9.33)$$

9.4 X-rays

The phenomenon of electron scattering can be utilized for the production of X-rays, as we will discuss in this section.

9.4.1 Generation of X-rays

X-rays are generated in a low-pressure tube that contains a filament (cathode) and a metal target

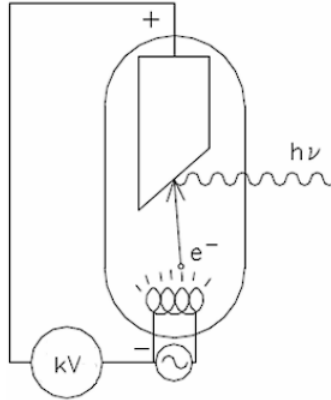


Figure 9.6: X-ray tube illustration

(anode). By heating the filament with a current passing through it, electrons are emitted. These electrons are accelerated by the potential difference V between the cathode and the anode, as illustrated in Figure 9.6. When they strike the anode, these electrons emit Bremsstrahlung radiation, whose spectrum is displayed in Figure 9.2.

9.4.2 X-ray Spectrum

Continuous Spectrum (Bremsstrahlung)

Classically, the continuous spectrum in Figure 9.2 should asymptotically approach zero as the frequency ν of the emitted photon tends to infinity. However, in practice, a maximum cutoff frequency, ν_{\max} , is observed (as described by Equation 9.32). This cutoff frequency corresponds to the situation where all the kinetic energy of the electron is converted into photon energy. Classical electromagnetic theory, however, does not account for this phenomenon, leading to incorrect predictions of the X-ray spectrum.

Thus, let E be the kinetic energy of the incident electron; then we should have:

$$E = h\nu_{\max} \Rightarrow \nu_{\max} = \frac{eV}{h} \quad (9.34)$$

The Equation 9.34, which relates the potential difference to the maximum frequency of the emitted photon, is called the Duane-Hunt Law.

In this context, Bremsstrahlung radiation can be considered the inverse of the photoelectric effect. In the photoelectric effect, radiation is used to eject an electron, while in Bremsstrahlung, electrons are used to emit a photon.

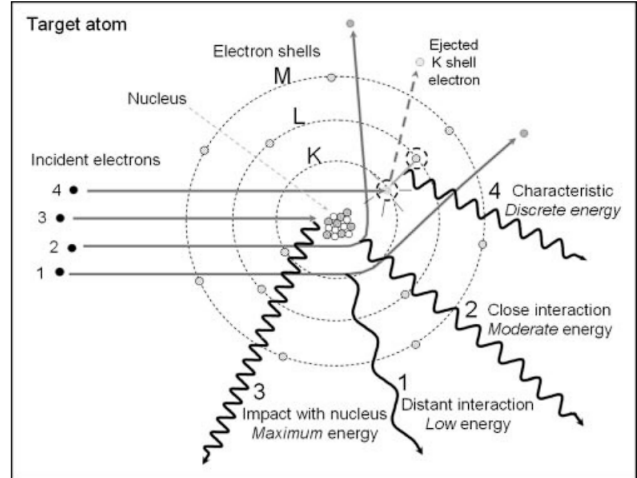


Figure 9.7: Interaction of the incident electron with the atom [5]

Characteristic or Discrete Spectrum

Additionally, as we can see in Figure 9.2, besides the Bremsstrahlung spectrum (continuous), the X-ray spectrum has characteristic lines specific to the anode material.

These characteristic lines of the anode material occur when the incident electron ejects an electron from an inner atomic shell (Figure 9.7). Thus, an outer electron will occupy the ejected electron's shell, emitting a photon of light.

9.5 Bremsstrahlung in Nuclear Decay

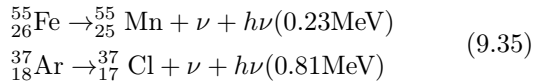
Bremsstrahlung radiation emission also occurs during the transformation of the nucleus in the beta decay process or in electron capture. That is, a continuous spectrum of X-rays originates within an atom undergoing transformation and can be attributed to the sudden change in nuclear charge when a beta particle is emitted or when an orbital electron is captured.

In this case, it is called inner or internal Bremsstrahlung, because it originates from the nucleus, the inner part of the atom, as opposed to external bremsstrahlung, which occurs when a particle from the outside approaches the nucleus and is deflected by it (section 9.3).

In the case of beta decay, emission occurs due to the acceleration that the beta particle undergoes to leave the nucleus shortly after its "birth".

In the electron capture decay process, the quan-

tum of energy not carried away by the neutrino is emitted as internal bremsstrahlung. Thus, in electron capture decay, internal bremsstrahlung may possess energies between zero and the maximum, or transition energy of a radionuclide. The upper limit of the internal bremsstrahlung can be used to determine the transition energy of a nuclide in electron capture decay. Some examples of radionuclides that decay by electron capture are as follows:



9.6 Conclusion

Apart from the interest in the nature of the process itself, bremsstrahlung appears in various fields of physics: atomic and nuclear physics, solid-state physics, particle physics, astrophysics, and so on. Moreover, it is an important tool in many areas of experimental research, with a wide range of technical applications.

The bremsstrahlung process is generally considered to be well understood. However, the comparisons between experiment and theory have for the most part been made for cases where only the emitted photons are considered, disregarding the accelerated outgoing particles. Thus the results are necessarily integrated over all particles scattering angles, whereby important features are lost and the check of the theory is not as strong as it could be. When, on the other hand, the bremsstrahlung photons are detected in coincidence with the accelerated particles scattered into a fixed direction, information on the elementary process of bremsstrahlung can be obtained and a more stringent check of the theoretical work becomes possible.

Bibliografia

- [1] On a New Kind of Rays. *Nature* 53, 274–276 (1896). <https://doi.org/10.1038/053274b0>
- [2] Jackson, John David, 1925-2016. (1999). *Classical electrodynamics*. New York :Wiley,
- [3] Nakel, W. (2004). *The Elementary Process of Bremsstrahlung*.
- [4] Griffiths, David J. (David Jeffery), 1942-. (2013). *Introduction to electrodynamics*. Boston :Pearson,
- [5] Seibert J. A. (2004). X-ray imaging physics for nuclear medicine technologists. Part 1: Basic principles of x-ray production. *Journal of nuclear medicine technology*, 32(3), 139–147.
- [6] L’Annunziata, M. Chapter 8 - Electromagnetic Radiation: Photons. *Radioactivity (Second Edition)*. pp. 269-302 (2016),

10

Cherenkov radiation

Vinicius dos Santos Malafatti

Instituto de Física de São Carlos, Universidade de São Paulo, 13560-970 São Carlos, SP, Brazil

Abstract: Cherenkov Radiation was detected first by the Russian physicist Pavel Cherenkov. It's a radiation emitted by a particle that moves through a medium with its velocity higher than the speed of light in this medium and emits a blue light. Some of these effect it's visible in nuclear reactors. This radiation it have been useful to understand some mysteries in the field of astrophysics, using in detectors to help scientist to discover the origin of cosmic rays. Here, it will be show a brief historical context, a mathematical description, and some applications of these wonderful phenomenon.

10.1 Introduction

Let's begin with some historical facts about it. First, in 1900, Marie and Pierre Curie saw these effect in their experiments with radium, but it was first detected experimentally by the russian physicist Pavel Cherenkov [1], who was under the supervision of Sergei Vavilov, in 1934, he noticed a very weak visible radiation from a pure liquids under the influence of γ -rays. But a theory was developed just in 1937 for two physicist Igor Tamm and Ilya Frank, who shared the 1958 Nobel prize for their discovery. Cherenkov discover two other features by which the effect, the light has a unique polarization and directional properties. Since 1945, there have been great strides in the field. The creation of photomultiplier, the most sensitive detector known for the study of faint pulses of light, has been largely responsible for the more recent developments. At the same time the advent of nuclear physics with the construction of the nuclear reactors all over the world, producing high energies particles that could be produce Cherenkov radiation, the creation of detectors with Cherenkov radiation, enabling to distinguish between different types of particles and to measure directly their velocities[2], when these particles for

example strikes the atmosphere and the telescopes detect the Cherenkov light produced by the shower or their interaction with some water tanks in the ground.

10.2 Theory

When a charged particle moves at a uniform velocity in a dielectric medium, the associated electromagnetic field close to the particle polarizes the medium along its track, so that the electrons attached to the atoms follow the wave-form of the pulse as the particle goes by. It can be compare when a jet breaks the sound barrier (See Figure 10.1). It's important to mention that in this pro-

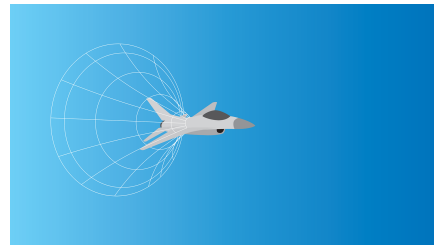


Figure 10.1: Jet breaks the sound barrier [6]

cess the atoms are not excited by the electron and neither are the removed from their bound states, there is not ionization. There is a fundamental relation between the velocity of the particle, and the refractive index of the current medium, and the angle at which the light is emitted. This is know as the Cherenkov relation [3]:

$$\cos \theta_c = \frac{1}{\beta_n} \quad (10.1)$$

where $\beta_n = vn/c$, e n is the refraction index of the medium. It can be seen in the Figure 10.2 and

in the Figure 10.3 the propagation of a high-energy particle.

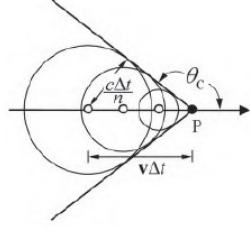


Figure 10.2: Spherical waves emitted at previous positions of the particle (small open circles) [3]

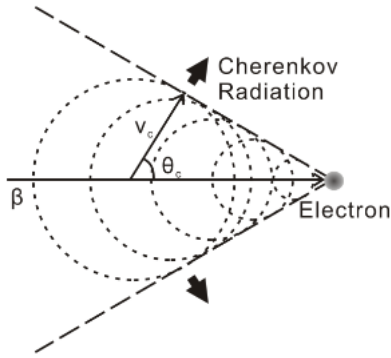


Figure 10.3: A schematic of Cherenkov Radiation [7]

For example in the water, where the index is $n = 1.33$, the Cherenkov relation maximum (10.1) will be $\theta = 41^\circ$ and the velocity to emit Cherenkov radiation will be $v = 2.3 \times 10^8 m/s$. So, the velocity is close to the speed of light, it's important to use special relativity, to obtain the velocity of the particle. Begin, with the momentum conservation as in [10]

$$P^2 = P_0^2 + P_c^2 - 2P_0P_c \cos \theta_c \quad (10.2)$$

Now, using the energy conservation,

$$(P_0^2 c^2 + m_0^2 c^4)^{1/2} = (P^2 c^2 + m_0^2 c^4) + h\nu \quad (10.3)$$

where the where $v = c/(n\lambda)$. Solving for the $\cos \theta_c$ we find that

$$\cos \theta_c = \frac{(P_c^2 + m_0^2 c^4)^{1/2} + (n^2 - 1)h\nu}{2P_0 c n} \quad (10.4)$$

now, with the (10.1) it's possible to find the velocity of the particle

$$v = \frac{P_0 c^2}{(P_c^2 + m_0^2 c^4)^{1/2}} \quad (10.5)$$

So, with these results the scientists are able to find the velocity of the relativistics particles, passing through the water for example, and this will be useful to the fields of particle physics and astrophysics to detect them.

10.2.1 Potentials and conditions for the emission

Now, let's find the potentials following the [3] and [11]. Using the Liénard-Wiechert potentials, it will find an appropriate to potentials for the Cherenkov radiation:

$$\phi(\mathbf{r}, t) = \frac{1}{4\pi\epsilon} \left[\frac{q}{R - \beta_n \cdot \mathbf{R}} \right]_{ret} \quad (10.6)$$

and for potential vector

$$\mathbf{A}(\mathbf{r}, t) = \frac{\mu}{4\pi} \left[\frac{qv}{R - \beta_n \cdot \mathbf{R}} \right]_{ret} \quad (10.7)$$

The interesting feature of these equations is that the equation which determines the retarded time, which it's

$$t_{ret} - t = \frac{R(t_{ret})}{c_n} \quad (10.8)$$

and it will have two solutions, one will be inside the Mach cone and no solutions when it lies outside the cone. See the showing an observer inside the Mach cone of a charge moving at constant velocity. The moving charge enters the volume enclosed by the shell. Noting that in Figure 10.4 the square of $R_{ret} = |\mathbf{R} + v(t - t_{ret})\mathbf{i}|$ is a quadratic equation for $t - t_{ret}$ with the following solutions

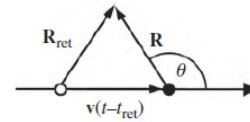


Figure 10.4: The present time position and retarded time position of a charge moving with constant velocity [3]

$$t - t_{ret} = \frac{-\mathbf{v} \cdot \mathbf{R} \pm \sqrt{(\mathbf{v} \cdot \mathbf{R})^2 - (v^2 - c_n^2)R^2}}{v^2 - c_n^2} \geq 0 \quad (10.9)$$

So, if $v > c_n$, the positivity condition on the right side of the (10.9) imposes two conditions, the first is:

$$\mathbf{v} \cdot \mathbf{R} < 0 \quad (10.10)$$

and

$$(\mathbf{v} \cdot \mathbf{R})^2 > (v^2 - c_n^2)R^2 \quad (10.11)$$

By Cherenkov relation, the left and right sides of the two conditions, imply that solutions to (10.9) exist if

$$\begin{aligned} \theta &> \frac{\pi}{2} \\ \sin \theta &\leq \sin \theta_c = \frac{1}{\beta_n} \end{aligned} \quad (10.12)$$

The conditions in (10.12) define the volume inside the Mach cone.

So, there will be no fields in front of the particle, so the potentials will exist only inside the Cherenkov's cone, the values of $(R - \beta_n \cdot \mathbf{R})$

$$R - \beta_n \cdot \mathbf{R} = \mp \frac{1}{c_n} [(\mathbf{R} \cdot \mathbf{v})^2 - (v^2 - c^2)R^2]^{1/2} \quad (10.13)$$

The potentials are only useful inside the Cherenkov cone, in cone edge there will be a singularity and outside they don't exist.

10.2.2 Radiated Energy

Using the Maxwell's equations:

$$\begin{aligned} \mathbf{E} &= -\nabla\phi - \frac{\partial \mathbf{A}}{\partial t} \\ \mathbf{B} &= \nabla \times \mathbf{A} \end{aligned} \quad (10.14)$$

and the potentials (10.6), (10.7), the electric field and the magnetic field can be computed. In most cases is interesting to find the radiation spectral, for that is convenient to use the fourier transformation and find $E(\omega)$ from $E(t)$. The energy that is radiated for unity of area and frequency can be obtained in the reference [3] and [11]:

$$\frac{d^2 U_{rad}}{d\omega dA} = \frac{ec_n}{\pi} |E(\omega)|^2 \quad (10.15)$$

After some calculations following the reference [3], it's find a final result,

$$\frac{d^2 U_{rad}}{d\omega dA} = \frac{\mu q^2}{4\pi} \left(1 - \frac{c^2}{v^2 n^2}\right) \omega \quad (10.16)$$

As from the equation (10.16), the Cherenkov radiation appears blue to the naked eye because is an increasing function of frequency, i.e the Cherenkov light is blue because n does not vary much in the visible part of the spectrum, on the other hand, there

will be *no* Cherenkov emission at frequencies beyond the near-ultraviolet because $n < 1$ there and it is not possible to satisfy the Cherenkov relation with a real angle, and that is confirmed through experiment. In Figure 10.5, it can be seen a continuous spectrum of the Cherenkov radiation,

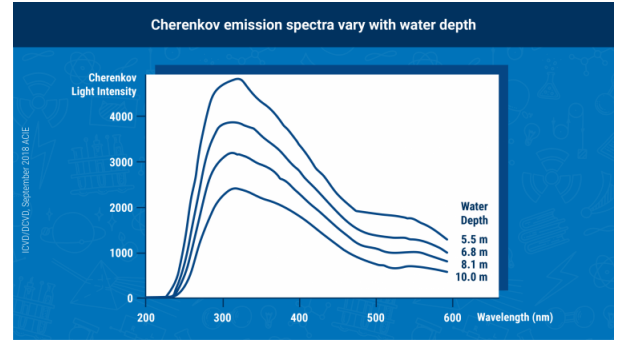


Figure 10.5: Continuous spectrum, and most of the light is produced predominantly in the blue, violet, and ultraviolet region of the electromagnetic spectrum [9]

10.3 Applications

Some applications to the Cherenkov radiation could be in:

- **Nuclear Reactors:** The Cherenkov radiation is used to detect high-energy particles charged, for example when a reactor pool is opened the scientist can identify the beta particles, and characterize the remaining radioactivity of spent fuel rods, this phenomenon helps to verify how much the fuel remains in the reactor for nuclear safety [4]. In Figure 10.7 it's shown the effect of Cherenkov radiation in a nuclear reactor, it's easy to see a blue light.
- **Astrophysics Experiments:** When a high-energy particles come from the some astrophysical source, they interact with the Earth's atmosphere and produce and shower of particles, some of them are electron-positron pair with relativistic velocities in Figure 10.6 . The Cherenkov radiation emitted in the atmosphere by these particles is used to find the direction and the energy of the cosmic ray or the gamma ray produced in the source, by experiments such as VERITAS, H.E.S.S, MAGIC, Cherenkov Telescope Array(CTA) that you will be discuss in the next section, some of them as Pierre Auger observatory is in the ground

where the particles interact with water in tanks on the ground and produce Cherenkov light, water Cherenkov detectors scattered across 3000 km² on Pampa Amarilla in Argentina have collected high-quality data to allow for precise measurements of UHECR in Figure.

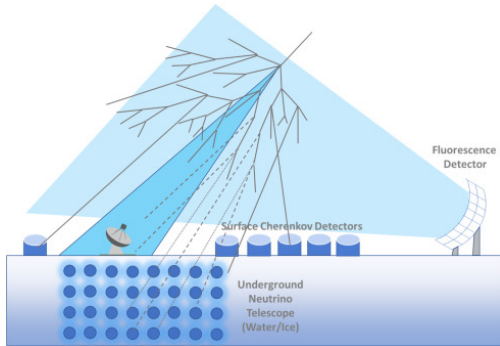


Figure 10.6: An illustration of the applications of Cherenkov light in the detection of high-energy cosmic rays and neutrinos [8]

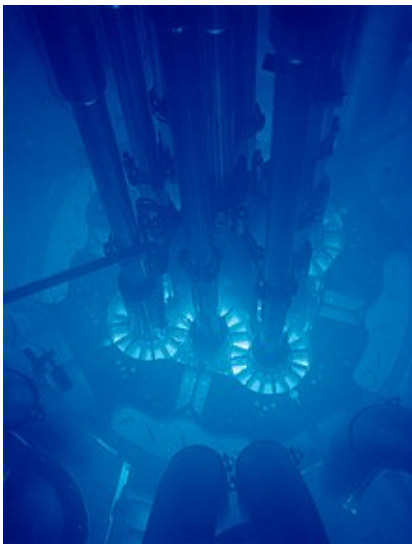


Figure 10.7: Cherenkov radiation glowing in the core of the Advanced Test Reactor at Idaho National Laboratory.[5]

10.3.1 CTAO

It will discuss shortly about the new international collaboration CTA , it will be the largest ground-based gamma-ray observatory and the most advanced. There will be three classes of telescopes Figure 10.8 which will cover the energy range (20

GeV to 300 TeV). So the cameras will detect the flash of light produced by the interaction of these high-energy particles. There will be two array sites, one in the northern hemisphere to see the northern sky and other in the southern hemisphere to see the southern sky. The technology present in the CTAO will use 3500 highly-reflective mirrors facets to focus light into the telescopes cameras that contains photomultiplier tubes and silicon photomultipliers to provide a ultra-fast-light- sensitive pixels [13].



Figure 10.8: Three sizes of CTA telescopes. [13]

10.4 Conclusion

The use of Cherenkov light has played an important role in many areas since the medicals [12] uses until in detectors of high-energy astroparticle physics. Being formulated by using special relativity theory. It supposes that its applications it will continue to be important, for the advance of the physics, and for the new discovers, helping answer some fundamental questions.

Bibliografia

- [1] Cherenkov, P.A. (1934) "Visible emission of clean liquids by action of gamma radiation," *Doklady Akademil Mauk SSE 2: 451*.
- [2] Jelley J. V., 1955, *BJAP*, 6, 227. doi:10.1088/0508-3443/6/7/301
- [3] Zangwill, A. (2012). *Modern Electrodynamics*. Cambridge: Cambridge University Press. doi:10.1017/CBO9781139034777
- [4] Branger, E., Grape, S., Jacobsson, S., Jansson, P., Andersson Sundén, E. (2017) On Cherenkov light production by irradiated nuclear fuel rods *Journal of Instrumentation*,

- 12: T06001 <https://doi.org/10.1088/1748-0221/12/06/T06001>
- [5] <https://en.wikipedia.org/wiki/Cherenkov-radiation>: Accessed 24 Nov.2023
- [6] <https://www.symmetrymagazine.org/article/august-2009/cherenkov-light?language-content-entity=und>
- [7] Sakaue, Kazuyuki et al. Investigation of the Coherent Cherenkov Radiation Using Tilted Electron Bunch.” (2017).
- [8] Lu Lu, Tianlu Yuan, The use of Cherenkov light in the detection of high-energy cosmic rays and neutrinos: The Pierre Auger and IceCube Observatories, Nuclear Instruments and Methods in Physics Research Section A: Accelerators, Spectrometers, Detectors and Associated Equipment, Volume 970, 2020, 163678,ISSN 0168-9002,<https://doi.org/10.1016/j.nima.2020.163678>.
- [9] <https://www.iaea.org/newscenter/news/what-is-cherenkov-radiation>
- [10] <http://large.stanford.edu/courses/2014/ph241/alaecian2/> (An Introduction to Cherenkov Radiation), Accessed 26 Nov.2023
- [11] Courteille Ph. W., Eletrodinâmica - Aulas em Física para pós-graduação, (Instituto de Física de São Carlos-USP, 20123), Capítulo 8.
- [12] Bianfei S, Fang L, Zhongzheng X, Yuanyuan Z, Tian Y, Tao H, Jiachun M, Xiran W, Siting Y, Lei L. Application of Cherenkov radiation in tumor imaging and treatment. *Future Oncol.* 2022 Sep;18(27):3101-3118. doi: 10.2217/fon-2022-0022. Epub 2022 Sep 6. PMID: 36065976.
- [13] <https://www.cta-observatory.org/science/ctao-performance/>

Kerr Effect

Vinicius Pereira Pinto

Instituto de Física de São Carlos, Universidade de São Paulo, 13560-970 São Carlos, SP, Brazil

Abstract: The Kerr Effect, uncovered by John Kerr in the late 19th century, manifests as induced birefringence and a modification of the local refractive index in a material under the influence of an electric field. This discovery led to the exploration of two distinct phenomena: the Magneto-optic Kerr Effect (MOKE) and the Optical Kerr Effect, the latter being the focus of this study. This work provides an overview of the historical development of the theory, offers a comprehensive theoretical treatment, and introduces various experimental techniques for characterizing this interaction in materials. Additionally, practical applications of this phenomenon are discussed, highlighting its potential technological implications.

11.1 Introduction

In the history of optical science, fundamental questions emerged, centered around the nature of light and the comprehension and manipulation of its interaction with matter. One of the most crucial domains of optics focuses on studying the propagation of light in matter, especially in condensed matter, offering vast possibilities for applications through precise control of this phenomenon. Initially, it is essential to understand how electrically charged particles or macroscopic clusters of these particles interact with light, examining influential characteristics such as absorption, dispersion, refraction, and polarization. The advent of Maxwell's electromagnetic theory represented a significant milestone, enabling the description of light interactions based on the macroscopic properties of materials.

In the 19th century, Michael Faraday devoted himself to studying the propagation of polarized light in isotropic dielectric media under magnetic fields. In his 1845 article [1], Faraday observed the rotation of the polarization plane along the propa-

gation of the medium, a phenomenon known as *optical activity*. Thirty years later, inspired by Faraday's insights, John Kerr undertook investigations to understand the behavior of light propagation in transparent and optically isotropic media when subjected to intense electrostatic forces, aiming to nullify the isotropy of solid [2] and liquid [3] media under the influence of light. Kerr succeeded in conducting these experiments on dielectric solids and liquids, which Faraday had failed to replicate in his tests with electrolytes and dielectrics. This effect came to be known as the *Kerr Electro-optic Effect*.

The Kerr Electro-optic Effect induces changes in the local refractive index in a medium, altered by electronic, thermal, and molecular orientation interactions under the influence of an electromagnetic field along the propagation of light, resulting in the induction of local birefringence in the material. The effect was observed by applying an electric field generated by a direct current (DC) voltage source, known as the *DC Kerr Effect*. In 1956, Buckingham [4] became the first to adapt this effect to alternating current (AC) sources and proposed using the electric field of light to induce the Kerr effect, known as the *AC Kerr Effect*. Thirteen years later, with the advent of pulsed lasers, Duguay and Hansen were able to observe the Kerr Effect produced by the electromagnetic field of the incident light itself using picosecond pulses from a mode-locked glass laser in 1969 [5], as this type of laser technology already provided high intensities. The temporal and spatial variation of the medium's refractive index caused by the light itself led to nonlinear optical effects such as self-focusing (Kerr lens) [6], self-phase modulation [7], modulational instability [8], supercontinuum generation [9], and four-wave mixing [10].

11.2 Third-order nonlinear processes

To study the processes occurring during the propagation of light through a material, it is necessary to employ Maxwell's electromagnetic theory. For simple materials, the response of bound charges to the electric field can be described by a dielectric polarization density, denoted as \mathbf{P} , which is linearly dependent on the electric field, denoted as \mathbf{E} , through the expression: $\mathbf{P} = \chi \varepsilon_0 \mathbf{E}$, where χ represents the electric susceptibility, and ε_0 is the vacuum electrical permittivity. For isotropic media, χ is a scalar quantity, preserving the same value for any direction of \mathbf{E} . For nonisotropic media, χ is expressed as a tensor, and the polarization dependence can be expressible as:

$$\begin{bmatrix} P_x \\ P_y \\ P_z \end{bmatrix} = \varepsilon_0 \begin{bmatrix} \chi_{11} & \chi_{12} & \chi_{13} \\ \chi_{21} & \chi_{22} & \chi_{23} \\ \chi_{31} & \chi_{32} & \chi_{33} \end{bmatrix} \begin{bmatrix} E_x \\ E_y \\ E_z \end{bmatrix}. \quad (11.1)$$

For complex materials, the polarization exhibits a nonlinear dependence on the electric field. Consequently, the polarization expression can be characterized through a Taylor series expansion:

$$\mathbf{P} = \varepsilon_0 \chi^{(1)} \mathbf{E} + \varepsilon_0 \chi^{(2)} \mathbf{E}\mathbf{E} + \varepsilon_0 \chi^{(3)} \mathbf{E}\mathbf{E}\mathbf{E} + \dots, \quad (11.2)$$

where the coefficients $\chi^{(n)}$ signify the n -th-order susceptibilities inherent to the material, encapsulating not only the polarization-dependent characteristics of the parametric interaction but also reflects the symmetries or their absence inherent in the material. The first term is the linear dependence, and the incorporation of the other terms is frequently referred to as introducing n -th-order nonlinearity.

Expanding the (11.2), the i -th component of the polarization will be:

$$\begin{aligned} \hat{P}_i = & \varepsilon_0 \sum_{j=1}^3 \chi_{ij}^{(1)} \hat{E}_j + \varepsilon_0 \sum_{j=1}^3 \sum_{k=1}^3 \chi_{ijk}^{(2)} \hat{E}_j \hat{E}_k \\ & + \varepsilon_0 \sum_{j=1}^3 \sum_{k=1}^3 \sum_{l=1}^3 \chi_{ijkl}^{(3)} \hat{E}_j \hat{E}_k \hat{E}_l + \dots, \end{aligned} \quad (11.3)$$

with $(i, j, k, l = x, y, z)$. To investigate third-order nonlinear processes, the analysis will be specifically focused on the third term.

11.2.1 Symmetry effects

From the (11.3), the most general susceptibility, for process involving the interaction of waves

of four linked different frequencies, has the form $\chi_{ijkl} \equiv \chi_{ijkl}^{(3)}(\omega_4 = \omega_1 + \omega_2 + \omega_3)$ it is possible to realize the potential to $3^4 = 81$ separate nonlinear coefficients, since i, j, k, l can each be x, y or z for a lossless medium of the most general triclinic symmetry. For structurally isotropic medium, with no intrinsic axes, only 21 coefficients are non-zero: when all indices are identical, $\chi_1 \equiv \chi_{iiii}$, and when two pairs of indices are the same, namely $\chi_2 \equiv \chi_{jjkk}$, $\chi_3 \equiv \chi_{jkjk}$ and $\chi_4 \equiv \chi_{jkkj}$ with $j \neq k$. This symmetry imposes the further constraint that:

$$\chi_1 = \chi_2 + \chi_3 + \chi_4, \quad (11.4)$$

resulting in the 21 non-zero coefficients [11]:

- 1: $xxxx = yyyy = zzzz$,
 - 2: $xyxy = yzyz = zxxz = yxyx = zzyy = xxzz$,
 - 3: $xyxy = yzyz = zxxz = yxyx = zzyy = xxzz$,
 - 4: $xyyx = yzzx = zxxz = yxyx = zyyz = xxzz$.
- (11.5)

Furthermore, for collinear beams, selecting one axis along the direction of beam propagation allows the reduction of non-zero coefficients to 8 by disregarding those associated with the chosen axis. If all beams are plane-polarized in the same direction, choosing the x-axis as the polarization direction results in the $\chi_1 = \chi_{xxxx}$ coefficient only. Additional insights into medium symmetries can be found in [11].

11.3 The DC Kerr Effect

Examining the DC Kerr Effect caused by a strong DC field that alters the refractive index of a medium, the absence of incident beams leads to frequencies $\omega = 0 + 0 + \omega$, as shown in Fig. 11.1.

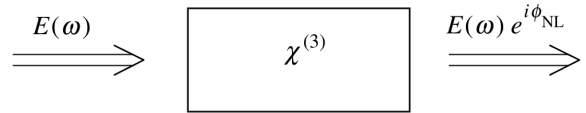


Figure 11.1: A strong DC field modifies a light propagation through a Kerr medium [12].

By selecting a y -polarized field, the coefficients are $\chi_1^K \equiv \chi_{yyyy}^K(\omega; 0, 0, \omega)$ and $\chi_4^K \equiv \chi_{xyyx}^K(\omega; 0, 0, \omega)$, the corresponding polarization responses unfold as follows:

$$\begin{aligned}\hat{P}_x(\omega) &= 3\varepsilon_0\chi_4^K E_y^2(0)\hat{E}_x(\omega), \\ \hat{P}_y(\omega) &= 3\varepsilon_0\chi_1^K E_y^2(0)\hat{E}_x(\omega).\end{aligned}\quad (11.6)$$

This leads to a difference of the refractive index for parallel and perpendicular polarized light, n_{\parallel} and n_{\perp} respectively, given by

$$n_{\parallel} - n_{\perp} \cong \frac{3(\chi_1^K - \chi_4^K)E_y^2(0)}{2n} = \frac{3\chi_2^K E_y^2(0)}{n}, \quad (11.7)$$

where χ_2^K and χ_3^K are identical, indicating that the difference is $\chi_1^K - \chi_4^K = 2\chi_2^K$, as derived from (11.4).

Expressing this difference as

$$\Delta n \equiv n_{\parallel} - n_{\perp} = \lambda_0 K E^2(0), \quad (11.8)$$

where λ_0 represents the vacuum wavelength, defining $K = 3\chi_2^K/(\lambda_0 n)$ as the Kerr constant of the medium.

11.4 The Optical Kerr Effect

Examining the Optical Kerr Effect caused by a strong wave, the presence of a wave at frequency ω_2 and intensity $I(\omega_2)$ leads to a modification in the refractive index of a probe wave at ω_1 , leading to $\omega_1 = \omega_2 - \omega_2 + \omega_1$, as shown in Fig. 11.2.

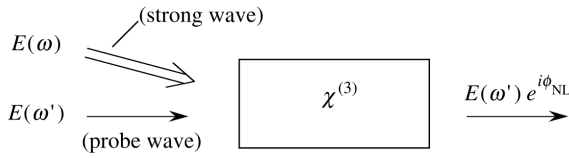


Figure 11.2: A strong beam of light influencing the propagation of a probe beam through a Kerr medium [12].

By selecting the waves with same polarisation, the only coefficient will be $\chi_{xxxx}^{OK} \equiv \chi_{xxxx}^{OK}(\omega_1; \omega_2, -\omega_2, \omega_1)$, and the corresponding polarization responses unfold as follows:

$$\hat{P}_x = \frac{3}{2}\varepsilon_0\chi_{xxxx}^{OK} \left| \hat{E}_x(\omega_2) \right|^2 \hat{E}_x(\omega_1), \quad (11.9)$$

leading to a difference of the refractive index of the probe wave given by

$$\Delta n_x \cong \frac{3\chi_{xxxx}^{OK} I(\omega_2)}{2n(\omega_1)n(\omega_2)c\varepsilon_0}, \quad (11.10)$$

where c is the speed of light in vacuum.

If the strong wave is y -polarized, the only coefficient will be $\chi_{xyyx}^{OK} \equiv \chi_{xyyx}^{OK}(\omega_1; \omega_2, -\omega_2, \omega_1)$, making the refractive index difference weaker.

11.4.1 Intensity-dependent refractive index

When a single beam has an intense intensity $I \equiv I(\omega, r, t)$ and modifies its own refractive index, $\omega = \omega_1 = \omega_2$, there's a self-action effect known as intensity-dependent refractive index. For a plane-polarised light, the polarisation is given by

$$\hat{P}_x(\omega) = \frac{3}{4}\varepsilon_0\chi_1 \left| \hat{E}_x(\omega) \right|^2 \hat{E}_x(\omega), \quad (11.11)$$

implying in a refractive index in the form

$$n(I) = n_0 + \left(\frac{3\chi_1}{4n_0^2 c \varepsilon_0} \right) I = n_0 + n_2 I, \quad (11.12)$$

where n_0 is the linear refractive index for ω and defining n_2 as the nonlinear refractive index.

A more detailed analysis of circularly and elliptically polarized light, encompassing additional coefficients, can be found in references [11, 12].

11.4.2 Refractive nonlinearities types

For the case of isotropic medium under a polarised laser with irradiance I (considered to be the same for linear and circular polarizations), where the frequencies are $\chi_{ijkl}(\omega = \omega + \omega - \omega)$, the nonlinear polarization derived from (11.2) is

$$\mathbf{P} = 6\varepsilon_0\chi_{1122} (\mathbf{E} \cdot \mathbf{E}^*) \mathbf{E} + 3\varepsilon_0\chi_{1221} (\mathbf{E} \cdot \mathbf{E}) \mathbf{E}^*. \quad (11.13)$$

It is possible to introduce the coefficients $A \equiv 6\chi_{xxyy}$ and $B \equiv 6\chi_{xyyx}$. Rewritten the (11.13), the nonlinear polarization is given by

$$\mathbf{P} = \varepsilon_0 A (\mathbf{E} \cdot \mathbf{E}^*) \mathbf{E} + \frac{1}{2}\varepsilon_0 B (\mathbf{E} \cdot \mathbf{E}) \mathbf{E}^*. \quad (11.14)$$

The ratios between these two coefficients is different for each type of nonlinearities processes of the medium: the pure nonresonant electronic ($B/A = 1$), orientational ($B/A = 6$), and thermal ($B/A = 0$). Changing the (11.12) for these coefficients, the change on the refractive index is given by

$$\Delta n_{linear} = \frac{I}{4n_0^2 \varepsilon_0 c} \left(A + \frac{1}{2}B \right), \quad (11.15)$$

for linear polarization, and

$$\Delta n_{circular} = \frac{I}{4n_0^2 \varepsilon_0 c} A, \quad (11.16)$$

for circular polarization. The ratios between $\Delta n_{linear}/\Delta n_{circular} = 1 + B/(2A) = 3/2, 4$ and 1 for pure electronic, molecular orientational, and thermal nonlinearities, respectively [12].

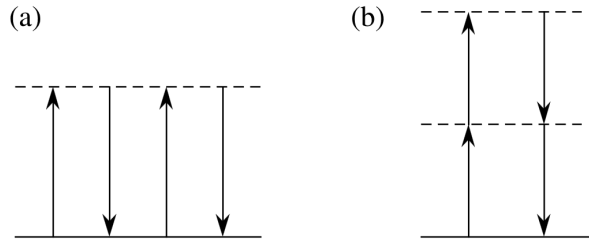


Figure 11.3: Diagrams of (a) a one-photon-resonant contribution by A , and (b) two-photon-resonant processes involving both coefficients A and B [12].

The distinct physical characteristics of the contributions from the two coefficients to the nonlinear polarization stem from a one-photon-resonant contribution by A , and two-photon-resonant processes involving both coefficients A and B (under certain conditions, exclusively contributed by B), shown in Fig. 11.3.

11.5 Nonlinear optical characterization

Due to the nonlinear response of light-matter interaction to a strong electric field in certain materials, which influences measurements and enables the exploration of these effects, it becomes imperative to determine the sign and magnitude of n_2 . Different materials has intrinsic characteristics, leading to diverse responses under distinct conditions. This necessitates the application of various techniques to measure their respective nonlinear coefficients.

11.5.1 Nonlinear Interferometry

An technique developed by [13] involves an interferometric method. In this approach, the material under investigation is positioned in one arm of an interferometer, and an intense pulsed laser beam is directed through the sample. This setup enables the measurement of the nonlinear phase change of the beam, providing a means to quantify n_2 from the obtained data. The use of this method for measuring the optical nonlinearity of gases [15] is illustrated in Fig. 11.4. This process induces changes in the refractive index, resulting in both a phase delay and a displacement of the fringe pattern at the interferometer output.

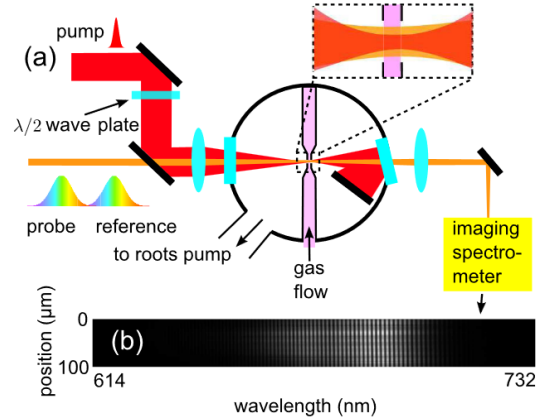


Figure 11.4: (a) Simplified experimental setup diagram of an interferometric n_2 measurement technique and (b) an example interferogram [15].

This method has variations, encompassing both absolute and relative measurements for n_2 [14]. In the case of relative measurements, a known nonlinear sample is introduced into one arm of the interferometer. The most recent variation, developed by [16], is tailored for measurements in the infrared spectral range, as depicted in Fig. 11.5.

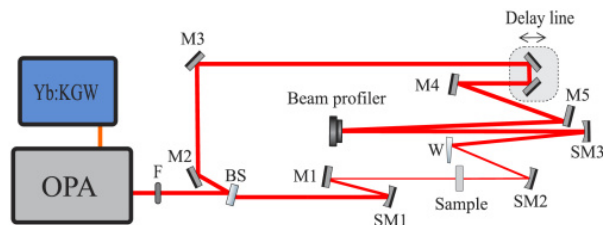


Figure 11.5: Experimental setup diagram of an interferometric n_2 measurement technique in the infrared spectral range [16].

While this approach was widely employed in the initial characterization of n_2 , newer methods have since been developed, yielding superior results and simple apparatus.

11.5.2 Z-scan

The Z-scan technique, developed by [17], has proven to be highly sensitive and features a straightforward experimental setup and analysis, making it particularly effective for measuring n_2 . This method relies on the conversion of phase distortion to amplitude distortion as a pulsed beam propagates through a Kerr medium, applicable over a broad wavelength range and accommodating various types of nonlinearity. To measure amplitude distortion, a

Gaussian laser beam is employed in a tight-focus limiting geometry, and the transmittance $T(z, t)$ of the medium through a finite aperture placed in the far field is recorded as a function of the sample position z , as shown in Fig. 11.6.

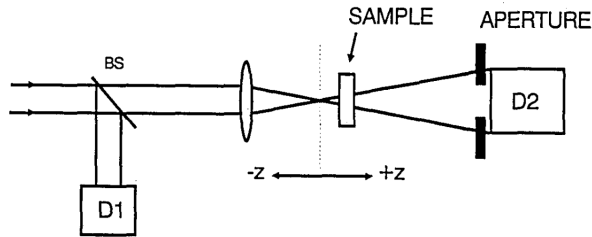


Figure 11.6: Simple Z-scan experimental apparatus [17].

The Fig. 11.7 shows an example of Z-scan measurements of a CS_2 cell. The transmittance distortion curve represents the nonlinear response of the material, where a less flattened curve indicates more intense nonlinearities in the medium. The peak-to-valley configuration of the Z-scan curve signifies either a positive (self-focusing) or negative (self-defocusing) nonlinearity. This is determined by measuring the difference between the normalized peak and valley transmittances, denoted as $\Delta T_{p-v} \equiv T_p - T_v$.

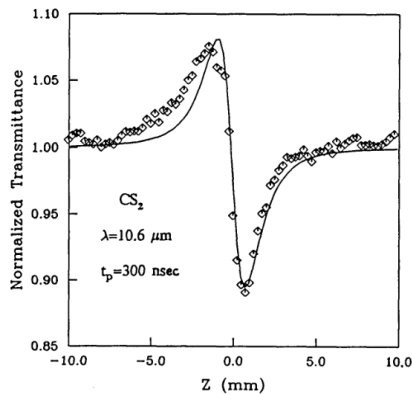


Figure 11.7: Measured Z-scan of a 1-mm-thick CS_2 cell [17].

Presently, this technique stands as the most widely employed method for characterizing n_2 , although it may exhibit some limitations in measuring specific complex media comprehensively. Numerous variations of this technique have been developed, ranging from studies on the dynamics of third-order optical nonlinearities [18] to enhanced sensitivity measurements utilizing Gaussian-Bessel

beams [19]. Additionally, some adaptations aim to mitigate or overlook certain nonlinear effects, such as thermal contributions.

11.5.3 Discrimination of nonlinearities types

A novel variation of the Z-scan method enables the discrimination of thermal, molecular orientation, and pure electronic refractive nonlinearities [20]. This approach involves varying the repetition rate to observe the thermal contribution, with the thermal effect being more pronounced at higher repetition rates of the pulsed laser, as shown in Fig. 11.8. Additionally, by leveraging the distinct dependencies on linear and circular polarization, as detailed in subsection 11.4.2, this method allows for the discrimination of various nonlinear effects, as shown in Fig. 11.9.

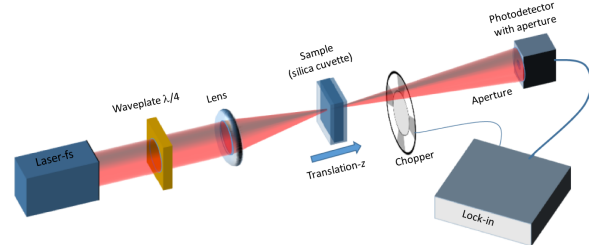


Figure 11.8: Experimental setup diagram of a single-beam polarization-resolved Z-scan [20].

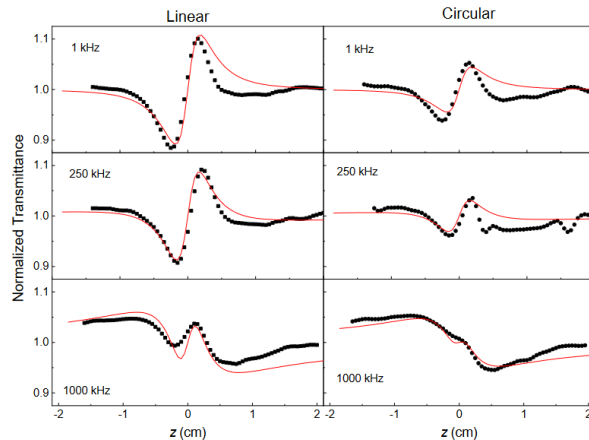


Figure 11.9: Z-scan signals obtained for pure CS_2 with linear (square) and circular (circle) polarization for three laser repetition rates [20].

11.5.4 Other techniques

Several methodologies, extending beyond nonlinear interferometry and z-scan, have been developed to measure third-order nonlinearities in condensed matter. The wave mixing technique employs two or more distinct incident waves to obtain relative measurements of n_2 . Cross-phase modulation (XPM) relies on the phase change in the probe induced by the cross-phase modulation effect with the pump. The nonlinear chirped interferometry technique is based on a frequency-degenerate pump-probe experiment with interferometric detection. The dispersive-scan (D-scan) technique serves as a temporal analog of the top-hat Z-scan. Also several specialized methodologies have been devised to address specific experimental conditions and requirements.

11.6 Kerr Effect application

Following the characterization of nonlinear processes in a Kerr medium, the derived insights can be leveraged to develop new technologies or methodologies. While only two applications are highlighted here, it is noteworthy that numerous other applications exist. Interested readers are encouraged to explore additional applications by referring to the references provided in the introduction.

11.6.1 Kerr-lens Modelocking

Notably, Kerr lensing stands out as a significant application, wherein a short optical pulse propagating through a nonlinear medium induces an optical phase delay that is most prominent along the beam axis, where the optical intensity is highest, and diminishes progressively away from the axis. Utilizing Kerr lensing, the generation of ultrashort pulses through the Kerr-lens Modelocking (KLM) technique has been achieved [21, 22]. The non-uniform intensity distribution in a Gaussian beam induces a local refractive index change, causing the medium to behave as a lens for high-intensity light. In this scenario, the cavity is engineered to be unstable for continuous-wave operation but stable for the pulsed configuration, characterized by a distinct focus. This method ensures that, when the cavity is in the correct configuration, pulsed operation predominates over continuous-wave operation, as depicted in Fig. 11.10.

The exceptionally rapid nonlinear response facilitates the generation of pulses lasting only a few femtoseconds, making it the most effective technique

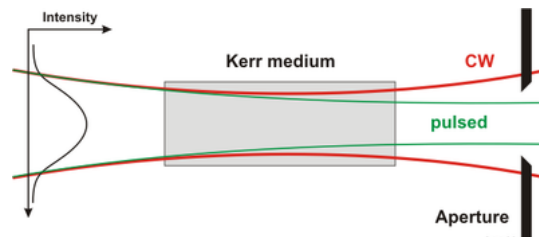


Figure 11.10: Kerr-lens modelocking principle

Commons Wikimedia - CC BY-SA 3.0

for producing ultrashort pulses close to the Fourier-transform limit achievable within the gain medium.

11.6.2 Kerr Effect on Bose–Einstein Condensates

A novel and intriguing exploration of the Kerr Effect delves into Bose–Einstein Condensates (BEC), where the absorption and emission processes within a BEC induce Kerr Effects [23]. In this context, nonlocal optical Kerr nonlinearities with controllable nonlocality were generated through matter-wave superradiance in a Rydberg-dressed BEC, leveraging the strong and long-range interactions between Rydberg atoms. Specifically, for Strontium atoms, a remarkable increase in n_2 by 15 orders of magnitude compared to conventional nonlinear optical materials was achieved, leading to the characterization of this phenomenon as a "Giant nonlocal Kerr nonlinearity" [24].

11.7 Conclusion

Over the span of nearly two centuries since John Kerr first discovered the effect that bears his name, significant advancements have occurred in the theoretical analysis of third-order nonlinear processes. More recently, a plenty of technologies has been developed for the characterization of Kerr media, alongside new methodologies targeting various types of nonlinearities, driven by advancements in pulsed laser technology. Furthermore, the applications stemming from the Kerr effect serve as the foundation for the leading femtosecond lasers used in present times and various other photonics technologies. Despite these remarkable developments, gaps persist in both theoretical understanding and experimental exploration of nonlinear processes. Active research projects are currently underway to address these gaps and contribute to the evolving landscape of nonlinear optics.

Bibliografia

- [1] Faraday, Michael. "On the magnetization of light and the illumination of magnetic lines of force c. 1." *The Royal Society* (1845).
- [2] Kerr, John. "A new relation between electricity and light: Dielectrified media birefringent", *Philosophical Magazine*, **50** (332), p. 337-348 (1875).
- [3] Kerr, John. "A new relation between electricity and light: Dielectrified media birefringent (Second paper)", *Philosophical Magazine*, **50** (333), p. 446-458 (1875).
- [4] Buckingham, A. D. "Theoretical Studies of the Kerr Effect II: The Influence of Pressure", *Proc. Phys. Soc.*, **68** (10), p. 910-919 (1955).
- [5] M. A. Duguay, J. W. Hansen; "AN ULTRA-FAST LIGHT GATE". *Appl. Phys. Lett.*, **15** (6), p. 192-194 (1969).
- [6] Belanger, P. A.; Pare, C. "Self-focusing of Gaussian beams: an alternate derivation", *Appl. Opt.* **22** (9), p. 1293 (1983).
- [7] Alfano, R. R.; Shapiro, S. L. "Observation of self-phase modulation and small-scale filaments in crystals and glasses", *Phys. Rev. Lett.*, **24** (11), p. 592 (1970).
- [8] Shukla, P. K.; Rasmussen, J. Juul. "Modulational instability of short pulses in long optical fibers", *Opt. Lett.* **11** (3), p. 171 (1986).
- [9] Lin, C.; Stolen, R. "New nanosecond continuum for excited-state spectroscopy", *Appl. Phys. Lett.* **28**, p. 216 (1976).
- [10] Stolen, R. H. "Phase-matched-stimulated four-photon mixing in silica-fiber waveguides", *IEEE J. Quantum Electron.* **11** (3), p. 100 (1975).
- [11] New, G. "Introduction to Nonlinear Optics." *Cambridge University Press* (2011).
- [12] Boyd, R. W. *Nonlinear Optics*. Elsevier, Amsterdam, 3rd edition (2007).
- [13] Bliss, E. S., Speck, D. R., Simmons W. W., "Direct interferometric measurements of the nonlinear refractive index coefficient n_2 in laser materials", *Appl. Phys. Lett.*, **25**, 728 (1974).
- [14] Weber, M. J.; Milam, D.; Smith, W. L. "Nonlinear Refractive Index Of Glasses And Crystals." *Optical Engineering* **17** (5), 1978.
- [15] Wahlstrand, J. K., Cheng, Y.-H., Chen, Y.-H., Milchberg, H. M. "Optical Nonlinearity in Ar and N_2 near the Ionization Threshold". *Phys. Rev. Lett.*, **107**(10). (2011).
- [16] Jansonas, G., Budriūnas, R., Vengris, M., Varanavičius, A., "Interferometric measurements of nonlinear refractive index in the infrared spectral range". *Opt. Express* **30**, 30507-30524 (2022).
- [17] Sheik-bahae, M., Said, A. A., Van Stryland, E. W. "High-sensitivity, single-beam n_2 measurements," *Opt. Lett.* **14**, 955-957 (1989).
- [18] Misoguti, L., Mendonça, C. R., Zilio, S. C. "Characterization of dynamic optical nonlinearities with pulse trains." *Appl. Phys. Lett.*, **74** (11), p. 1531-1533 (1999).
- [19] Gao, W., Wang, S., Yuan, J., Wang, L., Xiao, L., Jia, S. "Sensitivity enhancement of nonlinear refractive index measurement by Gaussian-Bessel beam assisted z-scan method." *Opt. Express* **30**, 7291-7298 (2022).
- [20] Moysés, R. M., Barbano, E. C., and Misoguti, L. "Discrimination of thermal, molecular orientation, and pure electronic refractive nonlinearities using the polarization-resolved Z-scan technique," *J. Opt. Soc. Am. B*, **40**, p. C60-C66 (2023).
- [21] D. E. Spence, P. N. Kean, W. Sibbett, "60-fsec pulse generation from a self-mode-locked Ti:sapphire laser", *Opt. Lett.* **16** (1), p. 42 (1991).
- [22] F. Salin et al., "Modelocking of Ti:sapphire lasers and self-focusing: a Gaussian approximation", *Opt. Lett.* **16** (21), p. 1674 (1991).
- [23] Stein, E., Vewinger, F., Pelster, A. "Collective modes of a photon Bose-Einstein condensate with thermo-optic interaction" *New J. Phys.* **21**, 103044 (2019).
- [24] Chen, Y., Bai, Z., Hang, C., Huang, G. "Giant nonlocal Kerr nonlinearity and polaritonic solitons in a Rydberg-dressed Bose-Einstein condensate," *Opt. Express* **31**, 33518-33534 (2023).

12

The Drude model

Willer Frank de Sousa Oliveira

Instituto de Física de São Carlos, Universidade de São Paulo, 13560-970 São Carlos, SP, Brazil

Abstract: Metals play a significant role in our society due to their electrical and thermal conductivity properties. They are widely used in various industries, from electronics to construction. To understand how electricity is conducted in metals, scientists have developed theoretical models, such as the Drude model. This model, proposed in the early 20th century, describes electrons in metals as free particles that move randomly and collide with positive ions. The model is used as a useful simplification in many contexts to describe the electrical conductivity of metals. However, the Drude model has its limitations. The aim of this work is to provide a literature review on the electrical properties of metals based on the Drude model. Through this analysis, we aim to provide a comprehensive resource that can serve as a foundation for future research and an introduction to the study of electrical conduction models.

12.1 Introduction

Paul Karl Ludwig Drude was a German physicist who began his career in the same year that physicist Heinrich Hertz published his experiments on James Clerk Maxwell's electromagnetic theory. In 1900, Drude wrote an important book titled "Lehrbuch der Optik," where he integrated Maxwell's theory with optics. In the same year, he published his theory on the conduction of heat and electricity in metals in the book "Zur Elektronentheorie der Metalle."

Drude's free electron model proposes a classical explanation for metallic conductivity, using Thermodynamics and Newtonian Mechanics to explain the properties of this material. Drude was born in 1863 and took over the Prussian Academy of Sciences in 1906, the same year he inexplicably committed suicide at the peak of his career, leaving behind a wife and four children [2].

Figure 12.1: Paul Karl Ludwig Drude, a German physicist who lived between the years 1863 and 1906.



wiki: Paul Drude (1863 - 1906).

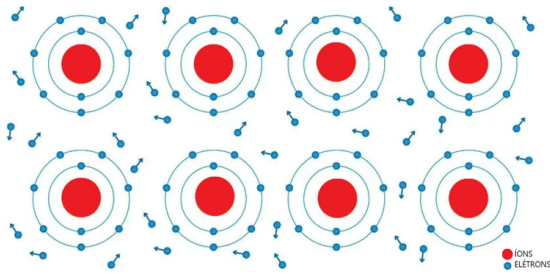
12.2 Basic Assumptions of the Drude Model

In Drude's model of metallic conduction, each atom in the crystalline lattice of a metal contributes one or more electrons from the valence layer, referred to as conduction electrons or free electrons. The Drude atom consists of a nucleus, containing protons and neutrons, and two types of electrons: the so-called nucleus electrons, located in the innermost electronic layers and tightly bound to the nucleus, and the conduction electrons.

The model assumes that during the formation of a metallic structure where atoms come together, valence electrons separate from the nucleus and move freely through the metal, as illustrated in Figure 12.2. The ions, in turn, remain stationary, arranged in a crystalline lattice [3].

In this context, Drude applied the kinetic theory of gases to explain the electrical and thermal con-

Figure 12.2: Free electrons moving through the metal.



Adapted by the author (2023).

duction of metals. The kinetic theory was the first successful microscopic model of matter. This "gas" of electrons can have a volumetric density thousands of times greater than an ideal gas under normal conditions and has at least two types of particles¹, whereas an ideal gas has only one.

To verify this, it is possible to calculate the density (n) of the electron gas, that is, the quantity of free electrons (N) per unit volume (V), in the following way:

$$n = \frac{N}{V} = N_a \frac{Z\rho_m}{A}. \quad (12.1)$$

In this expression, $N_a = 6.02 \times 10^{23} \text{ mol}^{-1}$ is Avogadro's constant, Z is the number of electrons in the valence layer of the metallic atom, ρ_m is the mass density of the metal, and A is the atomic mass of the element [?]. To calculate the density of the electron gas in gold ($1s^2 2s^2 2p^6 3s^2 3p^6 4s^2 3d^{10} 4p^6 5s^2 4d^{10} 5p^6 6s^1 4f^{14} 5d^{10}$), for example, which has $Z = 1$ electron in the valence layer, density $\rho_m = 19.3 \text{ g/cm}^3$, and $A = 197$, the density of the free electron gas in gold is:

$$n_{ouro} = 5,8997 \cdot 10^{22} \text{ cm}^{-3}$$

For comparison purposes, the density of molecules in the air under normal conditions of pressure and temperature (NTP) is on the order of $2.5 \times 10^{19} \text{ cm}^{-3}$, which is roughly a thousand times smaller than the density of free electrons in gold.

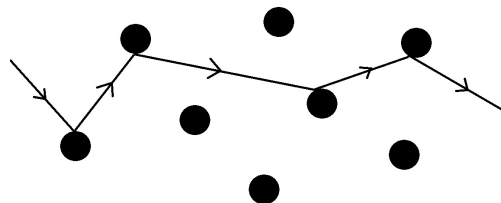
In general, the electronic density of conduction in metallic elements is on the order of 10^{22} electrons per cm^3 under conditions of room temperature and

¹In the kinetic theory of gases, all gas particles are assumed to be spherical, solid, and identical, colliding with each other elastically. In Drude's model, the gas of electrons has two different types of "particles": the fixed ions and the free electrons [4].

atmospheric pressure at sea level. For the model to be consistent, Drude made some basic assumptions:

1. The model considers the approximation of the *free* electron, which neglects electromagnetic interactions between electrons and ions, and the *independent* electron approximation, where the interaction between electrons is neglected. The electron-ion interaction is not completely ignored, as the model assumes that electrons are confined within the metal due to attraction with the ions. The total energy of the system is purely kinetic, and potential energy is disregarded [4]. In the absence of an external electromagnetic field, electrons move randomly in a straight and uniform manner between collisions with the lattice. In the presence of an external field, their trajectory slightly curves, and they must obey Newton's laws of motion. In all cases, additional internal fields are ignored, meaning electrons move independently of each other [1].
2. Collisions are instantaneous events that abruptly change the velocity of electrons. Unlike an ideal gas, only collisions between free electrons and ions are considered, while collisions between gas particles are ignored. However, it is known that in reality, there is a scattering phenomenon among electrons, but the detailed understanding of this phenomenon is not necessary to comprehend metallic conduction both qualitatively and quantitatively [3]. Figure 12.3 provides a simplified representation of Drude's theory. Although incorrect in a strict sense due to the scattering that occurs among electrons in the crystalline lattice, these scatterings do not significantly influence the results obtained by the model.

Figure 12.3: Free electron moving within a crystalline structure and eventually colliding with stationary ions, illustrated by the filled circles.



Adapted by the author (2023).

3. The average time between two consecutive col-

lisions of an electron is called τ , also known as the relaxation time or mean free time. The probability of an electron undergoing a collision in an infinitesimal time dt is dt/τ . This time is used in the Drude model as a phenomenological quantity and depends on various factors, such as the electron density, the density of atoms in the lattice, the sample temperature, and the presence of impurities. In the Drude model, the relaxation time is assumed to be constant, regardless of the position or velocity of the electrons [3].

4. Collisions are responsible for maintaining thermodynamic equilibrium. After each collision, the electron takes on a random direction and velocity that does not depend on the velocity prior to the collision but is directly related to the temperature of the location where the collision occurred [3]. This is the only way electrons can maintain thermal equilibrium with their surroundings when considering the approximations of the free and independent electron [4].

The Drude model postulates that an average charge carrier experiences the influence of a "resistance force", γ . When subjected to an external electric field E , the following differential equation is satisfied:

$$m \frac{d}{dt} \langle \vec{v} \rangle = q \vec{E} - \gamma \langle \vec{v} \rangle$$

Here, $\langle \vec{v} \rangle$ represents the average velocity, m is the effective mass, and q is the electric charge of the charge carrier.

The steady-state solution $\frac{d}{dt} \langle \vec{v} \rangle = 0$ of this differential equation is:

$$\langle \vec{v} \rangle = \frac{q\tau}{m} \vec{E} = \mu \vec{E}$$

where:
 $\tau = \frac{m}{\gamma}$ is the mean free time of a charge carrier, and μ is the electric mobility. Introducing the density of the charge carrier gas n (particles per unit volume), the average velocity can be related to an electric current:

$$\vec{J} = nq \langle \vec{v} \rangle$$

It can be demonstrated that the material adheres to Ohm's law with a DC electrical conductivity σ_0 .

$$\vec{J} = \frac{nq^2\tau}{m} \vec{E} = \sigma_0 \vec{E}$$

The Drude model also enables the prediction of current in response to a time-varying electric field with an angular frequency ω . In this case:

$$\sigma(\omega) = \frac{\sigma_0}{1 + i\omega\tau}$$

It is assumed that:

$$E(t) = \text{Re}(E_0 e^{i\omega t})$$

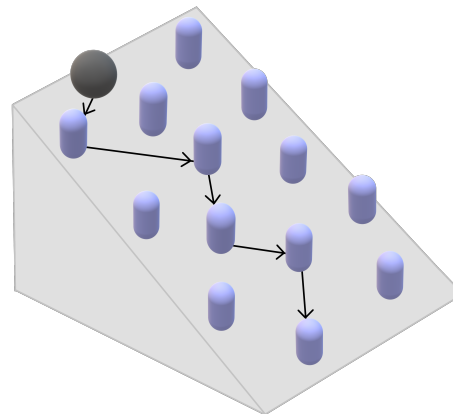
$$J(t) = \text{Re}(\sigma(\omega) E_0 e^{i\omega t})$$

In alternative conventions, i is replaced by $-i$ in all equations. The imaginary part signifies that the current lags behind the electric field because electrons require approximately a time τ to accelerate in response to a change in the applied electric field. While the Drude model was initially applied to electrons, it can also be extended to holes, representing positive charge carriers in semiconductors.

12.3 A Mechanical Analogy for the Drude Model

The motion of electrons in a metallic conductor under the influence of an applied electric field can be analogously compared to the motion of a solid sphere rolling downhill on an inclined plane and changing direction due to collisions with obstacles. The gravitational potential difference between the top and bottom of the slope is equivalent to the electric potential difference in the Drude model, while the obstacles on the plane are analogous to the ions distributed within the conductor.

Figure 12.4: Esfera maciça rolando sobre um plano inclinado e colidindo com obstáculos.



by the author (2023).

Adapted

Just as the sphere is affected by the slope of the plane and collisions with obstacles, electrons are influenced by the electric field and interactions with the conductor's material. This mechanical analogy aids in understanding the behavior of electrons in a metallic conductor according to the Drude free electron model [5].

In a model like this, the sphere lacks an intrinsic vibrational motion (analogous to thermal agitation) that would be responsible for a nonzero net electric current in the electrical context. To induce this agitation in the model, it is possible, as suggested by [5], to couple a vibratory motor to the system.

12.4 Theory of Conduction in Metals

As mentioned earlier, the movement of electrons within the crystalline lattice in the absence of an external electric field is considered random, as illustrated in Figure 12.5.

Figure 12.5: Random motion of an electron in a metallic crystal without an external electric field, moving rectilinearly between collisions. The particle appears to move around an average position.

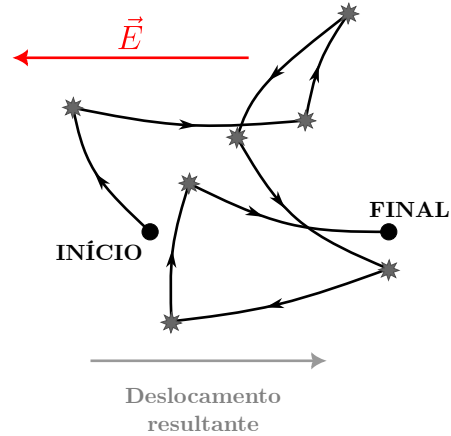


Adapted from Young e Freedman [1].

When an electric field \vec{E} is applied within a metal, the conduction electrons are dragged by the electric force $\vec{F} = -e\vec{E}$, resulting in a drift velocity \vec{v}_d opposite to the field, as shown in Figure 12.7. In a given time dt , the electrons will traverse an additional distance $\vec{v}_d dt$ compared to what they would cover in the absence of an electric field, as illustrated in Figure 12.5.

The flow of electrons traveling from one region to another generates an electric current (I) within

Figure 12.6: Random motion of an electron in a metallic crystal with an external electric field \vec{E} . The trajectory of electrons is slightly curved, resulting in a net displacement due to the electric force exerted on the particles.



Adapted from Young e Freedman [1].

the conductor². The intensity of an electric current is the amount of electric charge (Q) that crosses a cross-sectional area (A) of a conductor in a certain time (t):

$$I = \frac{dQ}{dt} \quad (12.2)$$

For a more general case, the current can be written as the scalar product between current density (J) and the cross-sectional area (A), where θ is the angle formed between them:

$$I = \vec{J} \cdot \vec{A} = J \cdot A \cdot \cos \theta \quad (12.3)$$

12.4.1 Conductivity and Electrical Resistivity

In this section, we will introduce the concepts of electrical conductivity and resistivity, which are the focus in modeling electrical conduction as proposed in the Drude model.

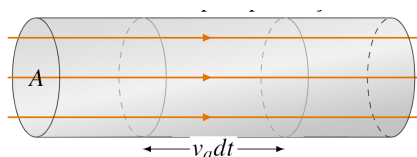
Considering the example of a cylindrical conductor, within a time interval dt , electrons cover a distance $v_d dt$. All electrons within this distance from an area A will traverse it, and these electrons are involved in a cylinder of volume $Av_d dt$. Taking into

²In common metals such as copper and aluminum, electrons naturally move within the material. However, this movement does not imply an effective flow of charges since free electrons move randomly within the material, with no fixed direction of displacement; hence, there is no electric current [1].

account that it contains n electrons per unit volume, and each of them has a charge of $-e$, the charge dQ flowing in this conductor will be $nev_dA dt$. Therefore, the current intensity can also be described as:

$$I = -neAv_a. \quad (12.4)$$

Figure 12.7: Random motion of an electron in a metallic crystal with an external electric field \vec{E} . The trajectory of electrons is slightly curved, resulting in a net displacement due to the electric force exerted on the particles.



Adapted from Young e Freedman [1].

From this, it is possible to write the current density (J), defined as the current flow per unit area of the cross-sectional area:

$$\vec{J} = \frac{I}{A} \hat{v}_a = -nev_a \vec{v}_a. \quad (12.5)$$

The electric current density \vec{J} is influenced by the applied field \vec{E} and the characteristics of the material itself. For certain materials, such as metals, at certain temperatures, the ratio $|\vec{E}|/|\vec{J}|$ is nearly constant. The relationship between these two properties is described by Ohm's Law. The proportionality constant is the resistivity (ρ), which expresses the difficulty with which a current is induced by an electric field in a conductor.

$$\vec{E} = \rho \vec{J}. \quad (12.6)$$

It is important to emphasize that resistivity does not depend on the geometric structure of the conductor but is intrinsically linked to the material from which it is made. The inverse of resistivity is electrical conductivity ($\sigma = |\vec{J}|/|\vec{E}|$), a property that expresses the ease with which a material conducts electricity. The higher the current density induced by a fixed electric field, the higher the conductivity of that material. Metals and metal alloys are the best conductors due to their low resistivities, which can be up to 10^{22} times smaller than those of insulating materials like amber and glass.

12.5 Application

12.6 Hall Effect

In this section, we will explore the phenomenon known as the Hall Effect. The Hall Effect was a fundamental discovery in physics that reveals the relationship between electric currents, magnetic fields, and the generation of a potential difference perpendicular to both. This phenomenon can be used to develop various practical applications, from magnetic sensors to advanced electronic devices.

In this chapter, it will be used to validate the assumptions adopted by Drude in his model of electrical conduction in metals.

12.6.1 Electric charges in motion under the action of an external magnetic force

When analyzing electric charges in motion, it is important to consider the existence of external magnetic fields (generated by a permanent magnet) or even the magnetic field generated by the charges themselves. In any of these situations, a magnetic field \vec{B} exerts a force on a charge q perpendicular to its velocity \vec{v} , causing a deviation in its trajectory [6]. The Lorentz force (Equation 12.7) determines the superposition of an electric force and a magnetic force exerted on a moving charge:

$$\vec{F} = q (\vec{E} + \vec{v} \times \vec{B}). \quad (12.7)$$

The Lorentz force was the basis for understanding J. J. Thomson's cathode ray experiment, which led to the discovery of the electron in 1897. In this experiment, Thomson adjusted the parameters of his apparatus so that the electric field was perpendicular to the magnetic field, making $F_E = F_B$ and causing the electron beam to follow a straight trajectory. Thus, the velocity of the electrons could be calculated using the relationship:

$$eE = evB \Rightarrow v = \frac{E}{B}. \quad (12.8)$$

12.6.2 Effect of an external magnetic field on an electric current

When these charges are trapped in a metal conductor, the Hall Effect, discovered in 1879 by the American physicist Edwin Hall, is an excellent way to analyze the effects of a magnetic field on an electric current. Hall wondered if this force would be applied throughout the length of the wire or only

on the moving charges; today we know that in metals, these charges are electrons. If the second option were true, Hall argued that the electrons would be attracted to one side of the wire, and consequently, an additional resistance to the current flow would be noticed.

Although he did not notice this resistance in his experiments, Hall believed that even if a permanent magnet could not divert the electrons significantly enough to alter the resistance of a conductor, it would cause a potential difference within it. This voltage effect, now called Hall voltage, was observed by Hall in his experiments and confirmed his thesis about the magnetic effect on free electrons.

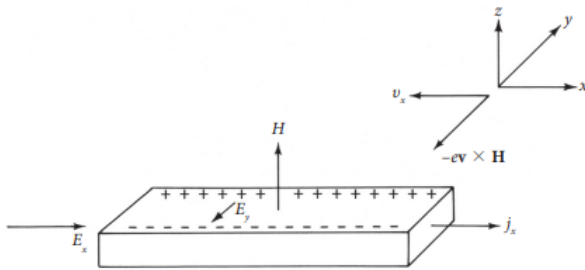
The Hall experiment (Figure 12.8) involves applying an electric field E_x to a wire extending in the x direction, inducing the passage of a current density J_x . A magnetic field \vec{H} in the $+z$ direction exerts a magnetic force F_H in the $+y$ direction. Thus, the force experienced by an electron can be determined by the Lorentz force:

$$F_H = -ev_a \times H. \quad (12.9)$$

Due to the force F_H , the electrons will undergo a deviation in the trajectory in the $-y$ direction (the drift velocity of the electrons is opposite to the direction of the electric current). Consequently, the electrons will collide with the sides of the wire at some point, accumulating in such a way as to generate an electric field in the $+y$ direction.

This accumulation will occur until the electric field \vec{E}_y increases to the point of producing a force of magnitude eE_y equal and opposite to the force of magnitude $ev_a H$. Thus, the Hall field will be in equilibrium. After this point, the moving charges no longer undergo deviations caused by transverse forces that can deflect their trajectory [7].

Figure 12.8: Schematic view of the Hall effect experiment.



Ashcroft, N.W. and Mermin, N.D. (1976).

From this, the ratio between the field E_x and the

current density J_x is defined as a quantity called magnetoresistance:

$$\rho(H) = \frac{E_x}{J_x}. \quad (12.10)$$

Another important quantity when it comes to the Hall effect is the Hall coefficient (R_H), which measures the intensity of E_y , as it balances the Lorentz force:

$$R_H = \frac{E_y}{J_x H}. \quad (12.11)$$

When the Hall field is oriented in the $-y$ direction as in Figure 12.8, the Hall coefficient must be negative; thus, the charge carriers have a negative sign. If the charges are positive, the direction of movement would be opposite, in the $-x$ direction, and therefore, the Hall field would be oriented in the $+y$ direction. Thus, the Hall experiment makes it possible to discover the sign of the charge carrier of electricity in a given material just by observing the lateral polarity of the conductor. An unusual fact is that some metals have a positive Hall coefficient, indicating that the charge carriers have a positive charge. The Drude model cannot explain this phenomenon, as the explanation for it only emerged with the quantum theory of solids.

To find the magnetoresistance and the Hall coefficient, it is necessary to calculate the components E_x and E_y of the electric field and the components of the density J_x and J_y . The force acting on each electron will be

$$f = -e \left(\vec{E} + \vec{v}_a \times \vec{H} \right). \quad (12.12)$$

This is the average force felt by the electrons since the velocity of each of them is variable. Therefore, in this case, the average velocity p/m must be used.

$$\frac{d\vec{p}}{dt} = -e \left(\vec{E} + \frac{\vec{p}}{m} \times \vec{H} \right) - \frac{\vec{p}}{\tau}. \quad (12.13)$$

In the steady state, the electric current does not vary with time, which implies that the components p_x and p_y of the electron momentum also do not vary with time. This means that the momentum of the electrons in the x and y directions is constant over time ($\dot{p}_x = \dot{p}_y = 0$), even in the presence of electric and magnetic fields. Therefore:

$$0 = -e\vec{E} - \frac{e\vec{p} \times \vec{H}}{m} - \frac{\vec{p}}{\tau}. \quad (12.14)$$

The trajectory of an electric charge in a medium with a constant magnetic field is curvilinear, with a radius $r = mv/eH$. In this case, we usually define

the angular frequency $\omega_c = v/r$. Using this definition in the situation we are dealing with leads to:

$$\omega_c = \frac{eH}{m}. \quad (12.15)$$

Analyzing Equation 12.14, the x component provides:

$$0 = -eE_x - \omega_c P_y - \frac{p_x}{\tau} \Rightarrow eE_x = -\omega_c p_y - \frac{p_x}{\tau}. \quad (12.16)$$

Similarly, the y component gives us:

$$0 = -eE_y + \omega_c P_x - \frac{p_y}{\tau} \Rightarrow eE_y = \omega_c p_x - \frac{p_y}{\tau}. \quad (12.17)$$

By multiplying Equation 12.16 by $-ne\tau/m$, it is possible to introduce the terms of conductivity ρ and current density J (Equation 12.5):

$$\sigma_0 E_x = \omega_c \tau J_y + J_x. \quad (12.18)$$

Analogously, we have that:

$$\sigma_0 E_y = -\omega_c \tau J_x + J_y. \quad (12.19)$$

Note that these equations can be written in the form:

$$\begin{pmatrix} E_x \\ E_y \end{pmatrix} = \frac{1}{\sigma_0} \begin{pmatrix} 1 & \omega_c \tau \\ -\omega_c \tau & 1 \end{pmatrix} \begin{pmatrix} J_x \\ J_y \end{pmatrix}. \quad (12.20)$$

And now, the resistivity ρ of the material becomes dependent on the direction, with the electric current flowing in one direction influencing the electric current flowing in an orthogonal direction.

To find the E_y component of the Hall field, the condition that there is no transverse current, i.e., a current in the y direction, is determined. By defining J_y as zero in the second equation, we find:

$$E_y = - \left(\frac{\omega_c \tau}{\sigma_0} \right) J_x. \quad (12.21)$$

By Equation 12.15, we have:

$$E_y = - \left(\frac{H}{ne} \right) J_x. \quad (12.22)$$

Thus, the Hall coefficient can be described as:

$$R_H = \frac{d}{dH} \left(\frac{E}{J} \right) = -\frac{1}{ne}. \quad (12.23)$$

This result shows that the Hall coefficient does not depend on material properties but only on the density of conduction electrons, which can indicate

whether the assumption of the Drude Model that metallic conduction occurs through valence electrons is valid. However, there is a difficulty in obtaining the density n when measuring the Hall coefficient in experiments. Contrary to expectations, these coefficients generally depend on the applied magnetic field, temperature, and sample preparation conditions.

Under ideal conditions, the observed Hall coefficients stabilize and show consistent behavior as they approach a specific limit value that is independent of variations in the applied magnetic field. This limit value represents a reference point or an intrinsic property of the material, which can be used to obtain more precise information about the electron density of a material.

12.7 Conclusion

In summary, while the Drude model served as a crucial milestone in the initial understanding of electron behavior in metals, it has significant limitations. The model is effective in providing a simplified description of some electrical phenomena, such as electrical conductivity, but falls short by not considering crucial aspects such as crystal structure, interactions between electrons and ions, and more complex electronic properties. Experimental discrepancies, particularly regarding interionic distance at low temperatures, highlight the model's shortcomings. Additionally, the Drude model fails to explain the positive Hall coefficient observed in some metals, underscoring its inadequacy in more complex scenarios.

The evolution towards the quantum theory of solids, which incorporates the wave nature of electrons and energy bands in materials, overcomes these limitations. The quantum theory of solids offers a more comprehensive explanation for electrical phenomena, especially in metals with specific characteristics, where Hall coefficients exhibit notable dependencies on magnetic fields. This anomalous deviation necessitates a deeper understanding of quantum effects and the electronic structure of solids, providing a more robust foundation for the study and comprehension of electrical phenomena in materials.

Bibliografia

- [1] YOUNG, Hugh D.; FREEDMAN, Roger A. Física III: eletromagnetismo. São Paulo: Pearson Education do Brasil, 2009.

- [2] WIKIPEDIA. Paul Drude. 2023. https://pt.wikipedia.org/wiki/Paul_Drude, Acessado em: 20/11/2023.
- [3] ASHCROFT, N. W.; MERMIN, N. D. Solid state physics. [S.l.]: World Book Publishing Company, 1976.
- [4] PÉREZ, C. A. S. O modelo do elétron livre de drude completa 100 anos. Caderno Brasileiro de Ensino de Física, v. 17, n. 3, p. 348–359, 2000.
- [5] BAGNATO, V. S.; RODRIGUES, V. Análogo mecânico para condutividade elétrica dos metais: Efeito da temperatura. Revista Brasileira de Ensino de Física, SciELO Brasil, v. 28, p. 35–39, 2006.
- [6] OLIVEIRA, N. A. d. Eletromagnetismo: teoria e aplicações. [S.l.]: LTC - Livros Técnicos e Científicos, 2019.
- [7] WALKER, J.; RESNICK, R.; HALLIDAY, D. Fundamentos de Física 3–Eletromagnetismo. [S.l.: s.n.], 2009.